Published in final edited form as:
Chem Rev. 2010 May 12; 110(5): 3212–3236. doi:10.1021/cr900396q.

Theory, Instrumentation, and Applications of EPR Oximetry

Rizwan Ahmad† and **Periannan Kuppusamy**†

† Center for Biomedical EPR Spectroscopy and Imaging, Davis Heart and Lung Research Institute, Department of Internal Medicine, The Ohio State University, Columbus, Ohio 43210, USA

1 Introduction

Oxygen is the third most abundant element in the universe by mass after hydrogen and helium. It has an atomic number 8 and is represented by the symbol O. At standard temperature and pressure, two atoms of the element bind to form molecular oxygen (O_2) which is a colorless, odorless, and tasteless diatomic gas, occupying 20.9% of air volume. Since its discovery[1] in the 1770s, its properties, chemistry, and relevance to life have intrigued generations of scholars and scientists. A multitude of scientific evidence[2–4] builds a compelling case for the vital role of oxygen in the evolution of life on earth. Aerobic organisms consume molecular oxygen to generate chemical energy, required for biologic processes, in the form of adenine triphosphate. Also, O_2 serves as a regulatory molecule for important physiologic processes.

In mammals, including humans, inhaled oxygen from the lungs is carried to the target tissue by the oxygen-carrying protein, hemoglobin. At the target tissue, where the cells actively engage themselves in respiration (oxidative phosphorylation), oxygen is released from the oxygen-bound hemoglobin (oxyhemoglobin), and the released oxygen is available to the metabolically active tissues. Any imbalance in tissue oxygen levels, which may occur due to altered supply or utilization of oxygen, may affect metabolic homeostasis and lead to pathophysiological conditions[5]. In addition, the level of oxygen at specific sites may affect cell signaling[6,7]. Hence, a precise knowledge of the levels of oxygen in the tissue of interest will be of paramount importance in our ability to understand the mechanism of pathogenesis and to develop strategies to correct the imbalance. This would require methods capable of quantifying the levels of tissue oxygenation with good spatial and temporal resolution. The information gained will enable better understanding of various metabolic and disease states and will assist in making effective clinical decisions regarding treatment and therapy options. The chemical and physical properties of oxygen enable a wide variety of methods for measuring and mapping oxygen content *in vivo*.

There are numerous reviews on various oxygen measurement techniques and their applications to specific organs and diseases[8–10]. For any particular application, the choice of an oximetry method is determined by its accuracy, measurement procedure, acquisition time, invasiveness, and relevance of the measured form of oxygen, which includes oxygen concentration, partial pressure of oxygen (pO_2), or oxygen saturation.

Electron paramagnetic resonance (EPR), also called electron spin resonance, is a magnetic resonance based technique capable of measuring oxygen levels in biological sampling, both *in vitro* and *in vivo*[11]. Over the past couple of decades, EPR oximetry technique has been continually refined to collect repetitive, minimally invasive, and accurate measurements of pO_2 over an extended duration[12,13]. At the same time, the biological applications for EPR oximetry have been rapidly growing and now include monitoring tumor oxygenation for determining cancer-treatment efficacy[14,15] and measuring tissue oxygen for estimating the extent of myocardial injury during both ischemia and subsequent reperfusion[16].

This article provides a brief survey of basic principle and novelty, instrumentation, measurement procedures, and a few promising applications of EPR oximetry for biological systems. Section 2 describes some commonly used experimental and clinical methods for tissue oxygen measurements. Section 3 discusses the basic principle of EPR oximetry and provides motivation by outlining its unique advantages. Section 4 provides the basic layout of a typical EPR spectrometer. Section 5 covers basics of data collection and processing procedures for EPR oximetry, and highlights some of the developments proposed to speed up the acquisition process. Section 6 describes spin probe development for EPR oximetry and encapsulation methods for particulate spin probes. Section 7 lists a few important, mainly *in vivo*, applications of EPR oximetry.

2 History of Tissue Oxygen Measurement

Even though the discovery of oxygen was made in the late 18th century, measurements of oxygen levels in biological samples have been studied only in the 20th century. In the 1930s, the German scientist Karl Matthes first used variable transmission of red and infrared light through the human ear to assess oxygenation[17]. An ear oximeter, developed in 1942 by the American scientist Glen Milliken, was used for many years in pulmonary and physiology laboratories. Several other attempts were made in the 1960s[18,19] but it was in the late 1980s that the computerized polarographic needle electrode system was used to assess tumor oxygenation in the clinic[20]. The use of this electrode technique helped establish the role of hypoxia in determining the effectiveness of radio- or chemotherapy[21,22]. Now there exist several oximetry methods that are based on other principles, including fluorescence and phosphorescence quenching, optical detection, immunohistochemical detection, and magnetic resonance techniques.

2.1 Chemical Methods

2.1.1 Polarographic Electrode—Blood and tissue oximetry using a polarographic electrode was proposed by Leland Clark[23]. The method is based on measuring the electric current resulting from the electrochemical reduction of oxygen at the cathode. In addition to the consumption of oxygen, the relatively large size of earlier designs lead to serious practical issues, such as artifacts due to blood flow, acute tissue injury, and signal averaging over a large volume. To avoid such issues, efforts have been made to design miniaturized polarographic electrodes[24], also called 'microelectrodes'. Modern recessed tip microelectrodes are available in the range of 5–10 μm[25] in diameter.

The commercially available recessed tip microelectrode by Eppendorf has been widely used to measure *in vivo* oxygenation of tissues. Owing the widespread use of this technique, it has been considered the 'gold standard' for measuring tissue oxygenation[26]. The method has been extensively used for measuring oxygen in tumor[27–29] and brain[30]. However, there are several disadvantages associated with polarographic electrodes including, consumption of oxygen by the electrode, poor signal-to-noise ratio (SNR) at low oxygen concentration, inability to make repeated measurements, and the highly invasive nature of the measurement procedure.

2.1.2 Transcutaneous Oxygen Sensor—A different setup using polarographic oxygen electrodes has been used for transcutaneous oxygen monitoring[31] (TCOM). In a typical setup, the electrode is pressed against skin to effectively measure the diffusion of oxygen through skin noninvasively. The method is quantitative, and it is thus far the only device that measures oxygen delivery to an end organ (the skin). It has been used to monitor oxygenation levels (in mmHg) in the skin, especially for premature infants[32], but also for adults in the intensive care setting[33]. Physicians also use TCOM to determine whether or not there is adequate blood flow to support healing of a lower extremity wound[34], such as a venous stasis ulcer or diabetic foot

ulcer. The necessity for exogenous skin heating along with the sensitivity of this method to skin properties, temperature fluctuations, and mechanical pressure pose a serious limit to it accuracy.

2.1.3 Immunochemical Methods—This technique requires the administration of a hypoxia marker such as 2-nitroimidazoles[35]. These bioreductive markers belong to the class of compounds that have maximum binding to severely hypoxic cells (with less than 0.38 mmHg of oxygen, for example) and increased inhibition to increasing oxygenation as dictated by Michaelis-Menton kinetics[36]. This approach is also used in combination with immunohistochemical techniques where hypoxia can be visualized and compared with necrosis, proliferation or oxygen-regulated protein expression[37]. However, the dependence of hypoxia marker binding on factors other than pO_2, such as level of tissue perfusion or the amount of reductases in the tissue, may make quantification of the result more complex. Also, binding of the hypoxia marker may not differentiate between long-term steady-state hypoxia and short-term transient hypoxia.

2.2 Optical Methods

2.2.1 Fluorescence Oximetry—Fluorescence oximetry is based on oxygen dependant changes in the lifetime of fluorescence. This principle has been used in the construction of OxyLite[38], a widely used commercially available oxygen-measuring sensor. It uses ruthenium chloride, a fluorescent dye, connected to the tip of a fiber-optic cable. Photodiodes excite the fluorophores of the dye, and the resulting fluorescence lifetime relates inversely to the oxygen tension at the tip. Typical probe diameter is ~ 220 μm.

This method does not consume oxygen and is capable of monitoring rapid temporal oxygen changes at a given tissue location. This technique has been widely used for measurement of oxygen in tumor[39], liver and brain[40], and has been compared to other oximetry techniques[41, 42]. Some drawbacks of the technique include: sensitivity to movement and temperature, pressure induced artifacts due to insertion of the probe, invasiveness, and the inability to perform repeated measurements at the same location overtime.

2.2.2 Phosphorescence Oximetry—Measurement of oxygen using phosphorescence oximetry involves injection of a phosphor material into the vasculature and measuring the oxygen-induced changes in the lifetime of the induced phosphorescence[43]. A bifurcated light guide is used to focus the excitation light from the source to the surface of the tissue where it is detected by a phosphorometer. Oximetry by phosphorescence-quenching has now been in use for over two decades[44]. This technique is gaining importance for *in vivo* applications[45, 46] as further technical improvements, including probe development[47], are continuously being made. In a typical setup, the phosphorometer (detector) utilizes photomultipliers or avalanche photodiodes to measure the phosphorescence signal to get information about the distribution of the lifetimes and amplitudes of the phosphor probe. Data analysis involving calibration and deconvolution subsequently gives histogram representations of pO_2 over the sampled region. When the measurements are done in a grid pattern, it is possible to construct contour maps which then can be used to compute the volume fraction of tissue sampled for any selected range of pO_2 values. Besides the minimally invasive nature, a significant advantage of this method is its ability to provide real-time, repeated measurements. Phosphorescence oximetry has been widely used for mapping the oxygen distribution in the retina[48] and other organs such as the heart and brain[49]. It has also been used to study oxygen distribution in murine vasculature[50] and oxygenation of tumors[51]. A major disadvantage of this technique is the need to inject the phosphor material into the vasculature. Also, the technique provides only the vascular oxygen concentration.

2.2.3 Pulse Oximetry—Pulse oximetry enables indirect measurement of oxygen saturation of blood which indicates the balance between oxygen delivery and consumption. It is a noninvasive method based on the differential absorption of red and infrared light by oxyhemoglobin and deoxyhemoglobin[52]. The ratio of the absorption of the red and infrared light is converted to the ratio of oxyhemoglobin and deoxyhemoglobin. The pulse oximeter consists of a pair of small light emitting diodes, one red and one infrared, facing a photodetector. Sites of measurement include fingers, toes, and earlobes, which have adequate blood flow. Due to the noninvasive nature and ease of use, this technique is more commonly used for clinical applications[53]. The major shortcomings of this method include: requirement of adequate arterial perfusion, motion artifacts, inability to measure tissue oxygenation, measurement of oxygen saturation rather than the actual oxygen content, inability to distinguish between carboxyhemoglobin and oxyhemoglobin, and stray light interference.

2.2.4 Near-Infrared Spectroscopy (NIRS)—The NIRS technique works on a physical principle similar to that of pulse oximetry, i.e., the light transmitted through a tissue is absorbed differently by oxygenated and deoxygenated hemoglobin in the circulation. The NIRS technique is noninvasive, with excellent temporal resolution, low-cost, and portability[54]. Due to the longer penetration depth of NIRS, real-time repeated measurements from relatively deep locations are possible. NIRS has been used for clinical studies of oxygen utilization in tissues and muscle oxygenation[55], especially in the area of exercise physiology. In other clinical studies, NIRS has been used for monitoring peripheral vascular disease[56], ischemic and hemorrhagic stroke[57], cerebral oxygenation[58], and blood flow measurements[59]. One drawback of the NIRS method is that it does not measure tissue pO_2 directly but rather provides the information about vascular oxygen saturation. Also, the absorption spectra of most common chromophores, such as oxyhemoglobin, deoxyhemoglobin, and cytochrome *c* oxidase, overlap which may result in ambiguous quantification[60].

2.2.5 Hyperspectral Imaging (HSI)—Oximetry using hyperspectral imaging relies on analyzing reflectance measurements that are backscattered and spectrally altered by the tissue to assess blood oxygen saturation[61]. The working principle of HSI is similar to NIRS, but unlike NIRS, it collects and processes information from many different visible wavelengths. The main advantage of using this technique is that it is noninvasive and allows a direct observation of blood-oxygen supply. This method has been applied to measure oxygen saturation in the optical nerve head and retina[62]. It has also been used to evaluate hemoglobin saturation in murine tumors[63] and tissue perfusion in humans[64]. In addition, HSI based methods have been used to investigate wound healing[65] and to diagnose hemorrhagic shock[66]. Major drawbacks associated with HSI include: lack of accuracy, complexity of data analysis, and inability to directly measure tissue oxygenation.

2.3 Nuclear and Magnetic Methods

2.3.1 PET Imaging—PET-based oximetry uses short-lived positron-emitting radionuclides for *in vivo* imaging of a variety of hypoxia biomarkers[67]. Besides radio-labeling of the biomarkers, the basic principle of this modality is similar to that of immunochemical methods. The common hypoxia markers used in PET are ^{18}F-containing imidazoles[68] (e.g., ^{18}F fluoromisonidazole, FMISO) and ^{18}F-containing pentafluorinated derivative of etanidazole[69] (EF5). Researchers at Washington University and Searle Radiographers developed instrumentation that could be used for *in vivo* imaging of the positron-emitting radionuclides[70]. PET oximetry is a noninvasive method that has been extensively used in tumor models for hypoxia mapping in mice and rat. Clinical studies include head and neck cancer[71] and lung cancer[72]. The PET/MRI and PET/CT combined modalities are also gaining importance as they have the added advantage of obtaining anatomical information along with

PET data. The use of PET oximetry is limited by the availability and cost of cyclotrons needed to produce short-lived radionuclides.

2.3.2 ^{19}F MRI—In 1988, Busse *et al.*[73] showed that ^{19}F nuclear magnetic resonance (NMR) spin-lattice relaxation rate (R_1) of perfluorocarbon probes could be used for imaging tumor pO_2 *in vivo*. The technique is based on NMR, but unlike conventional MRI (proton imaging), a probe based on perfluorocarbons (PFCs) is used. The PFCs are infused intravenously in the form of emulsions[74]. The ^{19}F spin lattice relaxation rate (R_1) of PFCs varies linearly with dissolved oxygen concentration. Thus, the ^{19}F-based oximetry reports absolute values of oxygen concentration. Hexafluorobenzene[75] (HFB) and perfluoro-15-crown-5-ether[76] (15C5) have been the most widely used PFCs for this application. Using this technique, it is possible to image pO_2 as well as follow dynamic changes in tumor oxygenation. It is also possible to combine the ^{19}F images and ^{1}H anatomical images to provide spatial registration. This method has been used in rodent models for different types of tumors including breast[77] and prostate[78]. Studies have also been conducted in rat brain[79], lung[80], and human eye[81]. Yu *et al.*[82] have reviewed ^{19}F MRI for physiological and pharmacological applications. The main concern with ^{19}F MRI is the toxicity of PFCs which needs to be fully characterized before this method can be used for clinical applications.

2.3.3 BOLD Imaging—In 1982, Thulborn *et al.*[83] described the oxygenation dependence of the transverse relaxation time of water protons. Later, Ogawa *et al.* described blood oxygen level-dependent (BOLD) MRI of tissues for imaging the blood oxygen level in rat brain[84]. BOLD images reflect the changes in the amount of oxygen bound to hemoglobin in blood. The presence of deoxyhemoglobin, which is paramagnetic in nature, can cause differences in susceptibility (i.e. changes in the local magnetic field) around the blood vessels, which affects the relaxation properties of the surrounding protons. Thus, a change in T_2-weighted image can be used to quantify changes in blood oxygenation. BOLD MRI oximetry is noninvasive and can be performed using available clinical scanners and has the advantage of the availability of fast imaging sequences. It can also provide information regarding temporal changes[85] in oxygenation. The repeatability and voxel-by-voxel information about changes in blood oxygenation co-registered with anatomical information are also advantages over other imaging techniques. A major disadvantage of the BOLD oximetry is that it does not provide quantitative information[86] of blood oxygenation. It measures the changes in blood oxygenation, but not absolute oxygen concentration in tissue.

3 EPR Oximetry

EPR oximetry is a minimally invasive magnetic resonance method capable of measuring direct and absolute values of pO_2 or O_2 concentration. In 1977, Backer *et al.*[87] reported the reversible and repeatable effect of oxygen concentration on the superhyperfine structure of EPR spectra of a soluble spin probe, also called spin label. Soon after, more oxygen-sensitive spin probes were developed and used for biological applications[88,89]. In the 1980s, James Hyde explored the quantifiable affect of oxygen concentration on the relaxation rates[90,91] of various spin probes, which remains the basis of present day EPR oximetry. He also greatly contributed to the development of instrumentation[92] and methodology for making EPR measurements. In 1986, Subczynski *et al.* reported the first *in vivo* EPR oximetry measurement[93] which was conducted on mice using an L-band EPR spectrometer. Over the last two decades, EPR oximetry has emerged as a promising technique for biological applications with unique advantages over other existing oximetry methods[11,94]. It possesses a high sensitivity to pO_2, and can provide three dimensional (3D) mapping of oxygen distribution, if required. This method shows a high specificity because of minimal interference from other sources. In addition, the spin probes are nontoxic, and are generally stable in a tissue environment. In fact, particulate (solid-state, crystalline, and water-insoluble) spin probes can stay in a biological

sample for months without losing their oxygen sensitivity[95,96]. Therefore, the particulate-based EPR oximetry is usually described as 'minimally invasive' as only one-time implantation of the particulate spin probe is needed, and the subsequent measurements are carried out without any invasive procedure.

Despite all these advantages, there exist numerous technical challenges that have limited the widespread use of *in vivo* EPR oximetry. Some of the technical problems encountered in EPR oximetry include: nonresonant absorption at higher frequencies resulting in unwanted heating of aqueous samples, poor SNR, small penetration depth especially at higher frequencies, requirement of an exogenous probe, rapid bioreduction or excretion of soluble spin probes, long acquisition times, and motion artifacts.

3.1 Principle of EPR Spectroscopy

EPR was first discovered by Zavoisky in 1944. It is a branch of spectroscopy in which electrons with unpaired spins, when placed under a magnetic field, absorb electromagnetic radiation to transition from low energy level to high energy level. In principle, EPR is similar to nuclear magnetic resonance (NMR) spectroscopy where the transition of protons between two energy levels is observed.

In EPR, the energy differences studied are primarily due to the interaction between electronic magnetic moments and the external magnetic field, B_{ext}, also called main magnetic field. Due to its magnetic moment, an unpaired election acts like a tiny bar magnet in the presence of an external magnetic field. It possesses the lowest energy if the magnetic moment is aligned with B_{ext} and the highest energy if it is aligned opposite to B_{ext} as shown in Figure 1. This is generally called the Zeeman Effect.

Since an electron is a spin 1/2 particle, the low energy and high energy states can be designated as $M_s = -1/2$ and $M_s = +1/2$, respectively. The energy E of an unpaired electron in an external magnetic field B_{ext} can be defined as

$$E = g\beta M_s B_{ext} = \pm \tfrac{1}{2} g\beta B_{ext}$$
$$\Delta E = g\beta B_{ext} = \hbar\gamma B_{ext} \quad (1)$$

where ΔE is the energy difference between the two states, dimensionless g is the g-factor or g-value, β is the Bohr magneton which is the unit of magnetic moment, $\gamma = g\beta/\hbar$ is the gyromagnetic ratio, and $\hbar$ is the reduced Plank's constant. If B_0 is the external magnetic field where ΔE in Eq. (1) matches the radiated energy $h\upsilon_0$, we can write

$$B_0 = \frac{2\pi\upsilon_0}{\gamma} = \frac{\omega_0}{\gamma} \quad (2)$$

where υ_0 is the frequency, in Hertz, of electromagnetic excitation usually in the radiofrequency (RF) range.

The splitting between energy states, depicted in Figure 2, varies linearly with B_{ext} and is degenerate when $B_{ext} = 0$, which means that the two states have the same energy in the absence of external magnetic field. In the presence of the external magnetic field, absorption of the electromagnetic radiation happens whenever Eq. 2 is satisfied. The condition can be satisfied either by fixing the radiation frequency and adjusting B_{ext}, or by fixing B_{ext} and adjusting the radiation frequency. The limitation of RF hardware, however, makes the latter choice

unattractive. At resonance, the unpaired electrons at the lower energy level absorb the RF radiation and jump to the higher energy state. These excited electrons move back to the lower energy state by releasing the excess energy. It is this transition between low and high energy states that is recorded in EPR.

Since the unpaired electron is exposed to its surrounding, nuclei with magnetic moment in the vicinity of an unpaired electron may affect the local magnetic field experienced by the unpaired electron, which may result in further splitting of the spectrum, called hyperfine splitting[97]. The presence of hyperfine structures in an EPR spectrum can provide a wealth of information regarding the free radical species and their environments.

3.2 Principle of EPR Oximetry

Molecular oxygen is a naturally occurring triplet radical and cannot be directly detected by EPR when in dissolved state due to extremely short relaxation time[98]. Hence, measurement of oxygen concentration by EPR (EPR oximetry) involves the use of an external spin probe consisting of paramagnetic material in either particulate (solid) or soluble form. The changes in the EPR linewidth of the exogenous spin probe are caused by the interaction of two paramagnetic species, molecular oxygen and the spin probe. The interaction includes dipole-dipole interaction and Heisenberg spin exchange[99], with the latter being the dominant interaction for the majority of commonly used soluble spin probes with low viscosities. The broadening of EPR spectrum, depicted in Figure 3, permits quantification of pO_2 or O_2 concentration.

The spin-spin relaxation rate, R_2, which is directly related to linewidth (W) and inversely related to relaxation time (T_2), increases with oxygen concentration. For soluble spin probes, the line-broadening is caused by direct bimolecular collisions between two paramagnetic species, with the rate of collision, ω, given by the Smoluchowski equation,

$$\omega=4\pi r(D_p+D_o)C_o \tag{3}$$

where r is the interaction distance between oxygen and the spin probe, D_P and D_O are the diffusion coefficients of the soluble spin probe and oxygen respectively, and C_O is the oxygen concentration. Usually D_O is much greater than D_P. Therefore, Eq. (3) can be approximated as,

$$\omega=4\pi r D_o C_o \tag{4}$$

Since the linewidth of the EPR absorption spectrum varies linearly with the collision frequency ω, the relationship between linewidth and oxygen concentration is expected to be linear. Therefore, the measured linewidth can be used to quantify oxygen concentration.

For particulate spin probes, line-broadening is based predominantly on Heisenberg spin exchange[90]. In the absence of oxygen, the radicals of the particulate spin probe undergo intense Heisenberg electron-electron exchange, also called exchange narrowing, which results in a very narrow lineshape. This phenomenon of exchange narrowing for paramagnetic resonance was first suggested by Gorter *et al.*[100] in 1947 and was later mathematically modeled by Anderson *et al.*[101] in 1953. In the presence of exchange narrowing, any line broadening, for instance, due to magnetic dipole interaction, is narrowed by a fast dynamics resulting from the exchange coupling. With the introduction of oxygen, the spin exchange between two

paramagnetic species – oxygen and the spin probe – results in reversible line-broadening of the EPR spectrum.

The line broadening (ΔW) due to spin exchange between the spin probe and O_2 can be written as[102],

$$\Delta W = AKC_o \tag{5}$$

where

$$K = p_A(4\pi d D_o) \tag{6}$$

and

$$A = \frac{2}{\sqrt{3}}\gamma_I \tag{7}$$

where d is the distance of closest approach of O_2 to a spin of the particulate probe, γ_I is the gyromagnetic ratio of the paramagnetic specie, C_O is the concentration of O_2 adsorbed into the probe, p_A is the probability of spin exchange per collision, given by

$$p_A = \frac{4J^2 T_1 \tau_c}{3 + 4J^2 T_1 \tau_c} \tag{8}$$

Here, J is the exchange interaction between the spins of a colliding O_2 and the spins of particulate probe, τ_c is the mean interaction time, and T_1 is the oxygen relaxation time. For strong spin exchange ($p_A \approx 1$), Eq. (5) becomes

$$\Delta W \propto kC_o \propto D_o C_o \tag{9}$$

For many carbon-based particular spin probes, however, the dipole-dipole interaction, depending on the pore size of the material and the temperature, may become the leading contributor to the line broadening[102].

On a pulsed EPR spectrometer[103], the decay of magnetization, called free induction decay (FID), is recorded after applying an excitation pulse in the presence of a fixed magnetic field. On a continuous wave (CW) EPR spectrometer, the absorption spectrum is instead collected by subjecting the sample to a fixed monochromatic electromagnetic excitation and sweeping B_{ext}. The EPR spectrum, also referred to as the EPR lineshape, is simply the Fourier transform of FID[104]. The most common lineshapes are Lorentzian and Gaussian but other nonparametric lineshapes are not uncommon.

3.3 Spectroscopy and Imaging

There are three modes of data collection in EPR – spectroscopy, spatial imaging, and spectral-spatial imaging. EPR oximetry can be performed either in the first (spectroscopy) or the third (spectral-spatial) mode. For spectroscopy mode, the EPR signal from the entire irradiated section of the sample is collected simultaneously. Since there are no magnetic gradients or other means of spatial encoding, no information is provided on the spatial distribution of spins. This method is quick and suitable for a small localized single implant. Spatial imaging does not provide any spectral information and is generally used to construct spin density maps. This mode is generally not used for oximetry which is based on variations in the lineshape. In spectral-spatial mode, both lineshape and spin density are mapped by applying linear magnetic-field gradients varying in both orientation and strength. Further details of data collection and processing for these three modes of EPR oximetry are discussed in section 5.

4 Instrumentation

Over the past few decades, many advances in EPR instrumentation have been made to improve SNR of the data and reduce the data collection time. In this section, we discuss a basic layout of a CW EPR spectrometer and imager. The layout of a pulsed EPR system, which in principle is very similar to an MRI system, is discussed elsewhere[105,106].

4.1 Basic Layout

A general layout of a CW EPR spectrometer and imager is shown in Figure 4. A static magnetic field is provided by a main magnet assembly. The gradient coils provide a linear magnetic-field gradient necessary for spatial encoding in EPR imaging. The sample to be studied is placed in the cavity, also called the resonator, which helps to amplify weak EPR signals. The detector and electromagnetic radiation sources are housed in a box called the RF bridge. The signal channel primarily consists of a phase sensitive detector.

4.1.1 Main Magnetic Field—The design of the magnetic field system for EPR spectroscopy and imaging defines the size and geometry of samples that can be studied. The requirements of field homogeneity are more stringent for larger samples and for narrower lineshapes. In general, the system must provide a magnetic field with across volume inhomogeneity smaller by an order of magnitude than the smallest linewidth being measured.

Generally three types of magnets are utilized in the existing EPR imaging designs, namely, nonferrous electromagnets[107], iron-core electromagnets[108], and permanent magnets[109]. For low-field systems with static fields up to 500 Gauss, nonferrous electromagnets can be used. These magnets may utilize Helmholtz coil design, solenoidal design, or some type of hybrid multicoil design for improved homogeneity of the field. These electromagnets provide the advantage of simple current control of the field due to the absence of hysteresis effects associated with the iron core. However, low energy efficiency of such magnets limits the achievable field strength to several hundred Gauss.

Historically the iron-core electromagnets used in EPR spectrometers found the most widespread use in higher-field EPR systems (RF to X-band). Typically such a system utilizes a large pole-face electromagnet (15″ and over) with custom-machined pole pieces to further increase the gap[110]. Permanent magnet-based systems have not gained a wide use due to poor thermal stability of the field and, thus, a need for elaborate systems of compensation coils and electronics. To ensure the stability of the magnetic field, for any magnet type, the Hall-effect sensor-based feedback is generally used. Figure 5 shows main magnet and magnetic field gradient assembly for an L-band EPR imager.

4.1.2 Gradient Coils—EPR imaging imposes extremely stringent requirements for magnetic field gradient design when compared to MRI. This is due to the fact that strong linear gradients (more than an order of magnitude stronger than for clinical MRI systems which are typically in the range of 1–4 G/cm) are required to obtain high spatial and spectral resolution due to the much broader lineshapes of EPR spectra. Also in CW-EPR imaging, the gradients must be able to dissipate peak power during long periods of time. Transient response, however, is less important than that for MRI so that active shielding is usually not necessary. As the sample size increases, problems imposed by the need for powerful field gradients escalate since the power required to generate a given gradient increases with the cube of the gap distance between the coils of the main magnet. Dissipation of the power in the coils also becomes more difficult as the surface/volume ratio of the coil decreases.

Two distinct gradient coil designs are selected for the two major geometries of main magnetic field coil designs, i.e., Helmholtz pair coils and a solenoidal coil[111]. The Z-gradient coils, for either of the main magnetic field coil designs, are Maxwell pair coil configuration. However, for X- and Y-gradient coils, the use of flat square pairs (four coils per axis as shown in Figure 6) is preferred for the Helmholtz main field geometry, while curved Golay gradient coil design[112] is required for the solenoid electromagnet to conform with the cylindrical geometry. A system of multiple computer-controlled power supplies must be utilized to drive the gradient coils as required by the projection acquisition sequence. Ideally these power supplies are a bank of switching mode operational power amplifiers capable of four-quadrant operation with an IEEE-488 or other computer interface.

4.1.3 RF Bridge—The RF bridge handles the generation of RF signal and the detection of the EPR signal coming out of the resonator. Key components of a typical RF EPR bridge, labeled in Figure 7, are briefly described below.

- i - Oscillator: It is used to generate RF energy. The frequency of RF energy is generally varied with mechanical and electrical means. While mechanical adjustments are used for coarse tuning, electronic adjustments are applied for fine tuning. The oscillator must have a stable output frequency and amplitude, as even slight changes can introduce distortion in the data.
- ii - Attenuator: It precisely controls the amount of RF energy delivered to the resonator. It must be very stable over time and a broad temperature range.
- iii - Circulator: Circulator allows reflected energy from the resonator at port 2 to reach the detector diode at port 3 while blocking high level excitation energy from port 1 to reach port 3.
- iv - Resonator: Resonator is used to amplify small changes induced in the RF radiation due to the magnetic resonance of the sample. The change in RF energy absorbed by the sample, upon magnetic resonance, changes the impedance of the resonator. This change in impedance changes the reflection coefficient of the resonator, resulting in reflected RF power fluctuation. In CW EPR, it is this fluctuation of the reflected RF power that is converted into an EPR signal.
- v - Detector: It converts RF energy reflected from the resonator into baseband signal. It is generally comprised of a diode detector and a passive low pass filter. The electrical output signal from a typical detector diode is 1500 mV output per mW of RF input. Since excessive RF power can permanently damage the diode, additional protection circuitry is included to monitor and limit the diode current
- vi - Reference Arm: It is used to apply small RF power to bias the detector diode into the more sensitive operating region. An RF phase (α) shifter synchronizes reference

arm power with the reflected power from the resonator. Many homebuilt units do not have a reference arm and require off resonance coupling of the resonator for the bias.

- vii - Preamplifier: It amplifies the small signal (typically less than 10 mV) from the detector for further filtering and amplification by lock-in amplifier (signal channel).
- viii - AFC: Automatic frequency controller modulates frequency of the RF source with 70 kHz signal. It further processes the 70 kHz component of the signal coming from the preamplifier to provide a feedback to electronically match RF oscillator frequency to that of the resonator.
- ix - SAW Oscillator: It generates saw tooth waveform (in the range of 400 Hz) to provide frequency sweep for tuning mode.
- x - Tuning Display: It displays oscillator frequency sweep (x-axis) verses reflected power from resonator (y-axis) during the tuning mode. It allows visual feedback for tuning the oscillator frequency to the resonator frequency.

4.1.4 Resonator—EPR resonator design is important to maximize sensitivity, and must be tailored to accommodate the sample with the highest possible *filling factor* × *quality factor* product. The quality factor, Q, is the ratio of energy stored to energy lost by the resonator, while the filling factor is the fraction of total RF magnetic field power entering the resonator that is incident upon the sample. Higher Q allows larger detectable changes during absorption and hence improves signal intensity.

The resonator must be a mechanically stable structure and should make most efficient use of the space within the magnet. Space constraints present a major consideration in the choice of the resonator design for EPR imaging. Innovations in resonator design, which enable automatic coupling adjustment and frequency tuning[113,114], can be used to suppress motion-induced distortion that occurs in biological samples.

In recent years much effort has been focused on the development of lumped-parameter RF sample cavities for L- and S-bands. Two major types of such resonators, namely loop-gap and reentrant, have been introduced and extensively discussed in literature [115,116].

Loop-gap resonators (LGR) provide straightforward design and high filling factors compared to standard distributed parameters RF cavities. However, due to the open structure of the inductive loop element, LGRs have significant radiation losses unless a shield is provided. The need for the shield leads to problems in achieving an optimum magnitude of modulation field and at least a 20% increase of overall resonator dimensions. A sketch of a loop-gap surface resonator design, originally developed by Bacic *et al.*[117] is shown in Figure 8a. The reentrant resonator (RER design) was introduced and described in great detail by Sotgiu[116]. Since the resonant structure of the RER forms a closed volume, it does not require any additional shield, thus providing substantial space savings as compared to LGRs. A number of RERs constructed of ceramic silver plated material are also reported[118] offering improved rigidity and stability. Figure 8b shows an RER resonator design for L-band EPR.

4.1.5 Modulation Coil and Signal Channel—To improve the system sensitivity, it is a common practice in CW-EPR to modulate B_{ext} by adding an oscillating the magnetic field using a pair of modulation coils and to detect the signal using a phase-locked loop detector which is also called a phase-sensitive or a lock-in detector. The lock-in detector compares the EPR signal from the crystal with the reference signal which comes from the same oscillator that generates the magnetic field. The lock-in detector only accepts the EPR signal that is phase coherent to the reference signal[119]. The advantages of lock-in detection include less $1/f$ noise from the detection diode and elimination of the baseline instabilities due to drift in DC

electronics. It is important to note that for certain data collection method, rapid scan[120] for instance, no field modulation is applied and the absorption signal is recorded directly.

4.2 Tuning Parameters

There is array of instrument parameters which, when adjusted properly, can improve the performance of the spectrometer or imager for a given oximetry application. Selection of these parameters depends on the experimental setup, such as sample size, and the nature and extent of information sought.

Here we briefly mention some of the important instrument setup parameters which affect the SNR and hence the acquisition time and the accuracy of final results. (i) Radiation Frequency: An increase in the radiation frequency improves the SNR, but at the same time results in unwanted nonresonant absorption and reduction in penetration depth. (ii) Magnetic Gradient: An increase in magnetic gradient strength thermally burdens the gradient coils and degrades SNR, but improves spatial resolution. (iii) RF Power: An increase in RF power improves SNR but may also result in heating of the sample and power saturation induced line broadening. (iv) Quality Factor: High Q of a resonator, along with critical coupling, improves SNR but also leads to extra sensitivity to sample motion. (v) Modulation Amplitude: An increase in modulation amplitude improves SNR but exerts extra burden on the modulation coils and also results in lineshape distortion, which is generally corrected by post-processing[121]. (vi) Sweep Time: Increasing the magnetic field sweep time for each spectral scan improves SNR but prolongs the acquisition time, which can be very critical for *in vivo* applications. (vii) Number of Projections: For imaging, collecting data along a large number of orientations generally improves reconstruction quality but only at the cost of increased acquisition time.

5 Data Collection and Processing

5.1 Spectroscopy

In spectroscopy, the measurements take place in the absence of a magnetic field gradient. Hence, no information is captured regarding the spatial distribution of the spin probe. The collected information is solely limited to the shape of the composite spectrum. If there are more than one paramagnetic species present in the sample, the observed signal is the superposition of individual spectra.

5.1.1 Data Collection—Although in principle it is possible to sweep the RF frequency for a fixed B_{ext}, the related hardware challenges make it an unattractive option. Therefore, in EPR the spectrum is generally observed, in the presence of a fixed frequency excitation, by sweeping B_{ext},

$$B_{ext}=B_0+B_\delta \tag{10}$$

where B_δ represents field sweep, B_0, defined by Eq. 2, is the magnetic field strength at which magnetic resonance occurs. For a majority spin probes, the lineshape l belongs to family of parametric functions such as Lorentzian, Gaussian, or Voigt[122]. A Lorentzian lineshape with full-width at half-maximum (FWHM) linewidth W and amplitude, κ, which is the area under the absorption curve, is defined in Eq. 11,

$$l(W,\kappa)=\frac{\kappa}{\pi}\frac{0.5W}{(B_\delta)^2+(0.5W)^2} \tag{11}$$

As mentioned earlier, SNR can be improved by modulating the magnetic field and observing the first harmonic, which, for small modulation amplitude B_m, represents the first derivative[123] of l as shown in Figure 9.

5.1.2 Data Processing—For oximetry, linewidth for an oxygen sensitive spin probe increases monotonically with the pO_2 to which the spin probe is exposed. Hence, measuring W can provide a direct reading of pO_2. For spectroscopy, the data processing involves estimating linewidth from noisy measurements. For high SNR, a direct peak-to-peak measurement can be used to estimate linewidth. For low SNR, however, curve fitting, shown in Figure 10 can be applied to improve robustness. For curve fitting, the measured noisy spectrum is fitted to a known parametric lineshape of the spin probe.

5.2 Spatial Imaging

Spatial EPR imaging is capable of providing the distribution of paramagnetic spins in the 1D, 2D, or 3D spatial domain[124,125] $\boldsymbol{u} \in \square^d$. Application of a magnetic field gradient $\boldsymbol{g}_u$ is used to resolve the spatial distribution of spin probes. In spatial imaging, it is assumed that the lineshape of the spin probe is spatially invariant. In cases where lineshape changes with the location (possibly due to changes in the environment such as variations in pO_2) or where there are multiple spin probes with different lineshapes, it may not be possible to provide an accurate distribution of the spin probes using purely spatial EPR imaging. Although spatial imaging is not used for oximetry, a basic understanding would help the reader comprehend the concept of spectral-spatial imaging which is discussed later.

5.2.1 Data Collection—The net external magnetic field in the presence of a gradient $\boldsymbol{g}_u$ becomes,

$$\begin{aligned} B_{\text{ext}} &= B_0 + B_\delta + \langle \boldsymbol{g}_u, \boldsymbol{u} \rangle \\ B_{\text{ext}} - B_0 &= B_\delta + \langle \boldsymbol{g}_u, \boldsymbol{u} \rangle \end{aligned} \tag{12}$$

where $\langle .,. \rangle$ represents the inner product. The resonance condition is only met where $B_\delta + \langle \boldsymbol{g}_u, \boldsymbol{u} \rangle = 0$. Each term in Eq. 12 has units of magnetic field, but can be converted to spatial units by dividing both sides by $-|\boldsymbol{g}_u|$.

For EPR imaging, data is collected in the form of projections. A projection p is computed by the Radon transform (RT) of a 2D or 3D object f,

$$p(\rho, \widehat{\boldsymbol{g}}_u) = \int_{\boldsymbol{u}} f(u) \delta(\rho - \langle \widehat{\boldsymbol{g}}_u, \boldsymbol{u} \rangle) d\boldsymbol{u} \tag{13}$$

where $\rho = -B_\delta / |\boldsymbol{g}_u|$ and $\hat{\boldsymbol{g}}_u = \boldsymbol{g}_u / |\boldsymbol{g}_u|$ Here, $\langle \hat{\boldsymbol{g}}_u, \boldsymbol{u} \rangle$ is the plane to be integrated, and ρ is the distance of this plane from the center of image space as shown in Figure 11. For a spin probe with lineshape $l_\rho(W_\rho, \kappa)$, each measured projection is a convolution of a true projection obtained by Radon transform and the lineshape $l_\rho(W_\rho, \kappa)$.

$$p_l(\rho, \widehat{\boldsymbol{g}}_u) = p(\rho, \widehat{\boldsymbol{g}}_u) \otimes l_\rho(W_\rho, 1) \tag{14}$$

where $\otimes$ stands for convolution in the first variable. Note, $l_\rho(W_\rho, \kappa)$ is the lineshape in spatial domain, and $l(W, \kappa)$ is the lineshape in terms of magnetic field and is related to the former by

$$l(W,\kappa)=\frac{1}{|\widehat{g_u}|}l_\rho(W_\rho,\kappa) \tag{15}$$

where $W = |\mathbf{g}_u|W_\rho$.

5.2.2 Data Processing—For EPR spatial imaging, data processing involves reconstructing 2D or 3D images from a set of collected projections. It is a linear inverse problem and has been discussed extensively[126]. Generally, filtered backprojection (FBP) or direct Fourier method is used to reconstruct the image. For a small number of projections, the reconstruction using FBP may result in undesired streak artifacts. To overcome this problem, iterative reconstruction methods[127,128] can be used to improve the reconstruction quality at the cost of reconstruction time. The effect of spatial blurring, represented in Eq. 14, can be suppressed by applying higher gradient $|\boldsymbol{g}_u|$ For situations where the application of a large enough gradient is not possible due to SNR degradation or hardware limitations, deconvolution[129] is applied either before or during the reconstruction. A common practice is to perform deconvolution on individual projections before the reconstruction. The most common method of performing deconvolution is by a point-by-point division, in the discrete Fourier domain, of each measured 1D projection by the measured or calculated lineshape. To avoid, divide-by-zero problem, each projection is lowpass filtered before the deconvolution.

5.3 Spectral-Spatial Imaging

For samples having variable linewidths, which is the case for EPR oximetry, it is not possible to obtain an accurate map of the spin distribution using data-collection and image-reconstruction procedures used for purely spatial EPR. Furthermore, the information obtained by purely spatial EPR imaging is limited to the spin density and cannot resolve the nature of the spins at each spatial volume element (voxel). To overcome this limitation, an additional spectral dimension is considered to capture the lineshape at each voxel. The imaging technique that includes a spectral dimension along with one or more spatial dimensions is termed spectral-spatial imaging[130].

5.3.1 Data Collection—For spectral-spatial imaging, the spatial information is captured by collecting projections along different spatial orientations of the gradient vector, while the spectral information is captured by varying the gradient strength in addition to the orientation. Spectral-spatial imaging can be performed in 1, 2 or 3 spatial dimensions giving rise to 2D, 3D, or 4D spectral-spatial images, respectively. Conceptually, the data acquisition in n spatial and one spectral dimension is similar to the data acquisition in n +1 spatial dimensions. To augment the spectral dimension, an addition angle, θ, also called spectral angle, is introduced. The spectral angle is defined as

$$\tan\theta = \pm \frac{|g_u|\Delta L}{\Delta B} \tag{16}$$

where ΔL and ΔB define the size of the field-of-view along spatial and spectral dimensions respectively. Figure 12 shows the data collection scheme for a 2D spectral-spatial object.

5.3.1 Data Processing—Conceptually, image reconstruction for spectral-spatial imaging is identical to spatial imaging with the exception of an added dimension. Generally, after rescaling of the collected projections to accommodate for the signal loss at higher gradient strengths, FBP is applied to obtain a spectral-spatial image. For high gradient projections, time

averaging is applied to partially compensate for the SNR loss. Also, due to limited gradient strength, it is not possible to collect projections with the spectral angle values in the vicinity of $\pm\pi/2$, which leads to the problem of image recovery from an incomplete dataset. This is usually referred to as limited-angle tomography and has been studied extensively[131]. Spectral-spatial imaging is generally time consuming, especially in 4D where hundreds or even thousands of projections are collected with each requiring a sweep time of a couple of seconds or more.

5.4 Recent Developments

EPR oximetry, especially when performed over 3 spatial dimensions, is time consuming, which has adversely affected the wide use of EPR for clinical applications. Several innovations, ranging from improved hardware designs to optimized data collection and processing schemes, have been implemented to reduce the data collection time to the levels suitable for *in vivo* studies. However, there is still room for further acceleration of data acquisition before EPR can be declared a serious contender for clinical oximetry. In this section, we look at some of the data collection and processing methodologies adopted by the EPR community to speed up data acquisition.

5.4.1 Pulsed System—In CW EPR, the data are collected by exposing the sampling to a fixed frequency excitation and sweeping the magnetic field gradually. It may take a couple of seconds or more to acquire one projection. Therefore, acquiring data for higher dimensions, where hundreds and even thousands of projections may be required, becomes impractical for many applications where conditions may change rapidly. Pulsed EPR, on the other hand, has the potential to reduce the acquisition time substantially[106]. However, there are numerous technical challenges still to be addressed before pulsed EPR overtakes CW EPR for broad EPR applications. In pulsed EPR, the excitation is provided by a train of short RF pulses, and the emitted signal from the spins, called free induction decay (FID), is digitized and recorded. The EPR spectrum can be obtained by simply applying the Fourier transform to the FID. Although the basic principle of the pulsed EPR spectrometer is similar to that of NMR, extremely short relaxation times for EPR make the instrumentation much more challenging. At low frequencies, the dead time of an EPR resonator, defined as the time required by the resonator to dissipate the RF energy, can approach the relaxation times of many commonly used spin probes, making it extremely difficult to collect the data. Therefore, spin probes with longer relaxation times are highly preferred to exploit the advantages of the pulsed system. Lately, there has been a renewed interest in the development of a low frequency pulsed EPR system[132].

5.4.2 Overmodulation—Modulation amplitude is another important parameter that affects the data quality. In the presence of a modulating field $B_m\cos\omega_m t$ and without the application of the gradient, Eq. 12 can be written as

$$B_{\text{ext}} - B_0 = B_\delta + B_m\cos\omega_m t \tag{17}$$

where B_m is the modulation amplitude. Eq. 11 then becomes

$$\begin{aligned} l(W,\kappa,B_m) &= \frac{\kappa}{\pi}\frac{0.5W}{(B_\delta+B_m\cos\omega_m t)^2+(0.5W)^2} \\ &= \frac{\kappa_0}{(2/W)^2(B_\delta+B_m\cos\omega_m t)^2+1} \end{aligned} \tag{18}$$

where $\kappa_0 = 2\kappa/\pi W$ is the amplitude of l at $B_\delta = 0$. In terms of a Fourier series

$$l(W,\kappa,B_m)=\kappa_0\left(a_0+\sum_{n=1}^{\infty}a_n(W,B_\delta,B_m)\cos n\omega_m t\right) \tag{19}$$

where

$$a_n=\frac{\omega_m}{\pi}\int_{-\pi/\omega_m}^{\pi/\omega_m}\frac{0.5W\cos n\omega_m t}{(B_\delta+B_m\cos\omega_m t)^2+(0.5W)^2} \tag{20}$$

The closed form expression for a_n can be calculated by contour integration. In order to observe the first harmonic, a_1, the signal at the output of the lock-in detector is multiplied with $\cos\omega_m t$ and lowpass filtered. For B_m much smaller than W, the first harmonic is approximately equivalent to the first derivative of the absorption signal. When B_m increases so does the signal intensity, but the signal gets distorted and no longer remains Lorentzian as shown in Figure 13. Fortunately, this modulation induced distortion is well characterized[121]. In order to improve the SNR, the use of B_m that is much larger than W has been reported[133,134].

5.4.3 Rapid Scan—In traditional CW EPR, a slow linear scan is made to collect a spectrum or a projection. The magnetic field modulation and the lock-in detection are applied to increase SNR. In rapid scan, the magnetic field is swept back-and-forth at a high rate, usually in kHz range, and the absorption signal is recorded directly without any field modulation or lock-in detection. For scan rates comparable to the relaxation times, a distortion is introduced in the spectrum. Fortunately, this distortion is well characterized using Bloch equations and can be easily accounted for by post-processing[135]. When the RF power is optimized for a given scan rate, the signal intensity is enhanced by up to a factor of three relative to the conventional slow scan lock-in detection[120]. Also, the SNR for rapid scan is inversely proportional to the magnetic field sweep width as compared to the lock-in detection where the SNR is inversely proportional to the square of the magnetic field sweep width. The relative performance of rapid scan has been evaluated for EPR recently[136]. High scan rates, usually in the kHz range, make rapid scan the method of choice for EPR imaging of a moving object such as beating heart.

5.4.4 Iterative Reconstruction—Iterative methods, also known as series expansion reconstruction methods or algebraic reconstruction methods, have been used for tomographic reconstruction for the last few decades[127]. These methods are based on the discretization of the image domain prior to any mathematical analysis, which is in contrast to the transform methods, such as the FBP, where the continuous problem is only discretized as the last step of the reconstruction process[137].

Iterative methods are computationally intensive, but the reconstruction is usually superior to the FBP. Algebraic reconstruction technique[138] (ART) is a common iterative method used to reconstruct data from projections. The most attractive feature of ART, and other similar iterative techniques, is its ability to merge a variety of constraints into the iterative process. For example, a nonnegativity constraint can be readily implemented by setting the negative portions of the estimate to zero in each iteration. Further, the iterative methods do not require projections to be uniformly distributed and hence the missing angle problem is handled seamlessly. A comparison of ART reconstruction and FBP reconstruction from 20 noiseless projections for a 2D digital Shepp-Logan phantom is represented in Figure 14. A strong streak artifact is visible for the FBP reconstruction.

For spatial imaging, another major advantage of iterative methods is their ability to incorporate the deconvolution step into the interactive scheme, eliminating the need for a separate deconvolution which generally yields poor results. Computationally efficient algorithms have been reported to carry out the iterative reconstructions from projection data[139]. Recently, a number of iterative methods have been suggested for EPR image reconstruction, each differing in the cost function to be minimized[140,141].

5.4.5 Single-Point Imaging—Single-point imaging (SPI) or constant-time imaging[142] is a special way of collecting data using pulsed EPR. In SPI, for every pulsed RF excitation, a single data point of the FID after a fixed delay in the presence of static magnetic field gradients is acquired. It is analogous to performing pure phase encodings in all dimensions to fill the *n*D Fourier domain point-by-point. Since the phase-encoding time (the fixed delay after excitation) remains constant for a given image data set, the spectral information (lineshape) is automatically deconvolved, providing well-resolved pure spatial images. Therefore, SPI has the potential to provide high resolution artifact free images which can be useful for many biological applications. For spectral-spatial imaging, the spectral information can also be extracted from a series of SPI images each corresponding to a different delay from the excitation pulse. Since only one data point is recorded per excitation, acquisition times for SPI can be longer than that for CW EPR imaging.

5.4.6 Spinning Gradient—Conventionally, the main magnetic field is slowly swept for a given gradient orientation, and the process is repeated for a set of different gradient orientations. For such an acquisition, the adjacent data points in each projection are highly correlated, resulting in data redundancy. For spinning gradient, on the other hand, the main magnetic field is kept fixed while the gradient orientation is rotated rapidly, and the process is repeated for different values of the main magnetic field. The resulting data have lesser redundancy and generate better quality images. The performance of spinning gradient-based data acquisition has been explored for EPR by Deng *et al.*[143]. Usually, special low-inductance gradient coils are used to spin the gradients rapidly. If the spinning frequency is low (< 100 Hz), the existing systems with phase-sensitive detection can be used without any major hardware modifications.

5.4.7 Multisite Oximetry—Swartz *et al.*[144] have pioneered an approach coined “multisite oximetry”. A single favorable gradient direction is assumed for which each of several isolated implants is resolved. The EPR lineshape for the spin probe material is assumed to be Lorentzian, with unknown linewidths. A spectrum is recorded for two gradient magnitudes. The linewidths are then estimated by nonlinear least-squares curve fit; the curve fit is computed on intervals for which spectral components are nonoverlapping. In this manner, the linewidth of each spin probe site is estimated without reconstruction of the entire spectral-spatial object. The key assumption is that lineshapes are resolved with a single, one dimensional magnetic field gradient. The approach has been applied for *in vivo* oximetry of transient focal cerebral ischemia in the rat[134]. Recently, Som *et al.*[145] proposed a model based approach to solve the multisite problem with much more favorable constraints on the experimental setup. For four isolated implants of a particulate spin probe, acquisition time reduction of 40:1 was reported in this study.

5.4.1 Digital Detection—Digital detection[146], for both pulsed and CW EPR, has been gaining interest lately. There are several classes of digital detectors proposed for EPR[147], including homodyne detection followed by A/D conversion, superheterodyne detection followed by A/D conversion, time-locked subsampling (TLSS) of intermediate frequency carrier, and TLSS of RF carrier. In TLSS of intermediate frequency carrier, RF signal is first bandpass filtered and downconverted to intermediate frequency and then subsampled in a time-locked manner. For CW with field modulation, main advantage of digital detection is the ability

to simultaneously collect data across multiple harmonics of both absorption and dispersion signals. With the quality of digital hardware improving rapidly, digital detection will gain further popularity in the years to come.

5.4.1 Overhauser Enhanced MRI—Overhauser enhanced MRI (OMRI) combines the advantages of MRI with the sensitivity of EPR. It is a double resonance technique[148] that is based on the Overhauser effect[149]. In the presence of an exogenous, soluble spin probe, MRI measurements are recorded both with and without RF irradiation. The map of the difference between the intensities of two MRI reconstructions is related to the linewidth map of the spin probe. OMRI has been applied to study oxygenation of murine tumors[150]. Despite all the advantages, high RF power and long RF irradiation times are required to obtain good signal enhancement in OMRI[151].

6 EPR Oximetry Spin Probes

In living systems, free radicals and other paramagnetic species are either present at a very low concentration or have very short relaxation times, prohibiting their direct measurement. For instance, the relaxation time (T_1) for molecular oxygen dissolved in several solvents was found to be approximately 7.5 ps[98], making the direct measurement using current EPR spectrometers impossible. Therefore, in all EPR oximetry applications, an exogenous material, called a spin probe or spin label, is delivered into the biological system, and the interaction of endogenous paramagnetic specie, molecular oxygen in the case of oximetry, with the spin probe is used to quantify the endogenous specie.

6.1 Development

For the past two decades, several spin probes for EPR oximetry have been developed and extensively analyzed for biological applications. There are two classes of spin probes, namely, soluble and particulate spin probes. An appropriate choice of spin probe depends upon the experimental setup and the nature of desired information. Some of the pertinent properties of a spin probe include: (i) Spin Density: A higher spin density leads to higher SNR and ensures administration of smaller quantities of spin probe and shorter acquisition times. (ii) Sharp lineshape: A single sharp lineshape improves SNR and reduces data acquisition times. (iii) Power Saturation: RF power saturation broadens lineshape and degrades SNR. A high threshold for power saturation allows for stronger RF irradiation without the saturation induced broadening. (iv) Oxygen Sensitivity: It is defined as the change in linewidth for unit change in pO_2. Generally, higher oxygen sensitivity is desirable for accurate pO_2 measurements, but excessive broadening of lineshape due to high oxygen sensitivity may lower the SNR. (v) Biostability: Biostability of a spin probe ensures that it does not degrade or lose it properties in a biological environment. (vi) Chemical Toxicity: It measures the extent of damaging effect, besides the injury caused by the implantation, which a spin probe may have on biological system. (vii) Distribution: It refers to spatial distribution of the spin probe in the sample. Soluble spin probes tend to distribute more evenly while particulate spin probes tend to stay localized. Table 1 summarizes anoxic linewidths and oxygen sensitivities for commonly used oximetry spin probes.

6.1.1 Soluble Spin Probes—For oximetry, the main advantages of soluble spin probes include even distribution in the sample, access to deep organs, and automatic removal (by bioreduction or excretion) from the *in vivo* system. Nitroxides were among the first spin probes used for EPR oximetry[152]. Use of both five-and six-membered nitroxides has been extensively reported for a wide array of EPR oximetry applications[153–155]. Some of the commonly used nitroxides are shown in Figure 15a and 15b.

Nitroxide synthesized with ^{14}N has an EPR spectrum with three lines while the nitroxide synthesized with ^{15}N exhibits an EPR spectrum with two lines. As compared to particulate spin probes, the EPR signals from nitroxides exhibit low SNR and poor sensitivity to oxygen. A number of improvements, including use of perdeuterated nitroxides[167] and encapsulation of nitroxides in lipophilic environments[168], have been suggested to improve oxygen sensitivity. The synthesis of nitroxides can be manipulated to affect their bindings and hence distribution in a biological sample. For instance, a charged nitroxide cannot permeate the cellular membrane while a neutral nitroxide can, giving a spin probe distribution in both intracellular and extracellular compartments[169]. Howard Halpern, over the last twenty five years, has contributed immensely to the development of nitroxides for EPR measurements[170,171].

Nycomed Innovations Inc. developed[172] a family of trityl radicals (Figure 15c) bearing twelve sulfur atoms. These are analogs of triphenyl methyl radicals and have been synthesized on a large-scale and used for a variety of EPR oximetry applications[173–175]. Trityl radicals, also referred as TAM, offer a single sharp lineshape and an order-of-magnitude improvement in SNR over other commonly used soluble spin probes. Recently, synthesis of other derivatives of TAM have also been reported[176–178]. Perchlorotriarylmethyl (PTM) radicals (Figure 15d) constitute another important trityl-type radical used for EPR oximetry. Perchlorotriphenylmethyl triester radical (PTM-TE) was synthesized, as outlined in Scheme 1, by a facile 3-step synthesis[179] using Friedal-Crafts reaction of tetrachlorobenzene with chloroform followed by ethoxycarbonylation and subsequent oxidation. Bratasz *et al.*[180] reported on the development of an injectable spin probe formulation, consisting PTM-TE radical dissolved in hexafluorobenzene (HFB), for *in vivo* oximetry and imaging of oxygen concentration in tissues. PTM-TE was evaluated for its oxygen sensitivity, biostability, and distribution in a radiation-induced fibrosarcoma (RIF-1) tumor transplanted into C3H mice. Some of the favorable features of the spin probe are: a single narrow EPR peak (anoxic linewidth, 410 mG), high solubility in HFB (> 12 mM), large linewidth sensitivity to molecular oxygen (~ 17 mG/mmHg), good stability in tumor tissue (half-life: 3.3 h), absence of spin-spin broadening (up to 12 mM), and lack of power saturation effects (up to 200 mW).

6.1.2 Particulate Spin Probes—The main advantages of particulate spin probes include high spin density, which leads to high SNR; higher sensitivity to oxygen; and long term *in vivo* stability. Particulate spin probe-based oximetry is ideal for making repeated measurements over an extended duration in live animals. A wide array of naturally occurring, semi-synthetic, and synthetic particulate spin probes have been developed for EPR oximetry.

Carbon-based materials including coals (such as funinite[161,181] and gloxy[163]), chars[182,183] (either prepared from coals or synthesized from carbohydrates, wood, or other materials) and carbon black[184] (India Ink) have been extensively used for *in vivo* EPR oximetry. Thus far, India Ink remains the only spin probe approved for *in vivo* clinical use, both in the USA and Europe. In fact, EPR oximetry using India Ink has already been reported on human subjects[95]. Despite a strong EPR signal and easy availability, poor oxygen sensitivity (charcoals), broad lineshape (India Ink), nonlinear relationship between linewidth and pO_2 (almost all carbon-based particulate spin probes), lack of quality control (coals), poor stability (chars), and presence of nonparamagnetic components in the spectrum (almost all carbon-based particulate spin probes) may render carbon-based particulate spin probes an unattractive option for *in vivo* applications.

Lithium phthalocyanine (LiPc) (Figure 16a) was the first synthetic particulate molecule to be extensively investigated for biological applications[156]. LiPc is synthesized by electrochemical oxidation of Li_2Pc[185–187]. The EPR spectrum of LiPc is characterized by a single lineshape with anoxic linewidth of ~20 mG. LiPc has been studied for long-term *in vivo* oximetry measurements[188]. The shortcomings of LiPc are: saturation at lower power, lack of quality

control, a nonlinear relationship between linewidth and pO_2, and lack of long-term stability in tissues[156]. Recently, derivatives of LiPc, such as phenoxy-substituted LiPc (lithium 1,8,15,22-tetraphenoxyphthalocyanine, LiPc-α-OPh), shown in Figure 16a, have been developed[158] using electrochemical methods. As compared to LiPc, the derivative LiPc-α-OPh shows improved linearity of linewidth vs. pO_2 curve, higher oxygen sensitivity, and improved stability for *in vivo* applications. The schematic for LiPc-α-OPh synthesis is given in Scheme 2.

Another synthetic crystalline spin probe, lithium naphthalocyanine[159] (LiNc), shown in Figure 16b, has been widely studied for EPR oximetry applications. The LiNc shows higher spin density, a broader range of linear response to oxygen partial pressure, and more favorable power saturation properties when compared to LiPc[189]. However, the chemical properties of LiNc limit its attractiveness for biological oximetry applications. First of all, it is difficult to synthesize this material in a pure form, and secondly, it has shown limited stability and responsiveness in tissues[189]. Recently, Pandian *et al.*[190] have reported an improved chemical procedure to synthesize LiNc crystals in pure form with sustained oxygen sensitivity in tissues. The schematic for LiNc synthesis is shown in Scheme 3.

In efforts to develop better spin probes for EPR oximetry, Pandian *et al.*[160] reported the preparation of a new derivatized radical, lithium 5,9,14,18,23,27,32,36-octa-*n*-butoxy-2,3-naphthalocyanine (LiNc-BuO). Synthesis for LiNc-BuO is shown in Scheme 4. The spin probe was synthesized[191] from lithium metal and Nc-BuO in *n*-pentanol. The metal-free octa-*n*-butoxy-substituted naphthalocyanine (Nc-BuO) macrocyclic ligand readily reacted with lithium pentoxide to give dilithium octa-*n*-butoxy-naphthalocyanine (Li_2Nc-BuO), followed by oxidation to give LiNc-BuO radical which formed as needle-shaped, dark-green microcrystals, 5–10 μm in diameter and 50–150 μm in length. Preliminary studies of this material showed that the spin probe was stable in tissues and responsive to O_2 for more than 6 months[160].

The crystal structure of LiNc-BuO contains strongly coupled dimers of LiNc-BuO molecules, which favors a high degree of spin exchange, and results in a single sharp EPR line. The molecular packing leads to a structure with open channels large enough (10×6 $Å^2$) for the penetration of small diatomic paramagnetic molecules such as oxygen (O_2) and nitric oxide (NO), as well as the larger triatomic molecules such as nitrogen dioxide (NO_2). The EPR linewidth of LiNc-BuO is extremely sensitive to the concentration of paramagnetic gases in the pressure range of 0–760 mmHg. The effect of oxygen on LiNc-BuO is reversible without any signs of permanent adsorption or chemical oxidation. The time response of the effect of oxygen is extremely rapid (0.24 s). The paramagnetic gas-sensing properties of LiNc-BuO are attributed to the open molecular framework of the crystal structure. The oxygen sensitivity curves of LiNc and LiNc-BuO are shown in Figure 17. Photograph of LiNc-BuO microcrystal and stacking of LiNc-BuO molecules within the microcrystal are shown in Figure 18.

6.2 Particulate Spin Probe Encapsulation

The particulate spin probes can be used in their crystalline form to sense molecular oxygen[94], but may have limitations associated with particle migration within the tissue and, potentially, with biocompatibility and chemical toxicity of particles directly exposed to tissue. Exposure of some spin probes to the *in vivo* environment degrades their oximetry properties over time[156,189]. Successful transformation of EPR oximetry into a powerful clinical tool requires long-term stabilization of the spin probes in tissue sites, protection of the spin probes from degradative conditions, and insulation between the spin probe and tissue to avoid potential chemical toxicity.

Several studies have approached this set of challenges by encapsulating crystalline spin probes in biocompatible, biostable, gas-permeable polymer matrices[192–195]. Some critical parameters

that need to be considered in the development of encapsulated oximetry spin probes include the cost of the encapsulating polymer, *in vivo* stability (mechanical and chemical) of the polymer material, and film oxygen permeability.

In the past, coating of carbon-based particulate spin probes using a number of biopolymers[13] has been reported. Encapsulation of LiPc using Teflon AF 2400 (TAF), cellulose acetate (CA) and polyvinyl acetate (PVAc) has also been reported. The coating of LiPc using TAF was performed by solvent evaporation approaches, which produced very thin TAF films[193]. While the oximetry properties of TAF-encapsulated LiPc were encouraging, the handling properties of the films were inconvenient. Thin TAF films were brittle and maintaining them intact during implantation and explantation was challenging. Thick, multilayer TAF encapsulation of oximetry particles was not feasible, owing to the low solubility of TAF in the available solvents.

To overcome these operational difficulties, Meenakshisumdaram *et al.*[196] recently proposed a simple and easy-to-use cast-molding and polymerization method, using PDMS, which allowed for the fabrication of mechanically-robust spin probe encapsulations. PDMS is a biocompatible, highly flexible, and highly oxygen permeable silicone polymer that has been used in a wide range of medical device and health care applications. Also, PDMS has been approved for use in human subjects and is one of the reference materials provided by the National Heart Lung and Blood Institute for standardized biocompatibility testing[197]. The method also provided the capability of covering the embedded oximetry crystals with multiple layers of PDMS for fully sequestering them from the *in vivo* environment, and improving their biotolerability. Figure 19 shows chips fabricated by the encapsulation of LiNc-BuO particulates in PDMS.

7 Applications of EPR Oximetry

EPR oximetry has been used extensively for cellular studies to measure intracellular and extracellular oxygen concentrations, oxygen consumption rate, and membrane permeability and structure[11]. It has also been developed as a powerful tool for localized measurements of oxygen in organs and tissues which is extremely helpful in investigating various physiological and pathophysiological conditions. Several studies have been conducted using EPR oximetry to measure oxygen in the brain, heart, gastrointestinal tract, skeletal muscle, liver, kidneys, skin, and other organs[94]. Due to limited penetration depth, the existing EPR techniques are restricted to studies involving small animals or topical regions of large animals. In this section, a few important applications of EPR are briefly discussed.

7.1 *In Vitro* Applications

One of early applications of EPR oximetry was to measure oxygen consumption rate in tumor cell suspensions[198,199]. Two models, closed-chamber and open-chamber, were developed. In the closed-chamber model, the sample was isolated from the surrounding using oxygen impermeable medium. The oxygen consumption rate was quantified by measuring the overall oxygen concentration as a function of time in the sample. In the open-chamber model, the oxygen consumption rate was quantified by measuring the amount of oxygen diffusing through an oxygen permeable membrane, such as Teflon or methyl pentene polymer[152], separating the sample from the surroundings. Recently, EPR oximetry has also been shown to successfully monitor the intracellular and extracellular oxygen simultaneously by using two different spin probes[174,200]. One spin probe was internalized in the cells and reported the intracellular pO_2, while other particulate spin probe stayed outsides and reported the extracellular pO_2 values.

EPR oximetry has also been applied to study oxygen transportation both across and within a lipid bilayer model membrane[90]. This method was used to obtain profiles of oxygen transport parameter which, in turn, was used to evaluate the oxygen permeability coefficient of the

membrane[91]. In addition, oxygen transport parameter profiles have also been used to study membrane structure. The DOT method[201] (method of discrimination by oxygen transport), for instance, was effectively used to indicate the existence of lipid domains which exhibit slow oxygen transport rate. EPR oximetry has also been utilized to study the effects of membrane modifiers such as cholesterol[202], carotenoids[203], and transmembrane α-helical peptides[204] on oxygen transportation across the membrane. A book chapter by Subczynski and Swartz[11] treats the topic of *in vitro* EPR oximetry applications in detail.

7.2 *In Vivo* Applications

In vivo EPR oximetry applications generally include the study of oxygenation of several tissues and organs under various pathophysiological conditions. Exciting *in vivo* applications of EPR oximetry have emerged in the last two decades, but continuous development of oxygen-sensitive spin probes coupled with technical advancements in the instrumentation promises that more applications will follow. Here, we visit some of the widely studied *in vivo* applications of EPR oximetry.

7.2.1 Cancer/Tumor Applications—Tumor hypoxia is strongly linked to poor treatment outcome from chemo- or radiotherapy in several human malignancies[205]. Hypoxic tumors are biologically more aggressive, and it has been reported that hypoxic sarcoma or cervical cancers[27,206] tend to metastasize faster. More recently, it has also been reported[207] that ovarian cancer cells grown in a hypoxic environment tend to be more resistant to common chemotherapies than the cancer cells grown under normoxia. The fact that poorly oxygenated tumors are more aggressive and less susceptible to treatment suggests that tumor oxygenation status is an important parameter for cancer treatment[208]. The observation of substantial inter- and intra-tumor heterogeneities among tumors of similar histology and sites further emphasizes the importance of the measurement of hypoxia in individual tumors patients. The ability to monitor changes in the pO_2 before and after treatment could have profound implications for the planning of effective therapeutic strategies[209]. In particular, radiotherapy could benefit from modulated treatment based on regional variations in pO_2.

While these tumor oximetry studies demonstrate the clinical potential of *in vivo* oximetry, they also point to the limitations of commonly employed oximetry methods. For instance, measurements involving electrodes are highly invasive and cannot be used for repeated measurements from the same site, and measurements using PET involve exposure to ionizing radiation. EPR oximetry avoids some of the important limitations associated with other methods. It is a minimally invasive method that allows for repeated measurements and possesses high sensitivity to *in vivo* oxygen levels. Elas *et al.*[173] conducted a comparative study quantitatively correlating EPR oximetry using a trityl spin probe with OxyLite based oximetry.

Halpern *et al.*[210] conducted spectral-spatial imaging, in one spatial dimension, to provide a quantitative map of pO_2 distribution across the tumor using a soluble spin probe. In another study[211], the same group examined the affect of breathing in perfluorocarbon/carbogen on the oxygenation of fibrosarcomas. Gallez *et al.*[153] used nitroxides for assessing perfusion, oxygenation, and viability of tissues in murine tumor models. Krishna *et al.*[150] reported coregistration of tumor anatomy with pO_2 distribution using OMRI. Bratasz *et al.*[180] reported the development of an injectable spin probe formulation, consisting of PTM-TE radical dissolved in hexafluorobenzene, for *in vivo* oximetry under two different breathing environments. These results are summarized in Figure 20.

EPR oximetry employing particulate spin probes has also been used extensively to measure murine tumor oxygenation. Particulate spin probes are more suitable for long-term measurements and require onetime implantation at one or more locations in the region of interest. Measurements over several days or weeks enable the tracking of tumor oxygenation.

Goda *et al.* studied changes in oxygen tension in experimental tumors, RIF-1 tumor and mouse mammary tumor (MTG-B), after a single dose of X-ray irradiation. Ilangovan *et al.*[212] reported pO_2 mapping of tumors by co-implanting LiPc particulates with RIF-1 cells subcutaneously in the murine leg. Spectral-spatial imaging can be performed to map the spatial distribution of oxygen concentration in a tumor. Using a similar model, Bratasz *et al.*[213] conducted studies using LiNc-BuO to report pO_2 maps before and after a single dose of 30 Gy X-ray irradiation. The results are summarized in Figure 21. Hou *et al.*[214] has investigated the temporal effects of single or fractionated radiotherapy on subcutaneous RIF-1 tumor using multisite oximetry[144]. The purpose of the study was to determine the therapeutic outcomes when the timing of fractionations is guided by tumor pO_2. In another interesting study, the role of Granulocyte-macrophage colony-stimulating factor (GM-CSF) in the inhibition of breast cancer growth has been studied using EPR oximetry[215]. Figure 22 shows the effect on GM-CSF on tumor size. Murine tumor oximetry using encapsulated particulate spin probes has been reported[216,217]. A review article by Gallez *et al.*[218] provides a well-rounded account of EPR tumor oximetry.

7.2.2 Cardiac Applications—Fluctuations in free radical generation, oxygenation, and nitric oxide concentration carry importance in a variety of cardiovascular diseases. Cardiac oximetry imposes a great technical challenge due to cardiac motion. EPR oximetry in isolated perfused rat hearts has been demonstrated[110,219]. Studies have also been conducted for isolated beating heart[16,220] and heart *in situ* models[221], with both soluble and particulate spin probes.

Grinberg *et al.*[222] reported measurements of myocardial pO_2 by EPR oximetry in an isolated perfused rat heart during treatment with different cardioactive drugs: dobutamine, metoprolol, verapamil, vasopressin, and N omega-Nitro-L-Arginine Methyl Ester. The relationship of oxidative damage associated with ischemia/reperfusion (I/R) injury and the amount of oxygen in the heart has been focus in several studies. Ilangovan *et al.*[16] studied myocardial oxygen consumption rate as an index of postischemic recovery. Angelos *et al.*[223] studied the effect of hypoxic reperfusion and subsequent reactive oxygen specie (ROS) generation on cardiac function using EPR oximetry.

EPR oximetry has also been used to investigate the efficacy of various treatment options, including ischemic preconditioning and ROS-scavenging (antioxidant) drugs. For instance, studies by Zhu *et al.*[224] reported that ischemic preconditioning attenuated *in vivo* postischemic myocardial hyperoxygenation by improving myocardial oxygen consumption and decreasing ROS or reactive nitrogen specie generation after regional I/R. Another recent study[225] showed that sulfaphenazole (SPZ) protected the hearts from I/R injury. The overall aim of this study was to investigate the cardioprotective effect of SPZ and to delineate the involvement of NO, superoxide, and oxygenation and also to establish the signaling mechanism involved in cardioprotection in an *in vivo* rat model of acute myocardial infarction (MI). The beneficial effect, measured by hemodynamic functionality, correlated with a significant elevation of tissue oxygenation and bioavailability of NO.

Several recent studies utilized EPR oximetry to investigate the efficacy of stem-cell therapy for treating MI. Khan *et al.*[226] reported noninvasive long-term monitoring of *in situ* pO_2 during engraftment of stem cells in the infarct heart. Figure 23 displays the *in situ* oximetry data collected for over three months from a mouse heart transplanted with skeletal myoblasts (SM) using LiNc-BuO as a spin probe. In a separate but related study[227], the same author compared the oxygenation of infracted myocardial tissue with and without transplantation of SM. The myocardial pO_2 at the site of SM cell therapy was significantly higher when compared to the untreated group throughout the 4-week period as shown in Figure 24. The increased myocardial pO_2 positively correlated with neoangiogenesis and cardiac function.

In another study by Chacko *et al.*[228], bone marrow-derived mesenchymal stem cells (MSC) were transplanted in the infarct heart of rats, and showed significant reduction of infarct size followed by substantial recovery of tissue oxygenation, neovascularization, and cardiac function. In a recent report, Khan *et al.*[229] investigated the effect of hyperbaric oxygenation (HBO) on the engraftment of bone-marrow- derived rat MSCs transplanted in infarct rat hearts. HBO (100% oxygen at 2 ATA for 90 min) was administered daily for 2 weeks. The results showed (Figure 25) an increase in oxygenation levels reaching significance at 60 min followed by a return to baseline in about 2.5 h after the conclusion of HBO application in the noninfarcted hearts. Elevated oxygen levels were, however, sustained for more than two hours after the HBO administration in the infarcted heart. The results suggested that HBO treatment restored myocardial oxygenation to near normal levels in the infarct heart transplanted with MSCs.

7.2.3 Wound Healing Applications—Oxygen measurement in skin and other immediately underlying tissues is critical for evaluating the condition and treatment options for topical wounds, burns, and peripheral vascular disease. For these applications, where penetration depth is generally not a deciding factor, EPR oximetry holds a lot of promise for large animal models and potential clinical applications involving humans.

At the wound site, vasculature disruption leads to localized hypoxia[230]. Interestingly both hypoxia and hyperoxia, when present in moderation, have been known to induce angiogenesis[231] which plays a critical role in wound healing. However, hypoxia and hyperoxia, when present in the extreme, can derail tissue repair. Extreme hypoxia is unable to promote or sustain the growth of functional blood vessels. Extreme hyperoxia, on the other hand, can cause oxygen toxicity which can adversely affect the healing process. Oxygen therapy is commonly used in the wound clinics to treat wound hypoxia[232]. Schugart *et al.*[233] developed a mathematical model for addressing the role of tissue oxygenation on cutaneous wound healing. In a recent study, Lu *et al.*[234] studied decreases in oxygen levels due to Tibial fracture.

Oxygen measurements also provide a useful insight into the status, progression, and treatment of peripheral vascular diseases such as diabetic foot. Studies using this technique have been carried out in volunteers using India Ink and whole body clinical EPR instruments, and encouraging results have been reported[95].

7.2.4 Application of EPR Oximetry to Other Organs—EPR oximetry has also been studied for *in vivo* measurements in other organs and tissues such as liver, brain, kidney and skeletal muscle. Numerous studies, using EPR oximetry, have reported oxygen levels in the medulla and cortex of isolated perfused[163] and *in vivo*[235] kidney models. A number of pathophysiological conditions can affect liver pO_2. EPR oximetry also been used to study localized pO_2 in liver[164,236]. The value of pO_2 is known to affect the energetics of muscle function. EPR oximetry has been applied to study oxygenation of skeletal muscle[237]. The brain is quite vulnerable to pO_2 fluctuations. Several studies[238,239] show that EPR has been successfully used in small animal models to monitor brain oxygen over an extended duration of time. In addition, EPR oximetry has been used to evaluate the relationship between elevated levels of tissue pO_2 and healing of radiation damaged tissues.

8 Conclusions

Measurement of oxygen in biological samples, especially *in vivo*, has been of paramount interest. Several techniques have been developed for *in vivo* oxygen measurement, but no single technique has fully established itself for broad applications. EPR oximetry, due to its minimally invasive nature, capability to measure absolute pO_2, high sensitivity to oxygen, and ability to make repeated measurements, has emerged as a method of choice for wide array of biological applications. In the recent years, the number of laboratories and research groups contributing

to the development of EPR oximetry has increased. Significant strides have been made in spin probe synthesis and encapsulation, instrumentation development, and algorithm development for data collection and processing. Despite all the progress, translation of EPR oximetry to broad clinical applications have been hindered by lack of SNR at low frequencies, long acquisition times, and lack of FDA-approved spin probes suitable for implantation. Considering the progress made in the last decade, however, realization of clinical applications of EPR oximetry, especially for oncology, peripheral vascular disease, and wound healing, seems only few strides away.

Acknowledgments

We acknowledge the support of National Institute of Health for providing funding for several EPR related research projects, many of which have been discussed in this review. We also thank Brian Rivera for proofreading.

References

1. Lane, N. Oxygen: The Molecule that Made the World. Oxford University Press; Oxford: 2002.
2. Falkowski PG. Science 2006;311:1724. [PubMed: 16556831]
3. Jiang YY, Kong DX, Qin T, Zhang HY. Biochem Biophys Res Commun. 2009
4. Raymond J, Segre D. Science 2006;311:1764. [PubMed: 16556842]
5. Kulkarni AC, Kuppusamy P, Parinandi N. Antioxid Redox Signal 2007;9:1717. [PubMed: 17822371]
6. Prabhakar NR, Kumar GK, Nanduri J, Semenza GL. Antioxid Redox Signal 2007;9:1397. [PubMed: 17627465]
7. Sieck GC. J Appl Physiol 2004;96:375. [PubMed: 14660499]
8. Dewhirst MW, Klitzman B, Braun RD, Brizel DM, Haroon ZA, Secomb TW. Int J Cancer 2000;90:237. [PubMed: 11091348]
9. Swartz HM, Dunn JF. Adv Exp Med Biol 2003;530:1. [PubMed: 14562699]
10. Hunt TK, Rabkin J, Jensen JA, Jonsson K, Smitten KV, Goodson WH. World J Surg 1987;11:126. [PubMed: 3590819]
11. Subczynski, WK.; Swartz, HM. Biomedical EPR, Part A: Free Radicals, Metals, Medicine, and Physiology. Eaton, SR.; Eaton, GR.; Berliner, JL., editors. Kluwer Academic/Plenum Publisher; New York: 2005.
12. Dunn JF, Swartz HM. Methods 2003;30:159. [PubMed: 12725782]
13. Gallez B, Jordan BF, Baudelet C. Magn Reson Med 1999;42:193. [PubMed: 10398966]
14. Gallez B, Jordan BF, Baudelet C, Misson PD. Magn Reson Med 1999;42:627. [PubMed: 10502749]
15. O'Hara JA, Goda F, Demidenko E, Swartz HM. Radiat Res 1998;150:549. [PubMed: 9806597]
16. Ilangovan G, Liebgott T, Kutala VK, Petryakov S, Zweier JL, Kuppusamy P. Magn Reson Med 2004;51:835. [PubMed: 15065258]
17. Severinghaus, JW. The History of Anesthesia: Proceedings of the Fifth International Symposium on the History of Anesthesia; Santiago, Spain. 2001. p. 115
18. Cater DB, Silver IA. Acta Radiol 1960;53:233. [PubMed: 13808406]
19. Kolstad P. Scand J Clin Lab Invest Suppl 1968;106:145. [PubMed: 5731701]
20. Hockel M, Schlenger K, Knoop C, Vaupel P. Cancer Res 1991;51:6098. [PubMed: 1933873]
21. Brizel DM, Scully SP, Harrelson JM, Layfield LJ, Dodge RK, Charles HC, Samulski TV, Prosnitz LR, Dewhirst MW. Cancer Res 1996;56:5347. [PubMed: 8968082]
22. Dewhirst MW, Ong ET, Madwed D, Klitzman B, Secomb T, Brizel D, Bonaventura J, Rosner G, Kavanagh B, Edwards J, Gross J. Radiat Res 1992;132:61. [PubMed: 1410275]
23. Clark LC. Trans Am Soc Artif Internal Organs 1956;2:41.
24. Whalen WJ, Riley J, Nair P. J Appl Physiol 1967;23:798. [PubMed: 6061398]
25. Tsai AG, Friesenecker B, Mazzoni MC, Kerger H, Buerk DG, Johnson PC, Intaglietta M. Proc Natl Acad Sci USA 1998;95:6590. [PubMed: 9618456]
26. Baudelet C, Gallez B. Magn Reson Imaging 2004;22:905. [PubMed: 15288130]

27. Brizel DM, Scully SP, Harrelson JM, Layfield LJ, Bean JM, Prosnitz LR, Dewhirst MW. Cancer Res 1996;56:941. [PubMed: 8640781]
28. Okunieff P, Ding I, Vaupel P, Hockel M. Adv Exp Med Biol 2003;510:69. [PubMed: 12580407]
29. Vaupel P, Schlenger K, Knoop C, Hockel M. Cancer Res 1991;51:3316. [PubMed: 2040005]
30. O'Hara JA, Khan N, Hou H, Wilmo CM, Demidenko E, Dunn JF, Swartz HM. Physiol Meas 2004;25:1413. [PubMed: 15712720]
31. Huch A, Huch R, Arner B, Rooth G. Scand J Clin Lab Invest Suppl 1973;31:269.
32. Rooth G. Pediatrics 1975;55:232. [PubMed: 1090895]
33. Yu M, Morita SY, Daniel SR, Chapital A, Waxman K, Severino R. Shock 2006;26:450. [PubMed: 17047514]
34. Amann B, Luedemann C, Ratei R, Schmidt-Lucke JA. Cell Transplant 2009;18:371. [PubMed: 19500466]
35. Hodgkiss RJ. Anticancer Drug Des 1998;13:687. [PubMed: 9755725]
36. Koch CJ, Evans SM. Adv Exp Med Biol 2003;510:285. [PubMed: 12580442]
37. Kennedy AS, Raleigh JA, Perez GM, Calkins DP, Thrall DE, Novotny DB, Varia MA. Int J Radiat Oncol Biol Phys 1997;37:897. [PubMed: 9128967]
38. Griffiths JR, Robinson SP. Br J Radiol 1999;72:627. [PubMed: 10624317]
39. Wen B, Urano M, O'Donoghue JA, Ling CC. Radiat Res 2006;166:512. [PubMed: 16953670]
40. Nwaigwe CI, Roche MA, Grinberg O, Dunn JF. Adv Exp Med Biol 2003;530:101. [PubMed: 14562708]
41. O'Hara JA, Hou H, Demidenko E, Springett RJ, Khan N, Swartz HM. Physiol Meas 2005;26:203. [PubMed: 15798296]
42. Jordan BF, Cron GO, Gallez B. Magn Reson Med 2009;61:634. [PubMed: 19097235]
43. Pawlowski M, Wilson DF. Adv Exp Med Biol 1992;316:179. [PubMed: 1288078]
44. Rumsey WL, Vanderkooi JM, Wilson DF. Science 1988;241:1649. [PubMed: 3420417]
45. Shibata M, Ichioka S, Ando J, Kamiya A. J Appl Physiol 2001;91:321. [PubMed: 11408447]
46. Vinogradov SA, Lo LW, Jenkins WT, Evans SM, Koch C, Wilson DF. Biophys J 1996;70:1609. [PubMed: 8785320]
47. Tsukada K, Sakai S, Hase K, Minamitani H. Biosens Bioelectron 2003;18:1439. [PubMed: 12941558]
48. Wilson DF, Vinogradov SA, Grosul P, Vaccarezza MN, Kuroki A, Bennett J. Appl Opt 2005;44:5239. [PubMed: 16149347]
49. DeCampli WM, Schears G, Myung R, Schultz S, Creed J, Pastuszko A, Wilson DF. J Thorac Cardiovasc Surg 2003;125:472. [PubMed: 12658188]
50. Lo LW, Jenkins WT, Vinogradov SA, Evans SM, Wilson DF. Adv Exp Med Biol 1997;411:577. [PubMed: 9269475]
51. Wilson DF, Cerniglia GJ. Adv Exp Med Biol 1994;345:539. [PubMed: 8079756]
52. Severinghaus JW. J Clin Monit 1986;2:270. [PubMed: 3537215]
53. Walters TP. Br J Nurs 2007;16:1332. [PubMed: 18073672]
54. Cohn SM. J Am Coll Surg 2007;205:322. [PubMed: 17660081]
55. Quaresima V, Ferrari M. J Appl Physiol 2009;107:371. [PubMed: 19567814]
56. Thomson, SJ.; Cowan, ML.; Forton, DM.; Clark, SJ.; Musa, S.; Grounds, M.; Rahman, TM. Liver Int. 2009.
57. Carandang R, Krieger DW. Neurocrit Care 2007;6:161. [PubMed: 17572858]
58. De Blasi RA, Fantini S, Franceschini MA, Ferrari M, Gratton E. Med Biol Eng Comput 1995;33:228. [PubMed: 7643667]
59. Gora F, Shinde S, Elwell CE, Goldstone JC, Cope M, Delpy DT, Smith M. J Neurosurg Anesthesiol 2002;14:218. [PubMed: 12172295]
60. Tamura M, Hazeki O, Nioka S, Chance B. Annu Rev Physiol 1989;51:813. [PubMed: 2653207]
61. Vo-Dinh T, Stokes DL, Wabuyele MB, Martin ME, Song JM, Jagannathan R, Michaud E, Lee RJ, Pan X. IEEE Eng Med Biol Mag 2004;23:40. [PubMed: 15565798]
62. Khoobehi B, Beach JM, Kawano H. Invest Ophthalmol Vis Sci 2004;45:1464. [PubMed: 15111603]

63. Sorg BS, Moeller BJ, Donovan O, Cao Y, Dewhirst MW. J Biomed Opt 2005;10:44004. [PubMed: 16178638]
64. Zuzak KJ, Schaeberle MD, Gladwin MT, Cannon RO 3rd, Levin IW. Circulation 2001;104:2905. [PubMed: 11739304]
65. Shah SA, Bachrach N, Spear SJ, Letbetter DS, Stone RA, Dhir R, Prichard JW, Brown HG, LaFramboise WA. Biotechniques 2003;34:408. [PubMed: 12613264]
66. Cancio LC, Batchinsky AI, Mansfield JR, Panasyuk S, Hetz K, Martini D, Jordan BS, Tracey B, Freeman JE. J Trauma 2006;60:1087. [PubMed: 16688075]
67. Aboagye EO, Kelson AB, Tracy M, Workman P. Anticancer Drug Des 1998;13:703. [PubMed: 9755726]
68. Read SJ, Hirano T, Abbott DF, Sachinidis JI, Tochon-Danguy HJ, Chan JG, Egan GF, Scott AM, Bladin CF, McKay WJ, Donnan GA. Neurology 1998;51:1617. [PubMed: 9855512]
69. Dolbier WR Jr, Li AR, Koch CJ, Shiue CY, Kachur AV. Appl Radiat Isot 2001;54:73. [PubMed: 11144255]
70. Chapman JD, Engelhardt EL, Stobbe CC, Schneider RF, Hanks GE. Radiother Oncol 1998;46:229. [PubMed: 9572615]
71. Lehtio K, Oikonen V, Gronroos T, Eskola O, Kalliokoski K, Bergman J, Solin O, Grenman R, Nuutila P, Minn H. J Nucl Med 2001;42:1643. [PubMed: 11696633]
72. Koh WJ, Bergman KS, Rasey JS, Peterson LM, Evans ML, Graham MM, Grierson JR, Lindsley KL, Lewellen TK, Krohn KA, Griffin TW. Int J Radiat Oncol Biol Phys 1995;33:391. [PubMed: 7673026]
73. Busse LJ, Thomas SR, Pratt RG, Clark LC Jr, Ackerman JL, Samaratunga RC, Hoffmann RE. Med Phys 1986;13:518. [PubMed: 3736510]
74. Clark LC Jr, Ackerman JL, Thomas SR, Millard RW, Hoffman RE, Pratt RG, Ragle-Cole H, Kinsey RA, Janakiraman R. Adv Exp Med Biol 1984;180:835. [PubMed: 6534151]
75. Mason RP, Rodbumrung W, Antich PP. NMR Biomed 1996;9:125. [PubMed: 8892399]
76. Sotak CH, Hees PS, Huang HN, Hung MH, Krespan CG, Raynolds S. Magn Reson Med 1993;29:188. [PubMed: 8429782]
77. Bartusik D, Tomanek B, Siluk D, Kaliszan R, Fallone G. Anal Biochem 2009;387:315. [PubMed: 19454246]
78. McNab JA, Yung AC, Kozlowski P. Magma 2004;17:288. [PubMed: 15605277]
79. Duong TQ, Kim SG. Magn Reson Med 2000;43:393. [PubMed: 10725882]
80. Jacob RE, Chang YV, Choong CK, Bierhals A, Zheng Hu D, Zheng J, Yablonskiy DA, Woods JC, Gierada DS, Conradi MS. Magn Reson Med 2005;54:577. [PubMed: 16086368]
81. Ito Y, Berkowitz BA. Vision Res 2001;41:1307. [PubMed: 11322975]
82. Yu JX, Kodibagkar VD, Cui W, Mason RP. Curr Med Chem 2005;12:819. [PubMed: 15853714]
83. Thulborn KR, Waterton JC, Matthews PM, Radda GK. Biochim Biophys Acta 1982;714:265. [PubMed: 6275909]
84. Ogawa S, Lee TM, Kay AR, Tank DW. Proc Natl Acad Sci USA 1990;87:9868. [PubMed: 2124706]
85. Di Salle F, Formisano E, Linden DE, Goebel R, Bonavita S, Pepino A, Smaltino F, Tedeschi G. Eur J Radiol 1999;30:84. [PubMed: 10401589]
86. Baudelet C, Gallez B. Magn Reson Med 2002;48:980. [PubMed: 12465107]
87. Backer JM, Budker VG, Eremenko SI, Molin YN. Biochim Biophys Acta 1977;460:152. [PubMed: 192284]
88. Gurbiel R, Cieszka K, Pajak S, Subczynski W, Lukiewicz S. Folia Histochem Cytochem (Krakow) 1980;18:87. [PubMed: 6256266]
89. Morse PD 2nd, Swartz HM. Magn Reson Med 1985;2:114. [PubMed: 3007919]
90. Kusumi A, Subczynski WK, Hyde JS. Proc Natl Acad Sci USA 1982;79:1854. [PubMed: 6952236]
91. Subczynski WK, Hyde JS. Biochim Biophys Acta 1981;643:283. [PubMed: 6261814]
92. Thomas DD, Wendt CH, Francisz W, Hyde JS. Biophys J 1983;43:131. [PubMed: 6309262]
93. Subczynski WK, Lukiewicz S, Hyde JS. Magn Reson Med 1986;3:747. [PubMed: 3023786]
94. Swartz HM, Clarkson RB. Phys Med Biol 1998;43:1957. [PubMed: 9703059]

95. Khan N, Hou H, Hein P, Comi RJ, Buckey JC, Grinberg O, Salikhov I, Lu SY, Wallach H, Swartz HM. Adv Exp Med Biol 2005;566:119. [PubMed: 16594143]
96. He J, Beghein N, Clarkson RB, Swartz HM, Gallez B. Phys Med Biol 2001;46:3323. [PubMed: 11768508]
97. Kessel AR, Salimov VG. Russian Phys J 317–322;14:317.
98. Teng CL, Hong H, Kiihne S, Bryant RG. J Magn Reson 2001;148:31. [PubMed: 11133273]
99. Eastman MP, Kooser RG, Das MR, Freed JH. J Chem Phys 1969;51:2690.
100. Gorter CJ, Van Vleck JH. Phys Rev 1947;72:1128.
101. Anderson PW, Weiss PR. Rev Mod Phys 1953;25:269.
102. Grinberg OY, Williams BB, Ruuge AE, Grinberg SA, Wilcox DE, Swartz HM, Freed JH. J Phys Chem B 2007;111:13316. [PubMed: 17973414]
103. Murugesan R, Cook JA, Devasahayam N, Afeworki M, Subramanian S, Tschudin R, Larsen JA, Mitchell JB, Russo A, Krishna MC. Magn Reson Med 1997;38:409. [PubMed: 9339442]
104. Ernst RR, Anderson WA. Rev Sci Instrum 1966;37:93.
105. Quine RW, ARG, Eaton SS, Eaton GR. Concepts Magn Reson 2002;15:59.
106. Subramanian S, Matsumoto K, Mitchell JB, Krishna MC. NMR Biomed 2004;17:263. [PubMed: 15366027]
107. Oikawa K, Ogata T, Togashi H, Lin Y, Sato T. Anal Sci 1995;11:885.
108. He G, Shankar RA, Chzhan M, Samouilov A, Kuppusamy P, Zweier JL. Proc Natl Acad Sci USA 1999;96:4586. [PubMed: 10200306]
109. Rupp LW, Wittig KR, Wash MW. Am J Phys 1976;44:655.
110. Kuppusamy P, Chzhan M, Vij K, Shteynbuk M, Lefer DJ, Giannella E, Zweier JL. Proc Natl Acad Sci USA 1994;91:3388. [PubMed: 8159757]
111. Thomas, SR.; Busse, LJ.; Scheuck, VF. AAPM 1985 Summer School in Medical Physics; Seattle, WA. 1985.
112. Golay MJ. Rev Sci Instrum 1958;29:313.
113. Chzhan M, Kuppusamy P, Zweier JL. J Magn Reson, Ser B 1995;108:67. [PubMed: 7627435]
114. He G, Petryakov S, Samouilov A, Chzhan M, Kuppusamy P, Zweier JL. J Magn Reson 2001;149:218. [PubMed: 11318620]
115. Froncisz W, Hyde JS. J Magn Reson 1982;47:515.
116. Sotgiu A. J Magn Reson 1985;65:206.
117. Bacic G, Nilges MJ, Magin RL, Walczak T, Swartz HM. Magn Reson Med 1989;10:266. [PubMed: 2761384]
118. Chzhan M, Shtenbuk M, Kuppusamy P, Zweier JL. J Magn Reson, Ser A 1993:105.
119. Poole, CPJ. Electron Spin Resonance: A Comprehensive Treatise on Experimental Techniques. 2. Dover Publications; Mineola: 1997.
120. Stoner JW, Szymanski D, Eaton SS, Quine RW, Rinard GA, Eaton GR. J Magn Reson 2004;170:127. [PubMed: 15324766]
121. Robinson BH, Mailer C, Reese AW. J Magn Reson 1999;138:199. [PubMed: 10341123]
122. Bales BL, Peric M, Lamy-Freund MT. J Magn Reson 1998;132:279. [PubMed: 9632554]
123. Williams BB, Pan X, Halpern HJ. J Magn Reson 2005;174:88. [PubMed: 15809176]
124. Alecci M, Colacicchi S, Indovina PL, Momo F, Pavone P, Sotgiu A. J Magn Reson Imaging 1990;8:59.
125. Kuppusamy P, Wang P, Zweier JL. Magn Reson Med 1995;34:99. [PubMed: 7674904]
126. Deans, SR. The Radon Transform and Some of its Applications. John Wiley & Sons; New York: 1983.
127. Herman GT, Lent A. Comput Biol Med 1976;6:273. [PubMed: 1000955]
128. Wang CX, Snydera WE, Bilbro G, Santago P. Comput Biol Med 1998;28:13. [PubMed: 9644571]
129. Press, WH.; Flannery, BP.; Teukolsky, SA.; Vetterling, WT. Numerical Recipes in FORTRAN: The Art of Scientific Computing. Cambridge University Press; Cambridge: 1992.
130. Maltempo MM. J Magn Reson 1986;69:156.

131. Hanson KM. J Op Soc Am 1983;73:1501.
132. Epel B, Sundramoorthy SV, Mailer C, Halpern HJ. Concepts Magn Reson 2008;33B:163.
133. Mailer C, Robinson BH, Williams BB, Halpern HJ. Magn Reson Med 2003;49:1175. [PubMed: 12768596]
134. Williams BB, Hou H, Grinberg OY, Demidenko E, Swartz HM. Antioxid Redox Signal 2007;9:1691. [PubMed: 17678442]
135. Dadok J, Sprecher RF. J Magn Reson 1974;13:243.
136. Joshi JP, Ballard JR, Rinard GA, Quine RW, Eaton SS, Eaton GR. J Magn Reson 2005;175:44. [PubMed: 15949747]
137. Lewitt RM. IEEE Proc 1983;71:390.
138. Kak, AC.; Slaney, M. IEEE Press. New York: 1988.
139. Delaney AH, Bresler Y. IEEE Trans Image Process 1996;5:740. [PubMed: 18285163]
140. Ahmad R, Clymer B, Vikram DS, Deng Y, Hirata H, Zweier JL, Kuppusamy P. J Magn Reson 2007;184:246. [PubMed: 17113800]
141. Tseitlin M, Dhami A, Eaton SS, Eaton GR. J Magn Reson 2007;184:157. [PubMed: 17070083]
142. Subramanian S, Devasahayam N, Murugesan R, Yamada K, Cook J, Taube A, Mitchell JB, Lohman JA, Krishna MC. Magn Reson Med 2002;48:370. [PubMed: 12210946]
143. Deng Y, Petryakov S, He G, Kesselring E, Kuppusamy P, Zweier JL. J Magn Reson 2007;185:283. [PubMed: 17267252]
144. Grinberg OY, Smirnov AI, Swartz HM. J Magn Reson 2001;152:247. [PubMed: 11567578]
145. Som S, Potter LC, Ahmad R, Vikram DS, Kuppusamy P. J Magn Reson 2008;193:210. [PubMed: 18538600]
146. Hyde JS, Mchaourab HS, Camenisch T, Ratke JJ, Cox RW, Froncisz W. Rev Sci Instrum 1998;69:2622.
147. Hyde, JS.; Camenisch, TG.; Ratke, JJ.; Strangeway, RA.; Froncisz, W. Biomedical EPR, Part B: Methodology, Instrumentation, and Dynamics. Eaton, SR.; Eaton, GR.; Berliner, LJ., editors. Kluwer Academic/Plenum Publishers; New York: 2005.
148. Lurie DJ, Bussell DM, Bell LH, Mallard JR. J Magn Reson 1988;76:366.
149. Overhauser AW. Phys Rev 1953;92:411.
150. Krishna MC, English S, Yamada K, Yoo J, Murugesan R, Devasahayam N, Cook JA, Golman K, Ardenkjaer-Larsen JH, Subramanian S, Mitchell JB. Proc Natl Acad Sci USA 2002;99:2216. [PubMed: 11854518]
151. Matsumoto S, Yamada K, Hirata H, Yasukawa K, Hyodo F, Ichikawa K, Utsumi H. Magn Reson Med 2007;57:806. [PubMed: 17390363]
152. Popp CA, Hyde JS. J Magn Reson 1981;43:249.
153. Gallez B, Bacic G, Goda F, Jiang J, O'Hara JA, Dunn JF, Swartz HM. Magn Reson Med 1996;35:97. [PubMed: 8771027]
154. Liu S, Timmins GS, Shi H, Gasparovic CM, Liu KJ. NMR Biomed 2004;17:327. [PubMed: 15366032]
155. Smirnov AI, Clarkson RB, Belford RL. J Magn Reson, Ser B 1996;111:149. [PubMed: 8661272]
156. Liu KJ, Gast P, Moussavi M, Norby SW, Vahidi N, Walczak T, Wu M, Swartz HM. Proc Natl Acad Sci USA 1993;90:5438. [PubMed: 8390665]
157. Ilangovan G, Zweier JL, Kuppusamy P. J Phys Chem B 2000;104:9404.
158. Pandian RP, Dolgos M, Dang V, Sostaric JZ, Woodward PM, Kuppusamy P. Chem Mater 2007;19:3545.
159. Manivannan A, Yanagi H, Ilangovan G, Kuppusamy P. J Magn Magn Mater 2001;233:L131.
160. Pandian RP, Parinandi NL, Ilangovan G, Zweier JL, Kuppusamy P. Free Radical Biol Med 2003;35:1138. [PubMed: 14572616]
161. Vahidi N, Clarkson RB, Liu KJ, Norby SW, Wu M, Swartz HM. Magn Reson Med 1994;31:139. [PubMed: 8133749]
162. Smirnova TI, Smirnov AI, Clarkson RB, Belford RL. J Phys Chem 1994;98:2464.

163. James PE, Grinberg OY, Goda F, Panz T, O'Hara JA, Swartz HM. Magn Reson Med 1997;38:48. [PubMed: 9211379]
164. Goda F, Liu KJ, Walczak T, O'Hara JA, Jiang J, Swartz HM. Magn Reson Med 1995;33:237. [PubMed: 7707915]
165. Shen J, Bottle S, Khan N, Grinberg O, Reid D, Micallef A, Swartz H. Appl Magn Reson 2002;22:357.
166. Dhimitruka I, Velayutham M, Bobko AA, Khramtsov VV, Villamena FA, Hadad CM, Zweier JL. Bioorg Med Chem Lett 2007;17:6801. [PubMed: 17964156]
167. Philipp R, McIntyre JO, Robinson BH, Huth H, Trommer W, Fleischer S. Biochim Biophys Acta 1984;790:251. [PubMed: 6091764]
168. Liu KJ, Grinstaff MW, Jiang J, Suslick KS, Swartz HM, Wang W. Biophys J 1994;67:896. [PubMed: 7948703]
169. Glockner JF, Norby SW, Swartz HM. Magn Reson Med 1993;29:12. [PubMed: 8380480]
170. Halpern HJ, Peric M, Nguyen TD, Spencer DP, Teicher BA, Lin YJ, Bowman MK. J Magn Reson 1990;90:40.
171. Alecci M, Ferrari M, Quaresima V, Sotgiu A, Ursini CL. Biophys J 1994;67:1274. [PubMed: 7811942]
172. Ardenkjaer-Larsen JH, Laursen I, Leunbach I, Ehnholm G, Wistrand LG, Petersson JS, Golman K. J Magn Reson 1998;133:1. [PubMed: 9654463]
173. Elas M, Ahn KH, Parasca A, Barth ED, Lee D, Haney C, Halpern HJ. Clin Cancer Res 2006;12:4209. [PubMed: 16857793]
174. Kutala VK, Parinandi NL, Pandian RP, Kuppusamy P. Antioxid Redox Signal 2004;6:597. [PubMed: 15130286]
175. Subramanian S, Yamada K, Irie A, Murugesan R, Cook JA, Devasahayam N, Van Dam GM, Mitchell JB, Krishna MC. Magn Reson Med 2002;47:1001. [PubMed: 11979580]
176. Driesschaert B, Charlier N, Gallez B, Marchand-Brynaert J. Bioorg Med Chem Lett 2008;18:4291. [PubMed: 18640034]
177. Bobko AA, Dhimitruka I, Eubank TD, Marsh CB, Zweier JL, Khramtsov VV. Free Radical Biol Med 2009;47:654. [PubMed: 19523513]
178. Liu Y, Villamena FA, Sun J, Xu Y, Dhimitruka I, Zweier JL. J Org Chem 2008;73:1490. [PubMed: 18201099]
179. Dang V, Wang J, Feng S, Buron C, Villamena FA, Wang PG, Kuppusamy P. Bioorg Med Chem Lett 2007;17:4062. [PubMed: 17499990]
180. Bratasz A, Kulkarni AC, Kuppusamy P. Biophys J 2007;92:2918. [PubMed: 17259268]
181. Swartz HM, Boyer S, Gast P, Glockner JF, Hu H, Liu KJ, Moussavi M, Norby SW, Vahidi N, Walczak T, Wu M, Clarkson RB. Magn Reson Med 1991;20:333. [PubMed: 1663568]
182. Zweier JL, Chzhan M, Ewert U, Schneider G, Kuppusamy P. J Magn Reson, Ser B 1994;105:52. [PubMed: 7921671]
183. Smirnov AI, Norby SW, Clarkson RB, Walczak T, Swartz HM. Magn Reson Med 1993;30:213. [PubMed: 8396190]
184. Swartz HM, Liu KJ, Goda F, Walczak T. Magn Reson Med 1994;31:229. [PubMed: 8133760]
185. Afeworki M, Miller NR, Devasahayam N, Cook J, Mitchell JB, Subramanian S, Krishna MC. Free Radical Biol Med 1998;25:72. [PubMed: 9655524]
186. Ilangovan G, Zweier JL, Kuppusamy P. J Phys Chem B 2000;104:4047.
187. Turek P, Andre JJ, Giraudeau A, Simon J. Chem Phys Lett 1986:134.
188. Ilangovan G, Li H, Zweier JL, Kuppusamy P. J Phys Chem B 2001;105:5323.
189. Ilangovan G, Manivannan A, Li H, Yanagi H, Zweier JL, Kuppusamy P. Free Radical Biol Med 2002;32:139. [PubMed: 11796202]
190. Pandian RP, Dolgos M, Marginean C, Woodward PM, Hammel PC, Manoharan PT, Kuppusamy P. J Mater Chem 2009;19:4138. [PubMed: 19809598]
191. Pandian RP, Kim YI, Woodward PM, Zweier JL, Manoharan PT, Kuppusamy P. J Mater Chem 2006;16:3609.
192. Dinguizli M, Beghein N, Gallez B. Physiol Meas 2008;29:1247. [PubMed: 18843166]

193. Eteshola E, Pandian RP, Lee SC, Kuppusamy P. Biomed Microdevices 2009;11:379. [PubMed: 19083100]
194. Gallez B, Debuyst R, Liu KJ, Demeure R, Dejehet F, Swartz HM. Magma 1996;4:71. [PubMed: 8774004]
195. He J, Beghein N, Ceroke P, Clarkson RB, Swartz HM, Gallez B. Magn Reson Med 2001;46:610. [PubMed: 11550256]
196. Meenakshisundaram G, Eteshola E, Pandian RP, Bratasz A, Lee SC, Kuppusamy P. Biomed Microdevices 2009;11:773. [PubMed: 19291409]
197. Belanger MC, Marois Y. J Biomed Mater Res 2001;58:467. [PubMed: 11505420]
198. Pajak, S.; Cieszka, K.; Gurbiel, R.; Subczynski, WK.; Lukiewicz, SJ. Third meeting of the Polish Biophysical Society; Wroclaw-Olesnicka. 1978. p. 70
199. Sarna T, Duleba A, Korytowski W, Swartz HM. Arch Biochem Biophys 1980;200:140. [PubMed: 6244787]
200. Shen J, Khan N, Lewis LD, Armand R, Grinberg O, Demidenko E, Swartz H. Biophys J 2003;84:1291. [PubMed: 12547809]
201. Ashikawa I, Yin JJ, Subczynski WK, Kouyama T, Hyde JS, Kusumi A. Biochemistry 1994;33:4947. [PubMed: 8161556]
202. Subczynski WK, Wisniewska A, Yin JJ, Hyde JS, Kusumi A. Biochemistry 1994;33:7670. [PubMed: 8011634]
203. Subczynski WK, Markowska E, Sielewiesiuk J. Biochim Biophys Acta 1991;1068:68. [PubMed: 1654104]
204. Subczynski WK, Lewis RN, McElhaney RN, Hodges RS, Hyde JS, Kusumi A. Biochemistry 1998;37:3156. [PubMed: 9485469]
205. Hockel M, Schlenger K, Mitze M, Schaffer U, Vaupel P. Semin Radiat Oncol 1996;6:3. [PubMed: 10717157]
206. Rofstad EK. Int J Radiat Biol 2000;76:589. [PubMed: 10866281]
207. Selvendiran K, Bratasz A, Kuppusamy ML, Tazi MF, Rivera BK, Kuppusamy P. Int J Cancer 2009;125:2198. [PubMed: 19623660]
208. Menon C, Fraker DL. Cancer Lett 2005;221:225. [PubMed: 15808408]
209. Evans SM, Du KL, Chalian AA, Mick R, Zhang PJ, Hahn SM, Quon H, Lustig R, Weinstein GS, Koch CJ. Int J Radiat Oncol Biol Phys 2007;69:1024. [PubMed: 17967299]
210. Halpern HJ, Yu C, Peric M, Barth E, Grdina DJ, Teicher BA. Proc Natl Acad Sci USA 1994;91:13047. [PubMed: 7809170]
211. Halpern HJ, Yu C, Peric M, Barth ED, Karczmar GS, River JN, Grdina DJ, Teicher BA. Radiat Res 1996;145:610. [PubMed: 8619027]
212. Ilangovan G, Bratasz A, Li H, Schmalbrock P, Zweier JL, Kuppusamy P. Magn Reson Med 2004;52:650. [PubMed: 15334586]
213. Bratasz A, Pandian RP, Deng Y, Petryakov S, Grecula JC, Gupta N, Kuppusamy P. Magn Reson Med 2007;57:950. [PubMed: 17457861]
214. Hou H, Lariviere JP, Demidenko E, Gladstone D, Swartz H, Khan N. Radiother Oncol 2009;91:126. [PubMed: 19013657]
215. Eubank TD, Roberts RD, Khan M, Curry JM, Nuovo GJ, Kuppusamy P, Marsh CB. Cancer Res 2009;69:2133. [PubMed: 19223554]
216. Gallez B, Debuyst R, Dejehet F, Liu KJ, Walczak T, Goda F, Demeure R, Taper H, Swartz HM. Magn Reson Med 1998;40:152. [PubMed: 9660565]
217. Meenakshisundaram G, Eteshola E, Pandian RP, Bratasz A, Selvendiran K, Lee SC, Krishna MC, Swartz HM, Kuppusamy P. Biomed Microdevices 2009;11:817. [PubMed: 19319683]
218. Gallez B, Baudelet C, Jordan BF. NMR Biomed 2004;17:240. [PubMed: 15366026]
219. Friedman BJ, Grinberg OY, Isaacs KA, Walczak TM, Swartz HM. J Mol Cell Cardiol 1995;27:2551. [PubMed: 8825876]
220. Zweier JL, Kuppusamy P. Proc Natl Acad Sci USA 1988;85:5703. [PubMed: 2840672]

221. Zweier JL, Thompson-Gorman S, Kuppusamy P. J Bioenerg Biomembr 1991;23:855. [PubMed: 1663949]

222. Grinberg OY, Grinberg SA, Friedman BJ, Swartz HM. Adv Exp Med Biol 1997;411:171. [PubMed: 9269425]

223. Angelos MG, Kutala VK, Torres CA, He G, Stoner JD, Mohammad M, Kuppusamy P. Am J Physiol Heart Circ Physiol 2006;290:H341. [PubMed: 16126819]

224. Zhu X, Zuo L, Cardounel AJ, Zweier JL, He G. Antioxid Redox Signal 2007;9:447. [PubMed: 17280486]

225. Khan M, Mohan IK, Kutala VK, Kotha SR, Parinandi NL, Hamlin RL, Kuppusamy P. Antioxid Redox Signal 2009;11:725. [PubMed: 18855521]

226. Khan M, Kutala VK, Wisel S, Chacko SM, Kuppusamy ML, Kwiatkowski P, Kuppusamy P. Adv Exp Med Biol 2008;614:45. [PubMed: 18290313]

227. Khan M, Kutala VK, Vikram DS, Wisel S, Chacko SM, Kuppusamy ML, Mohan IK, Zweier JL, Kwiatkowski P, Kuppusamy P. Am J Physiol Heart Circ Physiol 2007;293:H2129. [PubMed: 17660391]

228. Chacko SM, Khan M, Kuppusamy ML, Pandian RP, Varadharaj S, Selvendiran K, Bratasz A, Rivera BK, Kuppusamy P. Am J Physiol Heart Circ Physiol 2009;296:H1263. [PubMed: 19286938]

229. Khan M, Meduru S, Mohan IK, Kuppusamy ML, Wisel S, Kulkarni A, Rivera BK, Hamlin RL, Kuppusamy P. J Mol Cell Cardiol 2009;47:275. [PubMed: 19376124]

230. Gordillo GM, Schlanger R, Wallace WA, Bergdall V, Bartlett R, Sen CK. Methods Enzymol 2004;381:575. [PubMed: 15063699]

231. Hopf HW, Gibson JJ, Angeles AP, Constant JS, Feng JJ, Rollins MD, Zamirul Hussain M, Hunt TK. Wound Repair Regen 2005;13:558. [PubMed: 16283871]

232. Mills C, Bryson P. Eur J Cardiothorac Surg 2006;30:153. [PubMed: 16769519]

233. Schugart RC, Friedman A, Zhao R, Sen CK. Proc Natl Acad Sci USA 2008;105:2628. [PubMed: 18272493]

234. Lu C, Rollins M, Hou H, Swartz HM, Hopf H, Miclau T, Marcucio RS. Iowa Orthop J 2008;28:14. [PubMed: 19223943]

235. James PE, Bacic G, Grinberg OY, Goda F, Dunn JF, Jackson SK, Swartz HM. Free Radical Biol Med 1996;21:25. [PubMed: 8791090]

236. Jiang J, Nakashima T, Liu KJ, Goda F, Shima T, Swartz HM. J Appl Physiol 1996;80:552. [PubMed: 8929598]

237. Glockner JF, Chan HC, Swartz HM. Magn Reson Med 1991;20:123. [PubMed: 1658535]

238. Hou H, Grinberg O, Williams B, Grinberg S, Yu H, Alvarenga DL, Wallach H, Buckey J, Swartz HM. Physiol Meas 2007;28:963. [PubMed: 17664686]

239. Liu KJ, Bacic G, Hoopes PJ, Jiang J, Du H, Ou LC, Dunn JF, Swartz HM. Brain Res 1995;685:91. [PubMed: 7583257]

Biographies

Rizwan Ahmad received the B.S. degree with honors in electrical engineering from The University of Engineering and Technology, Lahore, Pakistan in 2000, and the M.S. and Ph.D. degrees in electrical and computer engineering from The Ohio State University in 2004 and 2007, respectively. In his M.S., he worked as a research assistant on Electrical Capacitance Tomography with the Department Chemical Engineering. In his Ph.D., he worked as a research assistant on fast data collection and reconstruction methods for EPR imaging with the Davis Heart & Lung Research Institute (DHLRI). Since 2007, he has been with the DHLRI, Ohio State University Medical Center, Columbus, Ohio, where he is currently appointed as a Research Scientist. His research interests include biomedical signal processing, tomographic reconstruction, *in vivo* oximetry, and electron paramagnetic resonance spectroscopy and imaging.

Periannan Kuppusamy received his Ph.D. degree in 1986 with specialization in EPR (electron paramagnetic resonance) spectroscopy from the Indian Institute of Technology, Chennai, India. Following a brief Fogarty Fellowship program at the National Institutes of Health (NIH), Dr. Kuppusamy joined the Johns Hopkins University School of Medicine in 1987 as a Research Fellow and became a faculty in the cardiology division in 1991. In 2002, Dr. Kuppusamy moved to The Ohio State University, where he is currently a Professor in the Department of Internal Medicine. Dr. Kuppusamy functions as the Director of the Center for Biomedical Spectroscopy & Imaging; and Director of the Small Animal Imaging Center in the OSU College of Medicine. Dr. Kuppusamy has developed a variety of *in vivo* EPR spectroscopic and imaging

techniques for noninvasive measurements of free radicals and oxygen in biological systems. His major research focus is stem-cell therapy for myocardial infarction, novel bi-functional therapeutics for cardiovascular and cancer applications, and technology development for EPR-based oximetry for clinical applications. Dr. Kuppusamy has published over 280 peer-reviewed manuscripts of his research in leading scientific journals. He has several grants from the National Institutes of Health for the development of clinical oximetry and cardiovascular research. Dr. Kuppusamy has received research awards, including a Silver Medal in 2006 from the International EPR Society for significant contributions to the development of EPR imaging for biomedical applications; and a Doctorate of Medicine (*honoris causa*) in 2008 from the University of Pecs (Pecs, Hungary) for his cardiovascular research.

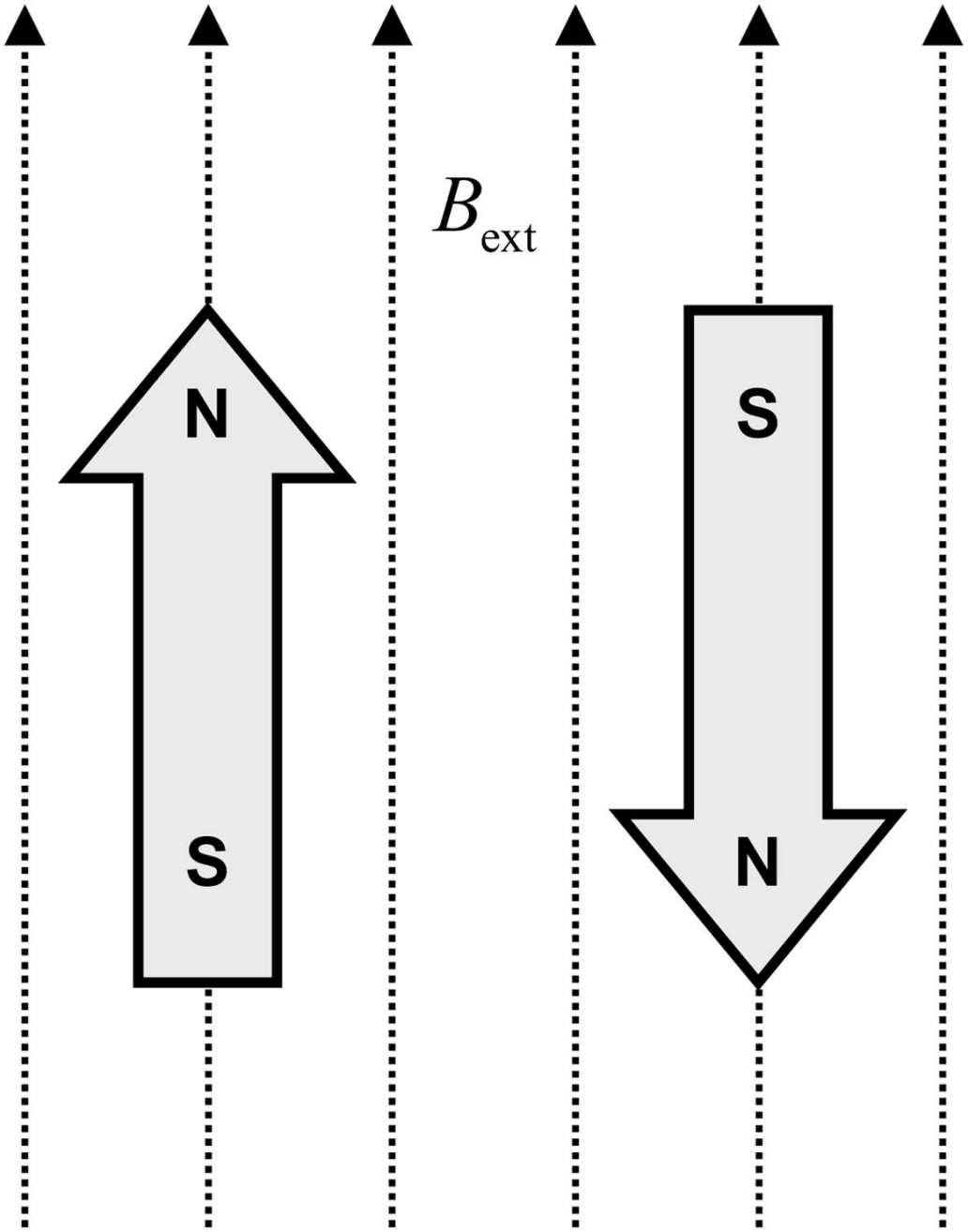

Figure 1.
Lowest (left) and highest (right) energy orientations of the magnetic moment of an unpaired electron in the presence of an external magnetic field B_{ext}.

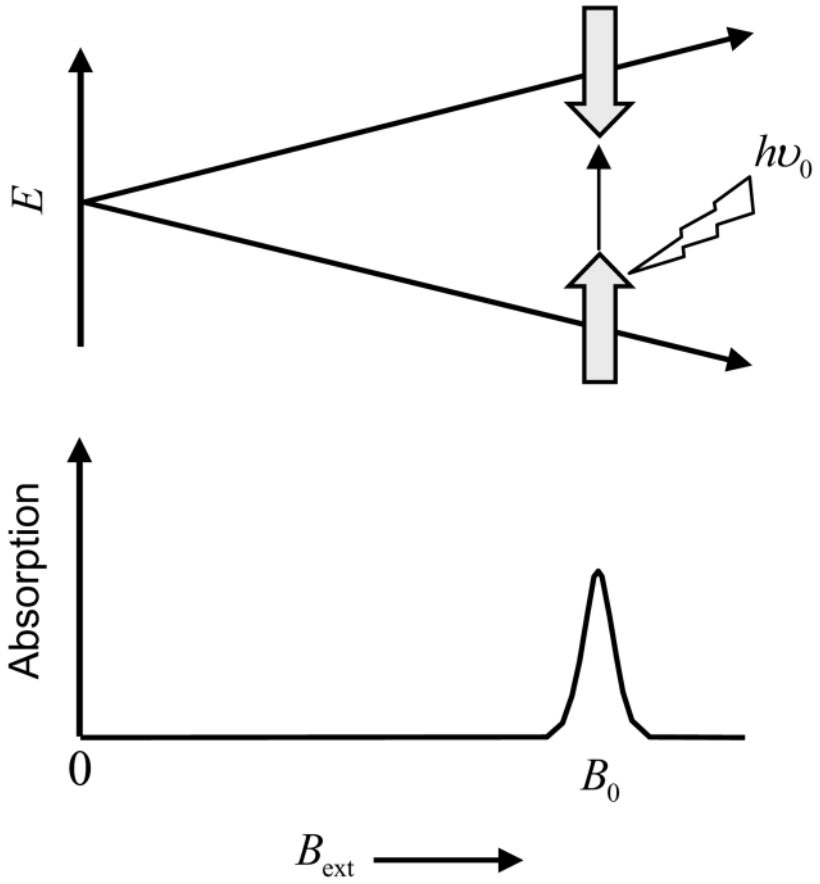

Figure 2.
Zeeman splitting in the presence of an external magnetic field B_{ext} (neglecting second order effects like hyperfine splitting).

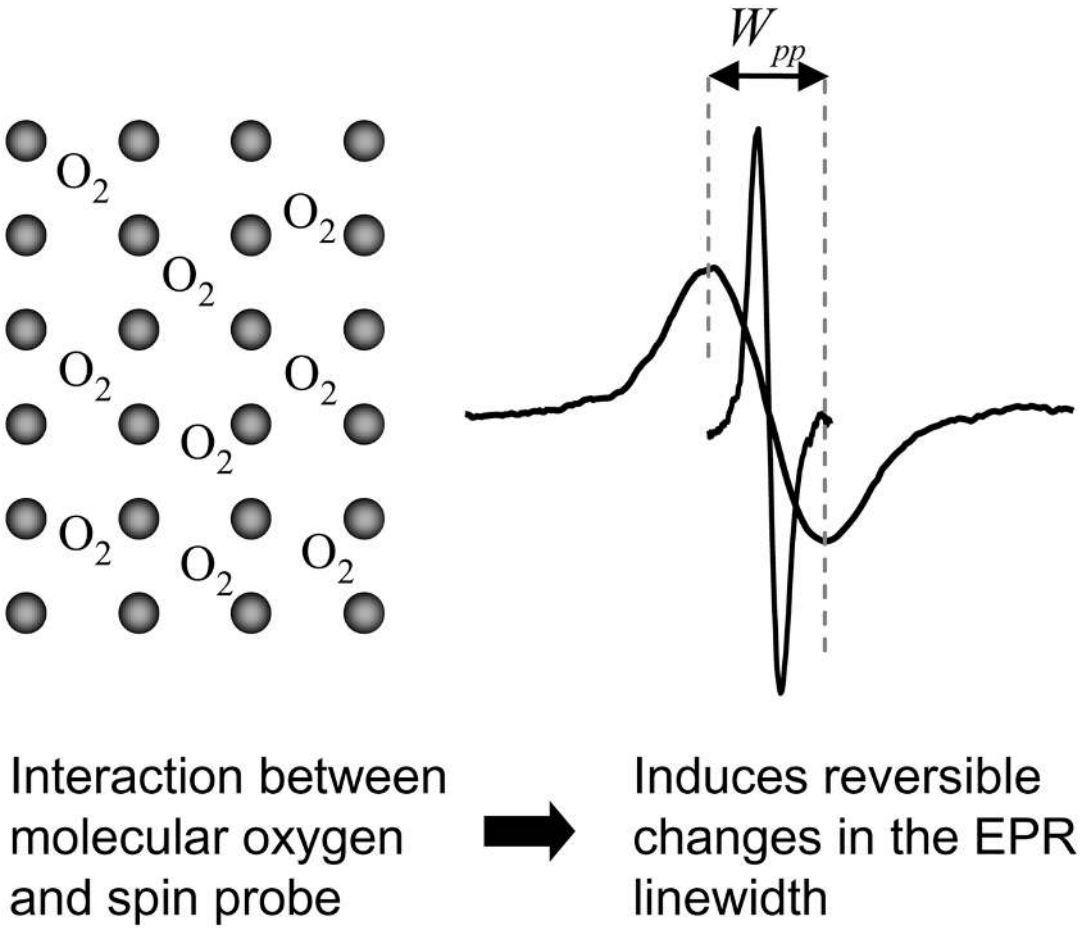

Figure 3.
Effect of oxygen on exchange narrowed lineshape. Black dots represents spin probe molecules. Introduction of O_2 induces line broadening measured by peak-to-peak linewidth W_{pp}.

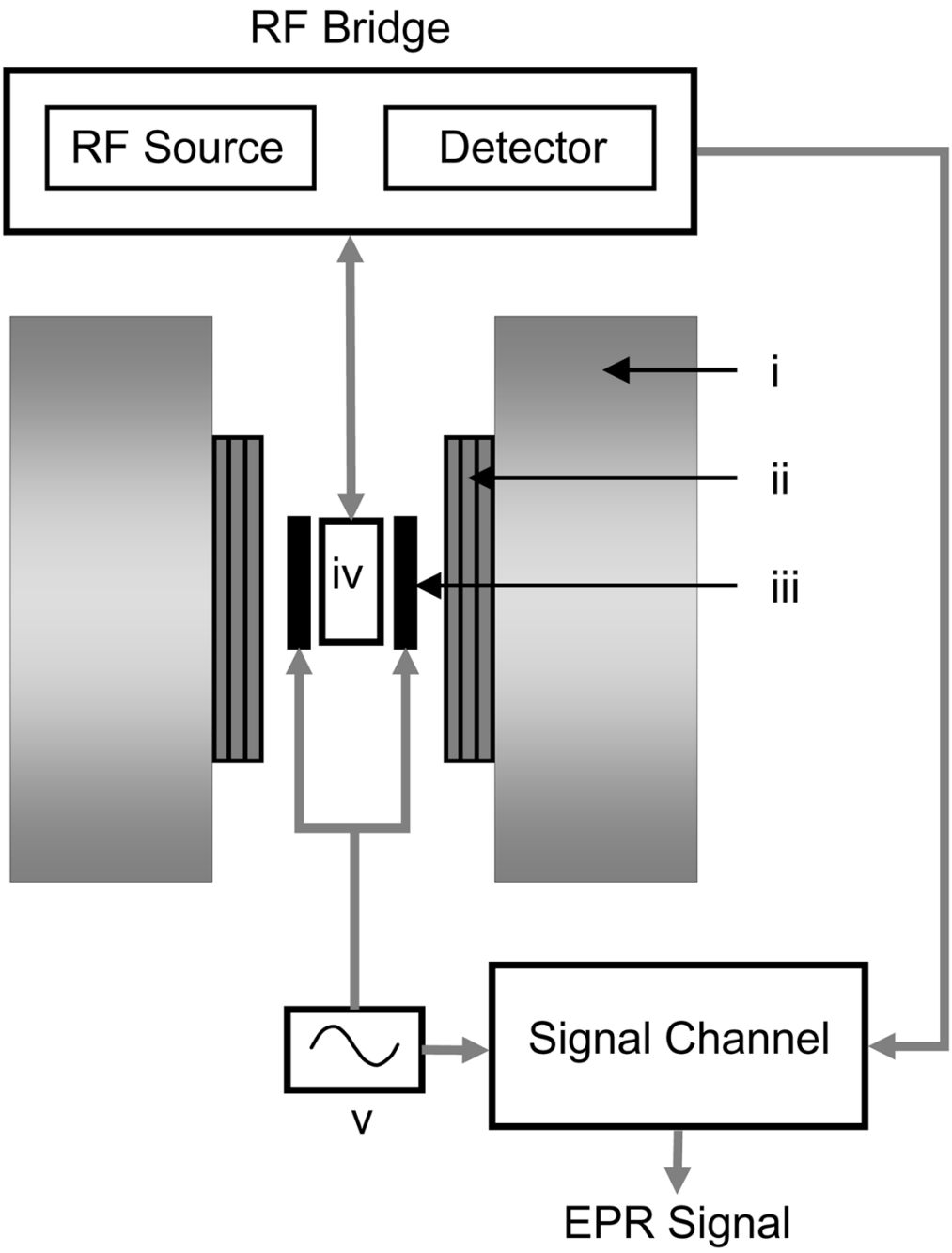

Figure 4.
A basic layout of a CW EPR spectrometer and imager. i, main magnet; ii, gradient coil assembly; iii, field modulation coil; iv, resonator; v, field modulation source.

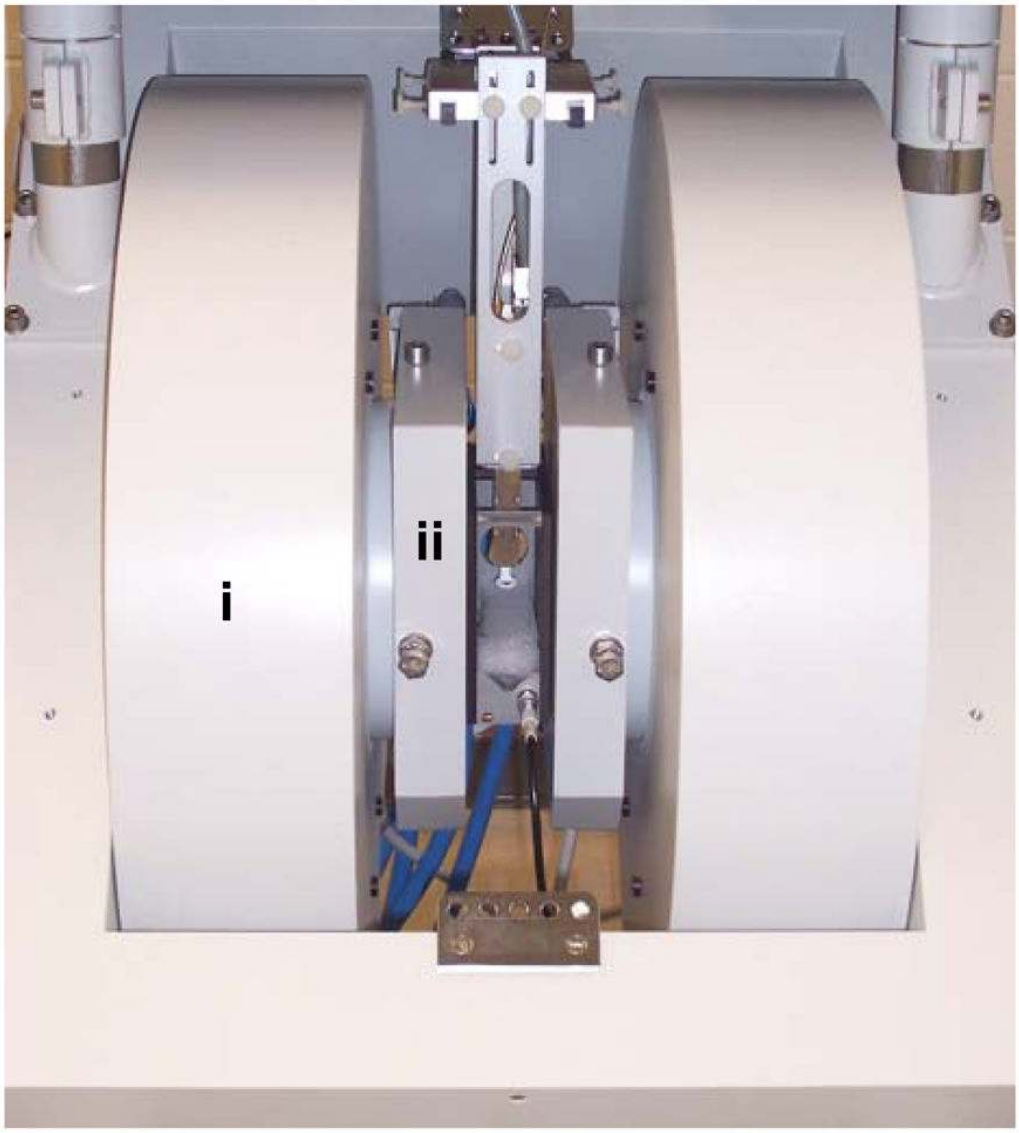

Figure 5.
Bruker (Bruker BioSpin, Billerica, MA, USA) L-band EPR imager. Main magnet (i) and magnetic field gradient assembly (ii).

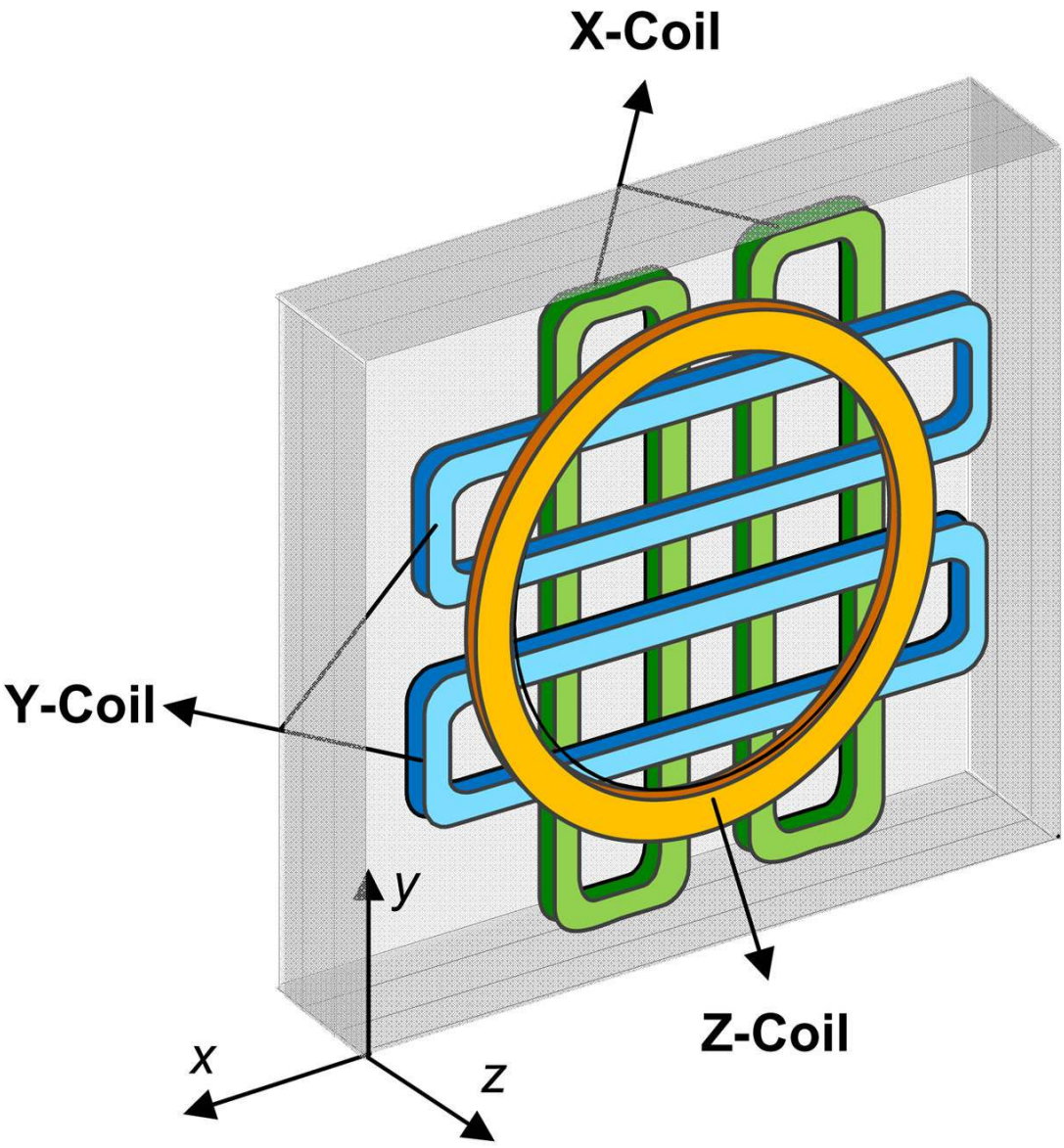

Figure 6.
Gradient coil assembly. Left-side enclosure of a 3D gradient coil assembly is shown. The Z-gradient is generated using Maxwell coils, while X- and Y-gradients are generated using flat pair coils.

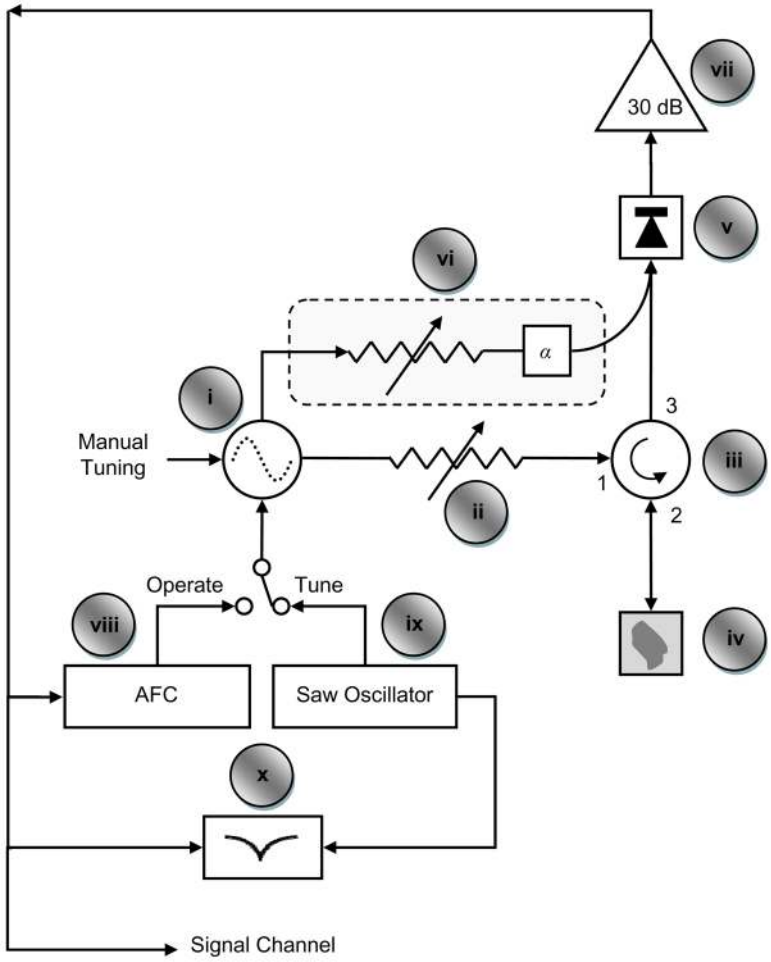

Figure 7.
Layout of a typical CW EPR bridge. Adapted with permission from Mr. Eric Kesselring.

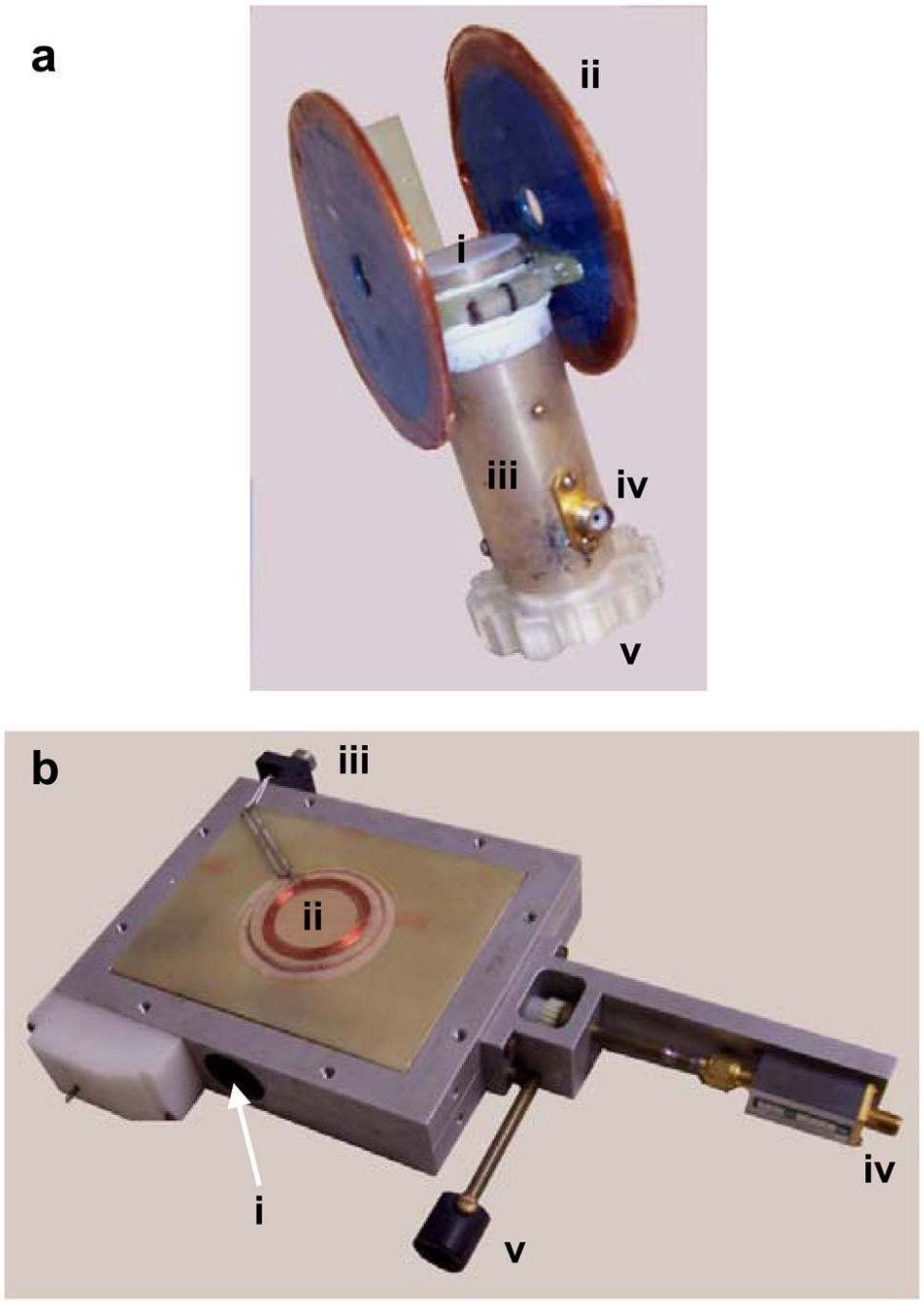

Figure 8.

Two frequently used resonator designs for EPR spectrometer. **a:** Surface bridged, loop-gap resonator (LGR). The LGR resonator structure is housed inside a metallic tubular shield. Legends: i, active surface area for sample; ii, filed modulation coils; iii, resonator shield; iv, RF input connector; v, coupling adjustment ring. The connector for field modulation coil is not visible from this view. The resonant frequency of this unloaded LGR was 1.25 GHz. **b:** Volume reentrant resonator (RER). The RER houses a cylindrical cavity of 24 mm diameter and 22 mm of effective length. Legends: i, sample cavity opening; ii, modulation coils; iii, connector of modulation coils; iv, RF input connector; v, coupling adjustment knob. The resonant frequency of this unloaded RER was 1.27 GHz

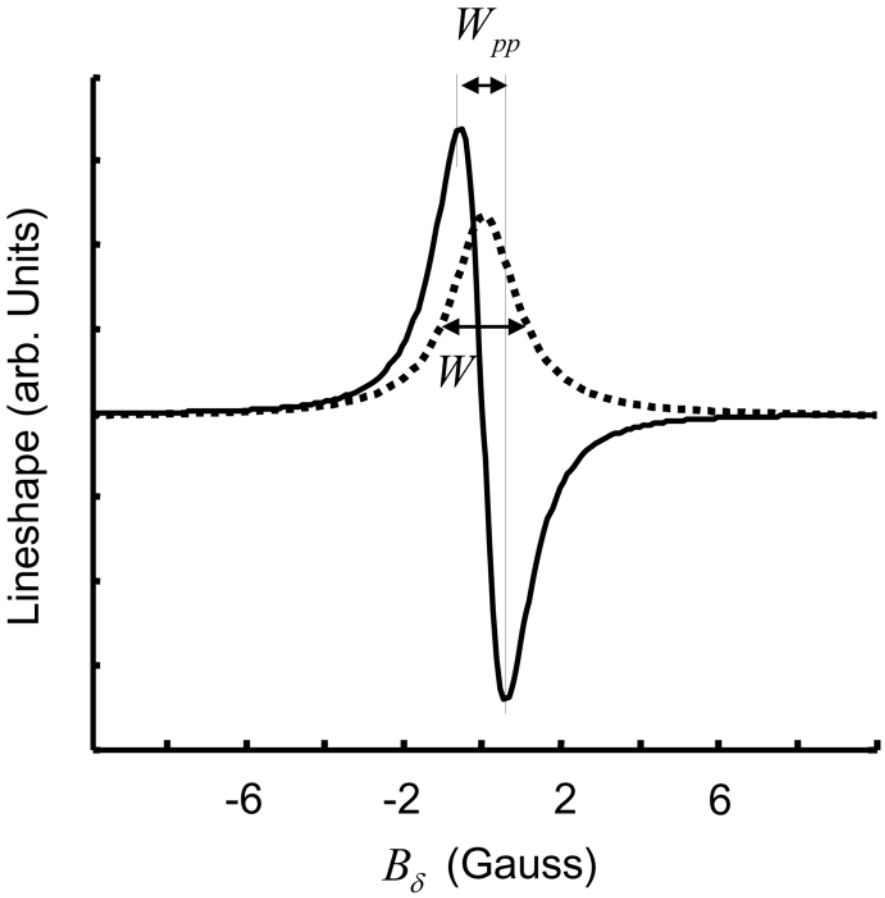

Figure 9.
Lorentzian lineshape (dotted line) with FWHM linewidth $W = 1$ G. First derivative Lorentzian lineshape (solid line) with peak-to-peak linewidth W_{pp} =0.58 G. For a Lorentzian lineshape, $W_{pp}=W/\sqrt{3}$.

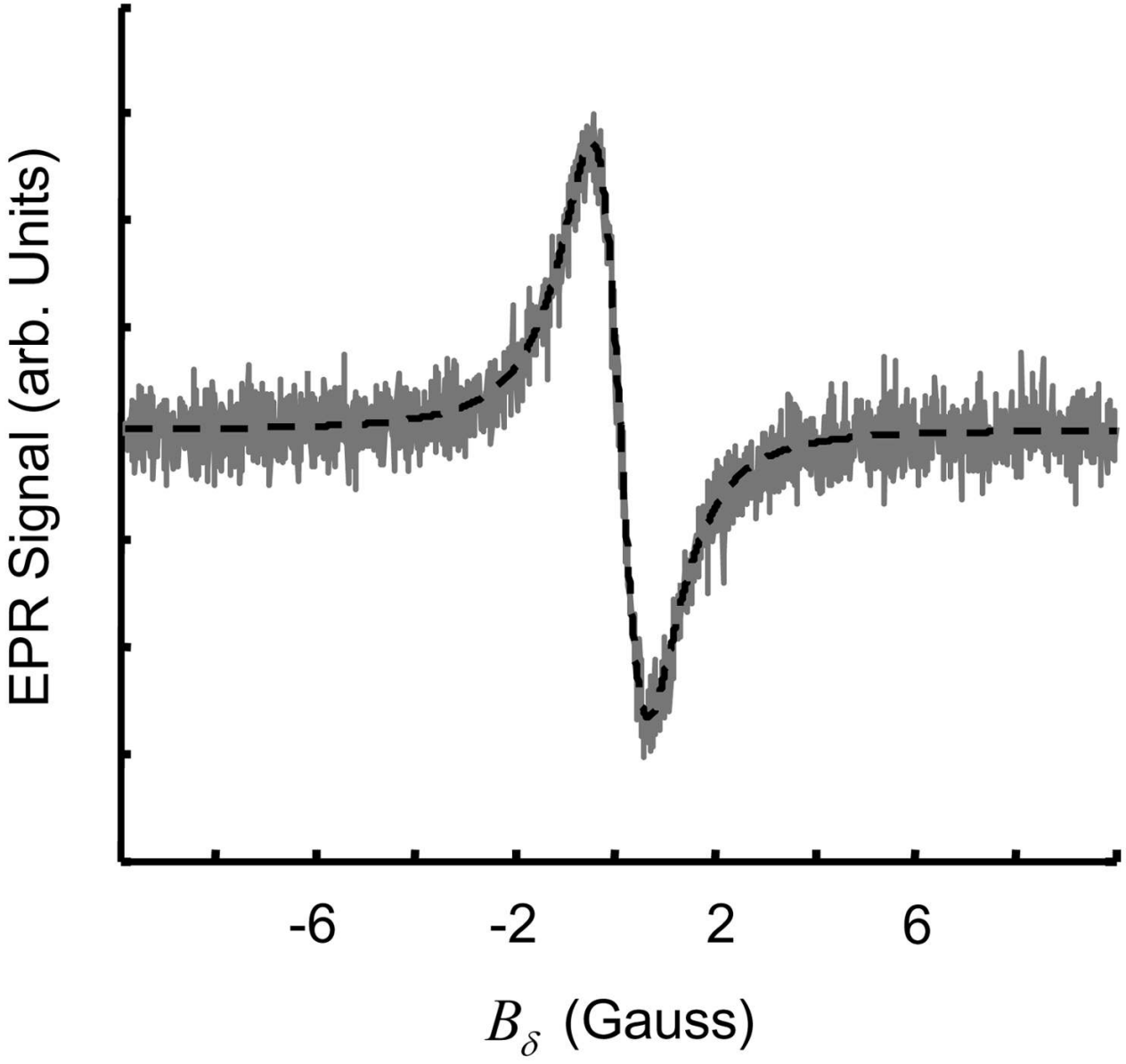

Figure 10.
Measured data (gray line) is generally noisy and curve fitting (dashed line) is applied to extract the linewidth information.

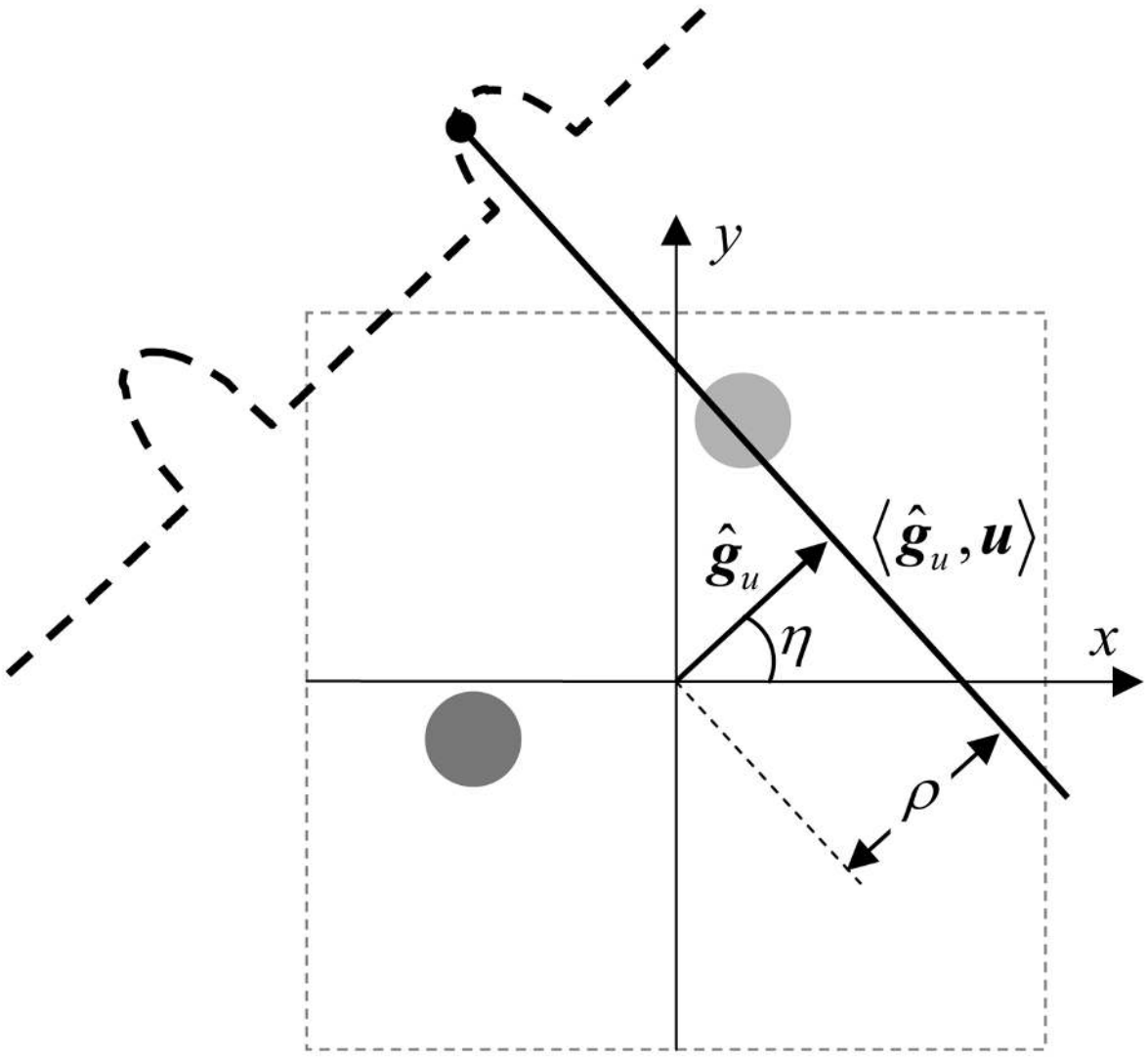

Figure 11.
Projection acquisition for a 2D spatial digital object. Angle η defines orientation of the applied gradient g_u, ρ defines the distance of resonant plane $\langle \hat{g}_u, u \rangle$ from the origin.

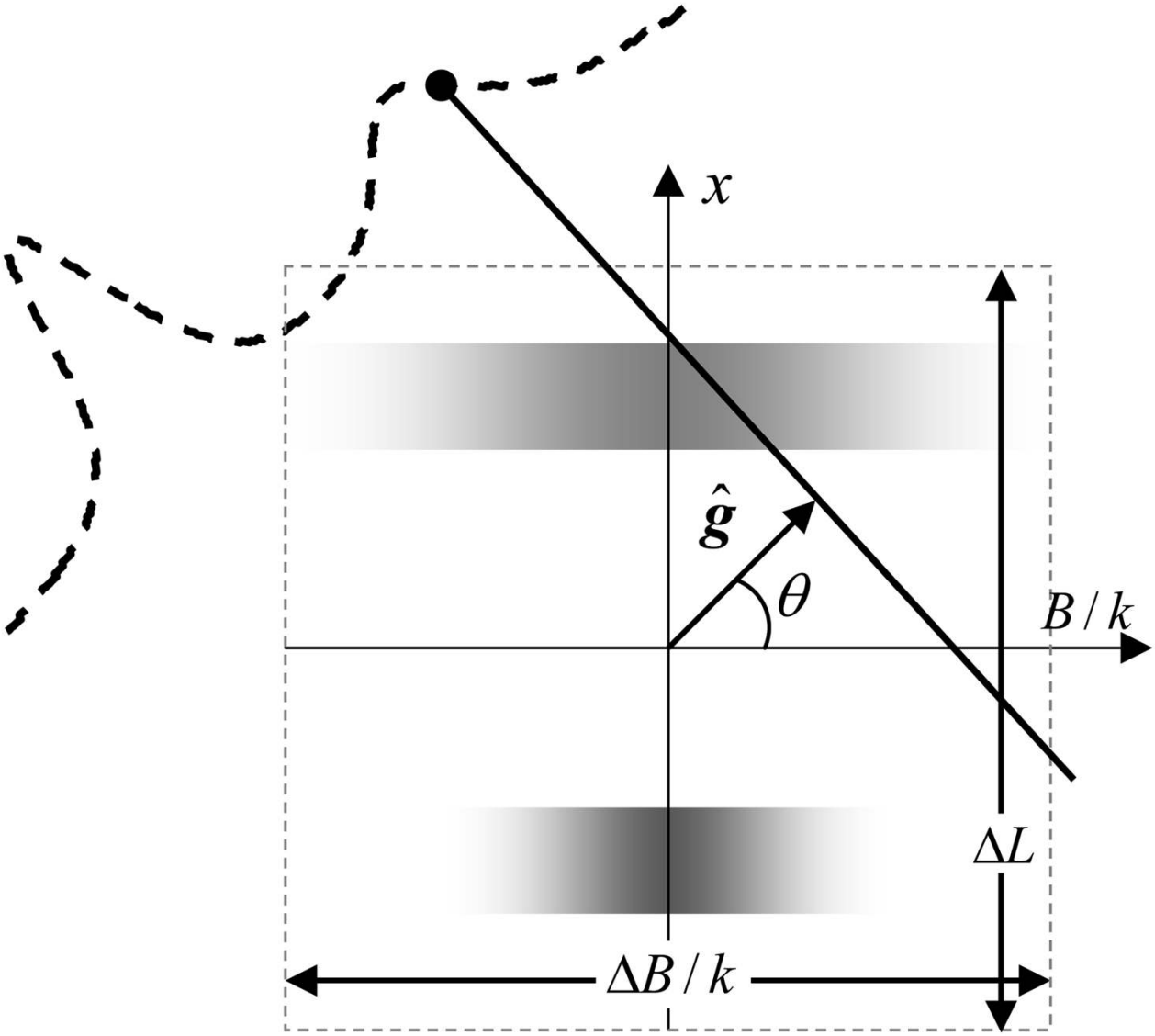

Figure 12.

Data collection for a 2D spectral-spatial digital object. The vertical-axis represents the spatial dimension while the horizontal-axis represents the spectral dimension. The figure shows two regions; the one on the top has a large linewidth while on the bottom exhibits a smaller linewidth. Here, $k = \Delta B/\Delta L$ and $\hat{\boldsymbol{g}} = (\hat{\boldsymbol{g}}_u \sin\theta, \cos\theta)$is a generalized gradient vector which incorporates gradient strength with gradient orientation.

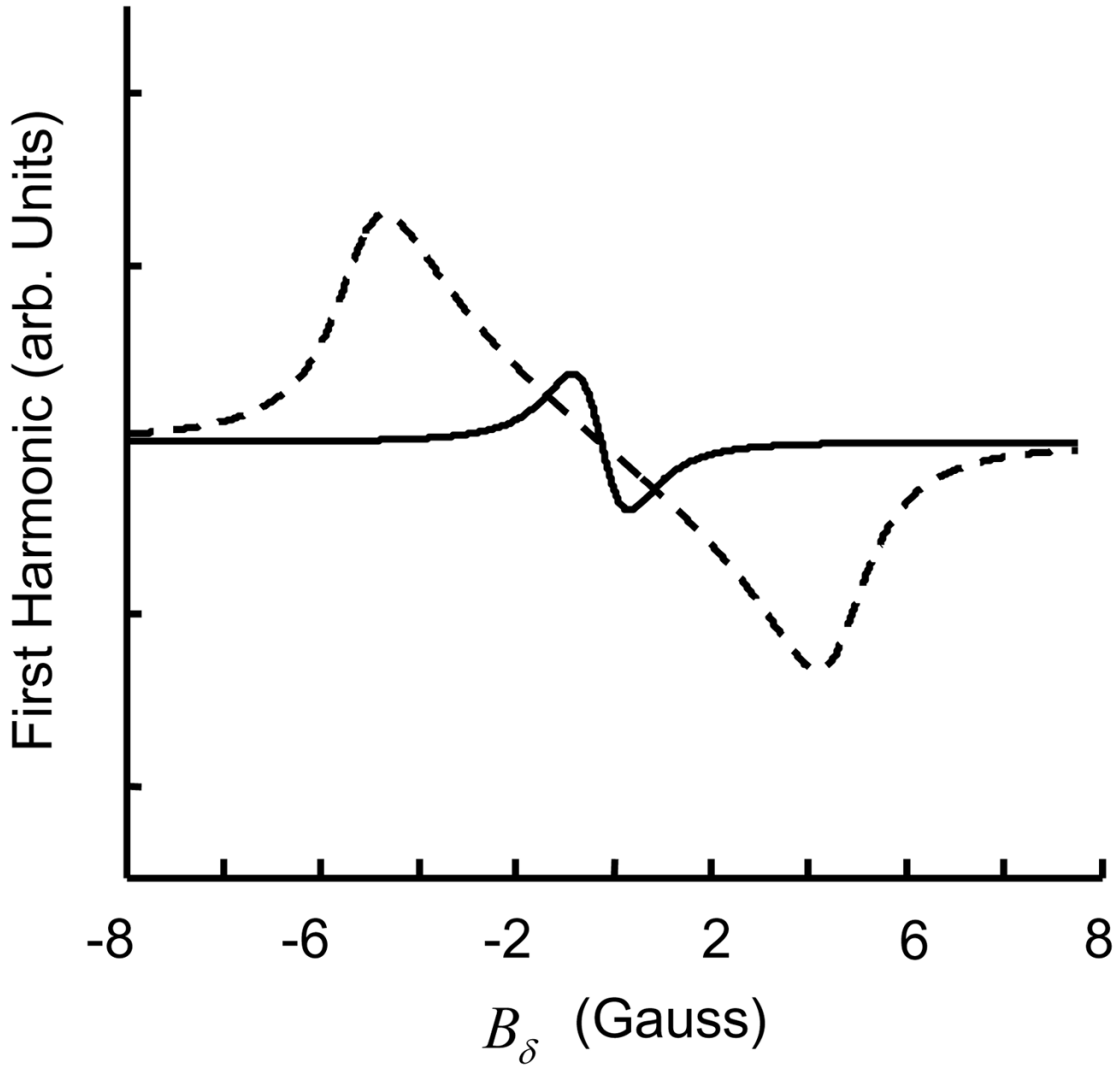

Figure 13.
Effect of modulation amplitude B_m on lineshape. The solid line represents lineshape for a modulation amplitude which is 10% of linewidth W, while the dashed line represents the lineshape for a modulation amplitude which is 250% of W.

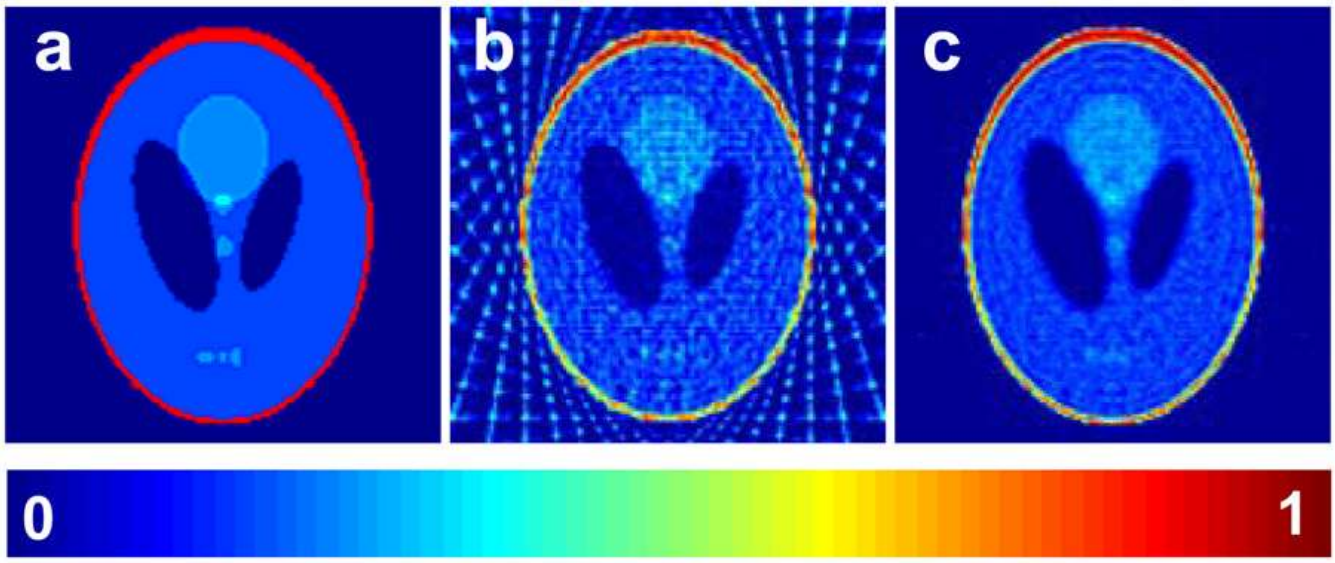

Figure 14.

Comparison of an iterative reconstruction method with the commonly used filtered backprojection method. **a:** A 128×128 2D digital Shepp-Logan phantom; **b:** Reconstruction from filtered backprojection using 20 noiseless projections, after the reconstruction all pixels with negatives values were set to zero; **c:** Reconstruction based on algebraic reconstruction technique (ART) with nonnegativity constraint using 20 noiseless projections.

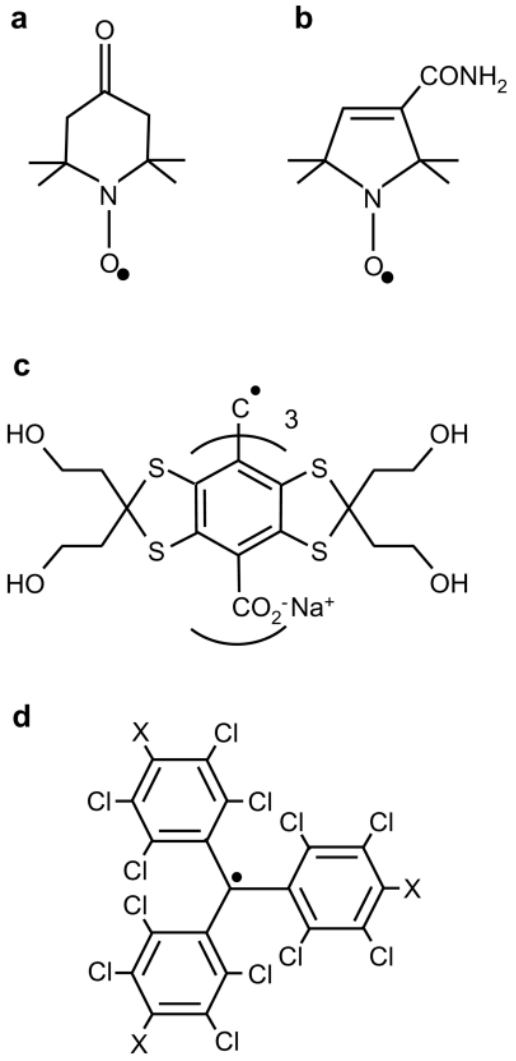

Figure 15.

Chemical structure of soluble spin probes commonly used for EPR oximetry. **a**: Tempone (1-oxyl-2,2,6,6-tetramethyl-4-piperidione); **b**: CTPO (2,2,5,5-tetramethyl-3-pyrroline-1-oxyl-2-carboxamide); **c**: TAM (triarylmethyl) OX063; **d**: PTM (perchlorotriphenylmethyl) for X=Cl, PTM-TE for X= COOR, and PTM-TC for X=COOH;

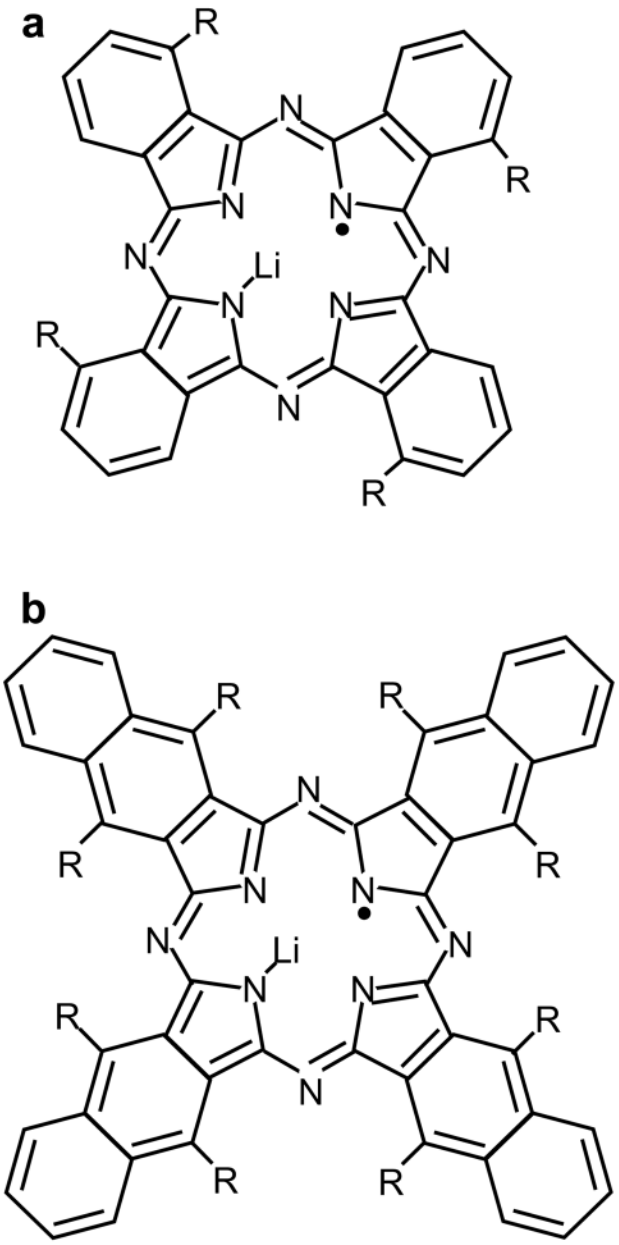

Figure 16.
Chemical structure of particulate spin probes commonly used for EPR oximetry. **a**: LiPC for R=H and LiPc-α-OPh for R=phenoxy; **b**: LiNc for R=H and LiNc-BuO for R=$O(CH_2)_3CH_3$

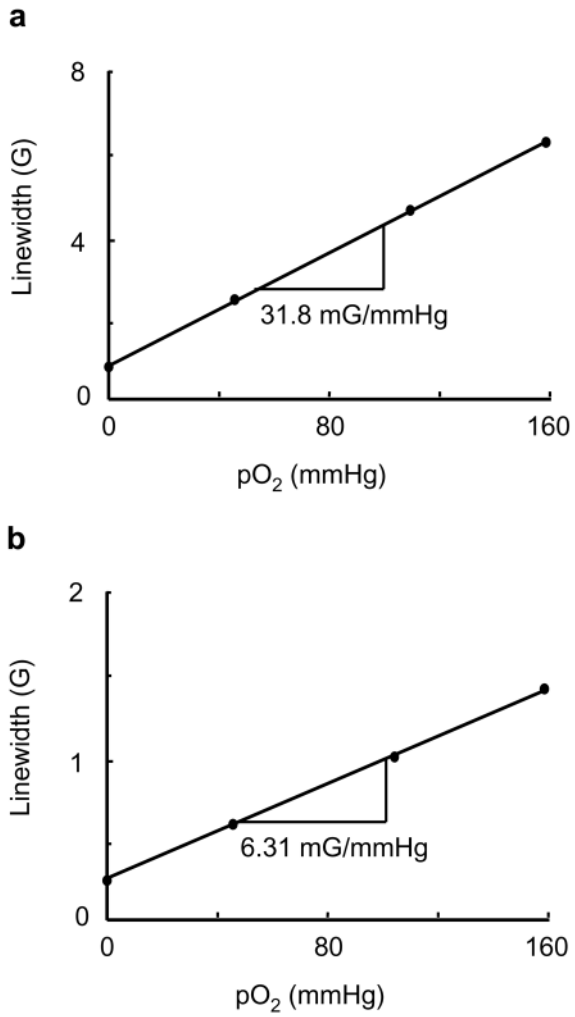

Figure 17.

Effect of molecular oxygen on the EPR linewidth of LiNc (a) and LiNc-BuO (b) crystals. A linear variation of linewidth with the pO_2 is observed for both the probes. For LiNc: anoxic linewith, 0.90 G; oxygen sensitivity, 31.8 mG/mmHg. For LiNc-BuO: anoxic linewidth=0.41 G; oxygen sensitivity=6.31 mG/mmHg. Measurements were conducted at L-band CW EPR spectrometer. The instrumental settings were: microwave power, 2 mW; modulation amplitude, 200 mG; modulation frequency, 100 kHz; receiver time constant, 10 ms; acquisition time, 10 s (single scan);

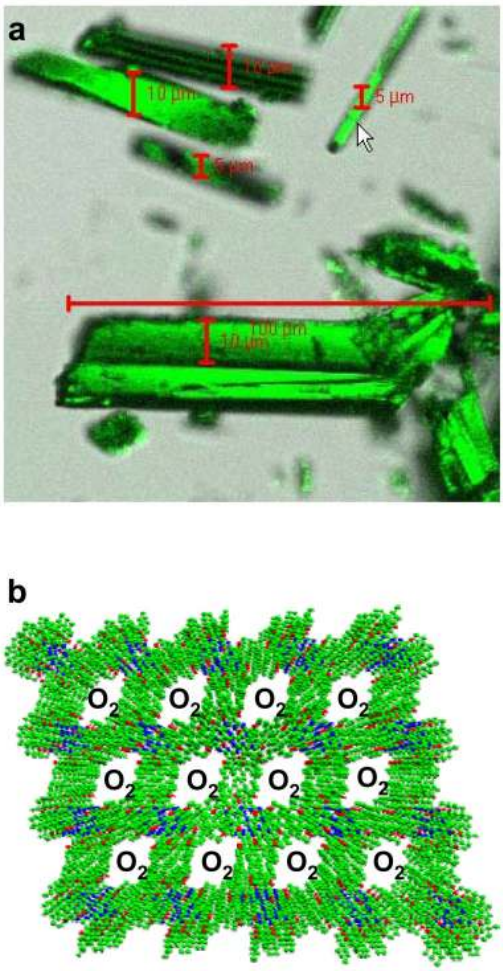

Figure 18.

LiNc-BuO in crystalline form. **a**: Photograph of needle-shaped LiNc-BuO microcrystals; **b**: Stacking of LiNc-BuO molecules in a crystal. The EPR line-broadening occurs due to the diffusion of O_2 into the microchannels and subsequent spin-spin interaction through the Heisenberg exchange mechanism. Image **b** is reprinted with permission from ref [191]. Copyright 2006 The Royal Society of Chemistry. **DOI:** 10.1039/b517976a.

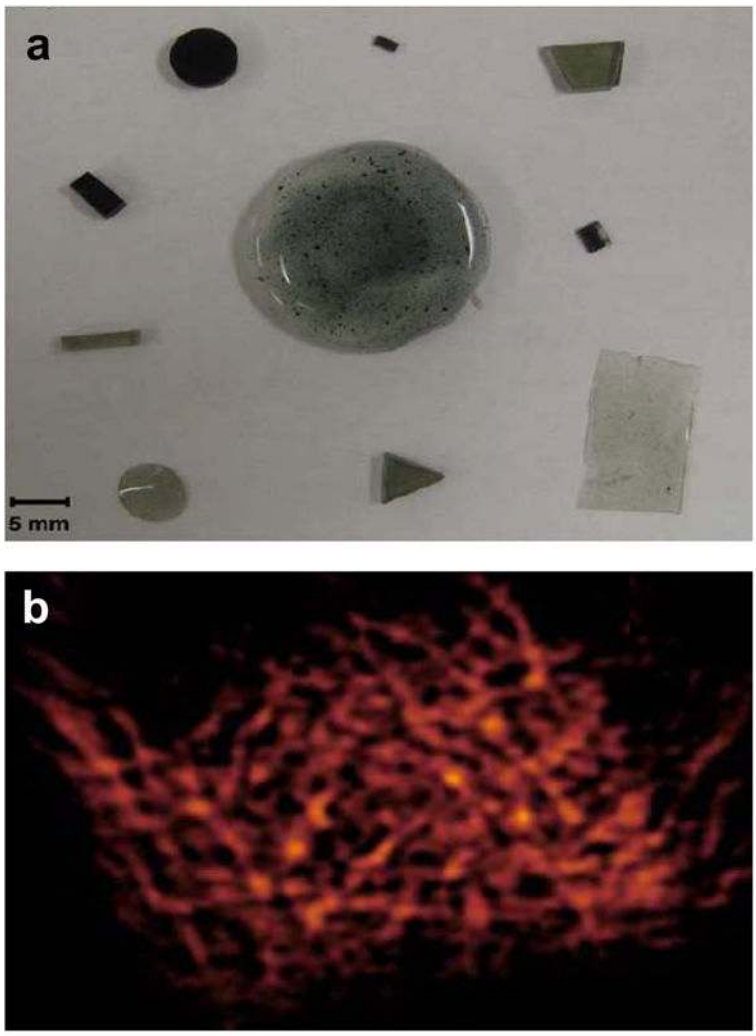

Figure 19.
Chips fabricated by the encapsulation of LiNc-BuO particulates in PDMS. **a**: Pieces of polymerized LiNc-BuO with varying sizes, shapes and ratios of particulate to polymer. Dark shade indicates higher concentration of LiNc-BuO crystals. **b**: X-band EPR images of polymerized LiNc-BuO chip to evaluate spin distribution. Samples were imaged under anoxic conditions, in a sealed tube. Reprinted with permission from ref [196]. Copyright 2009 Springer.

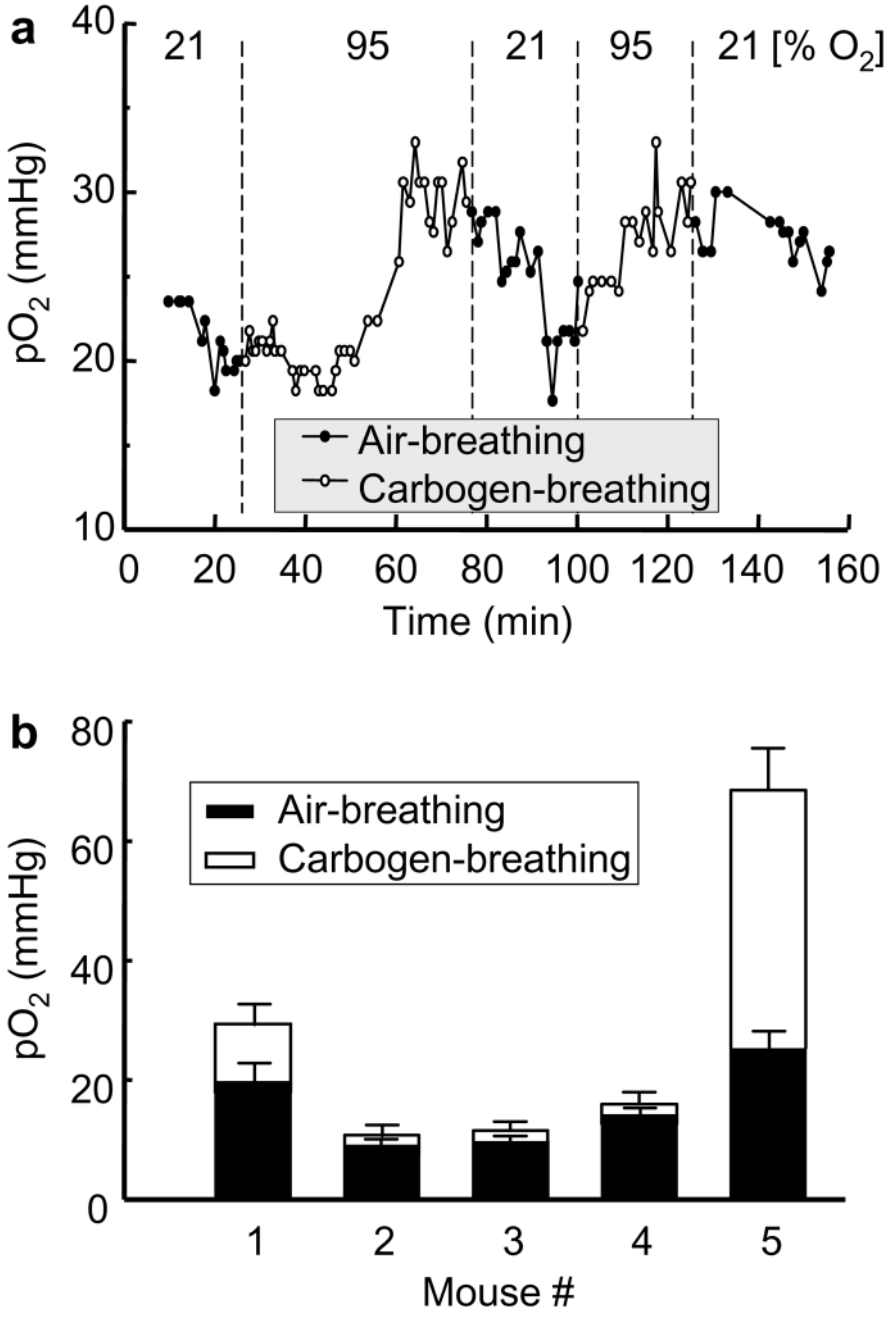

Figure 20.

Effect of FiO_2 (fraction of inspired oxygen) on the tumor pO_2. Twenty μL of PTM-TE (12 mM in HFB) was injected directly into RIF-1 tumor grown in the hind leg of a C3H mouse. **a:** Change in pO_2 in the tumor of a single animal while the FiO_2 was successively switched between 21% and 95% (carbogen gas), as indicated. **b:** The pO_2 values obtained before (FiO_2 = 21%) and 20 min after changing the FiO_2 to 95% in 5 different animals. Reprinted with permission from ref [180]. Copyright 2007 Elsevier.

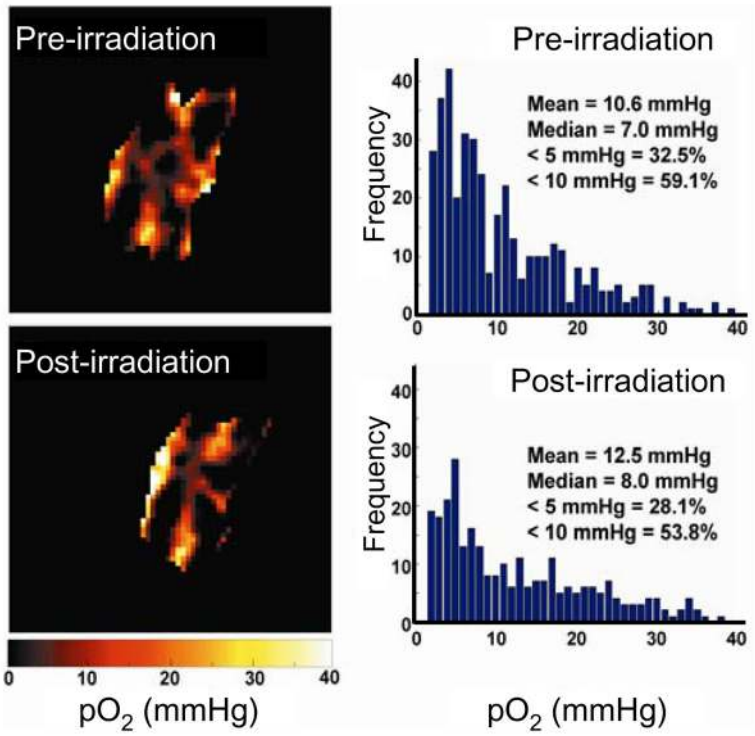

Figure 21.

In vivo mapping of tumor pO_2 during growth and after treatment with X-ray irradiation. Change and redistribution of tumor pO_2 are shown for a small (volume 113 mm^3) RIF-1 tumor before (pre-) and 1 h after (post-) X-ray irradiation. The tumor was implanted with RIF-1 cells internalized with nanoparticulates of LiNc-BuO. A dose of 30 Gy was delivered with 6-MeV electrons at a dose rate of 3 Gy/min. Redistribution is seen with a modest increase in the pO_2. Reprinted with permission from ref [213]. Copyright 2007 John Wiley and Sons.

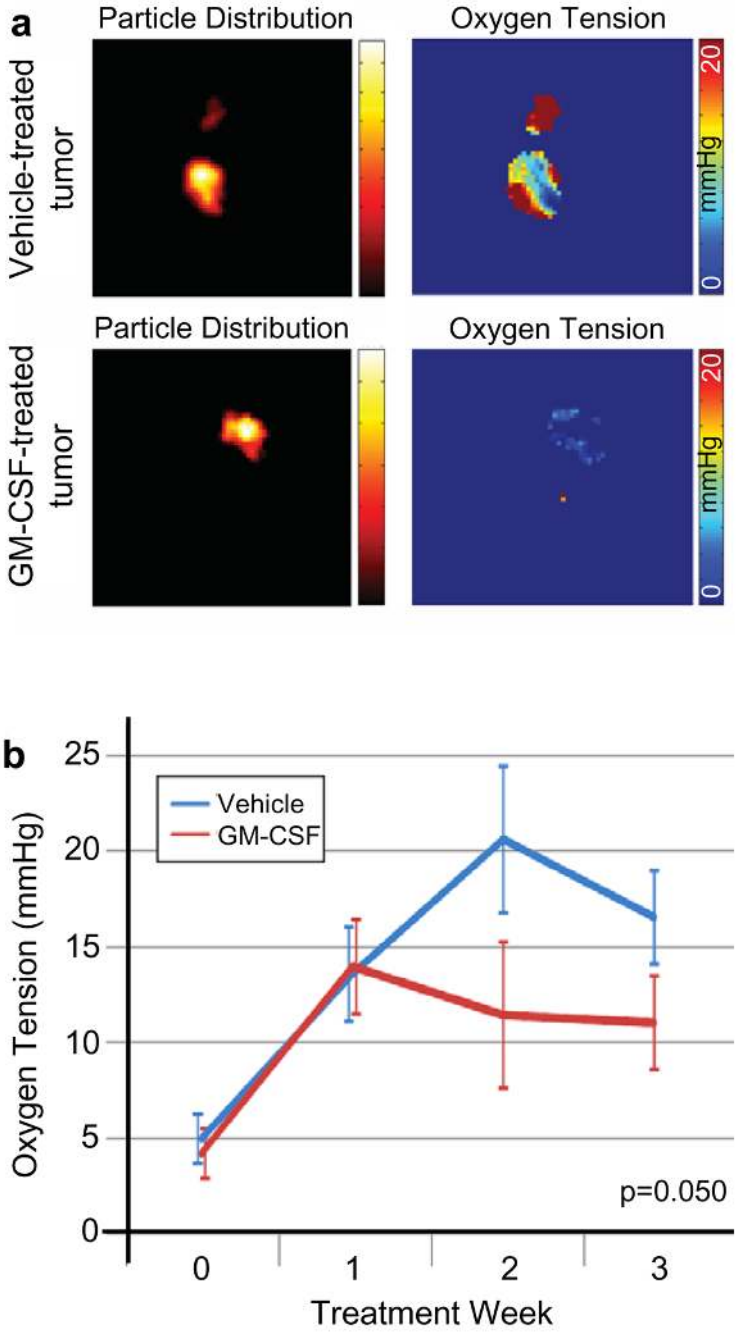

Figure 22.

Intratumor GM-CSF treatment reduces oxygen levels within mammary tumors *in vivo*. **a**: Representative EPR images showing probe distribution (left) and oxygen in the tumor (right); **b**: Trends in tumor oxygen levels over time (±SEM, N=5). Reprinted with permission from ref [215]. Copyright 2009 American Association of Cancer Research.

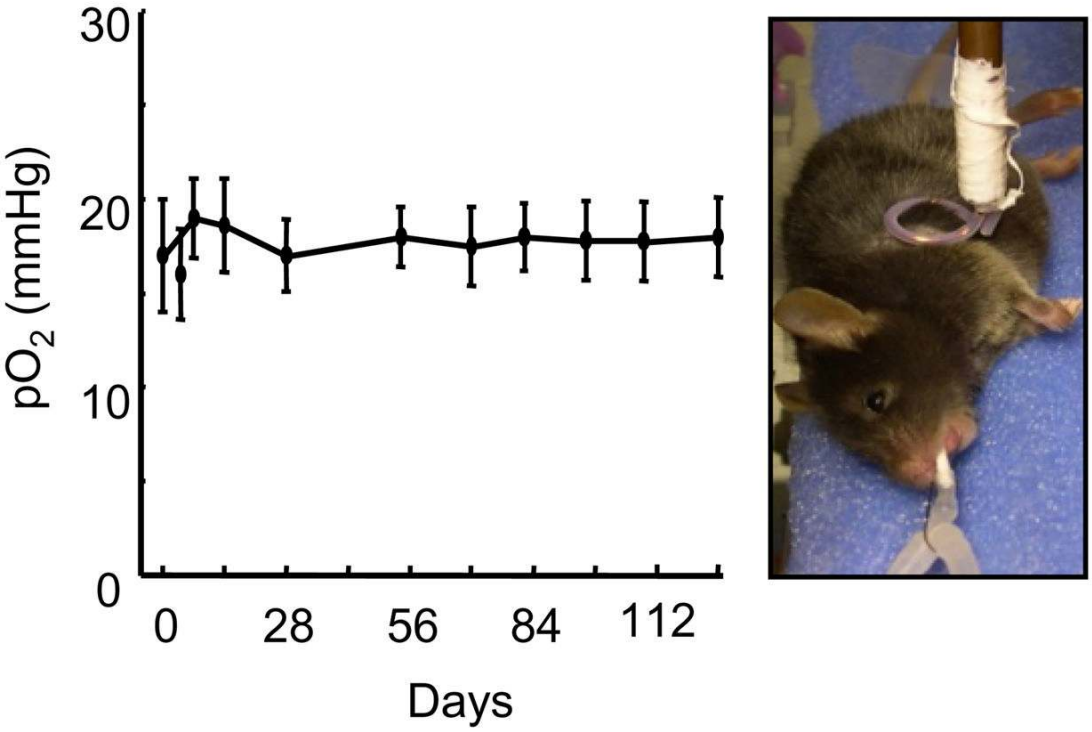

Figure 23.

Long-term monitoring of *in situ* pO_2 at the site of transplanted skeletal myoblasts (SM) in infarcted mouse hearts. Myocardial tissue pO_2 from mice (N=5) implanted with LiNc-BuO in the mid-ventricular region without left anterior descending coronary artery ligation. Data show the feasibility of pO_2 measurements for more than 3 months after implantation. Reprinted with permission from ref [226]. Copyright 2008 Springer.

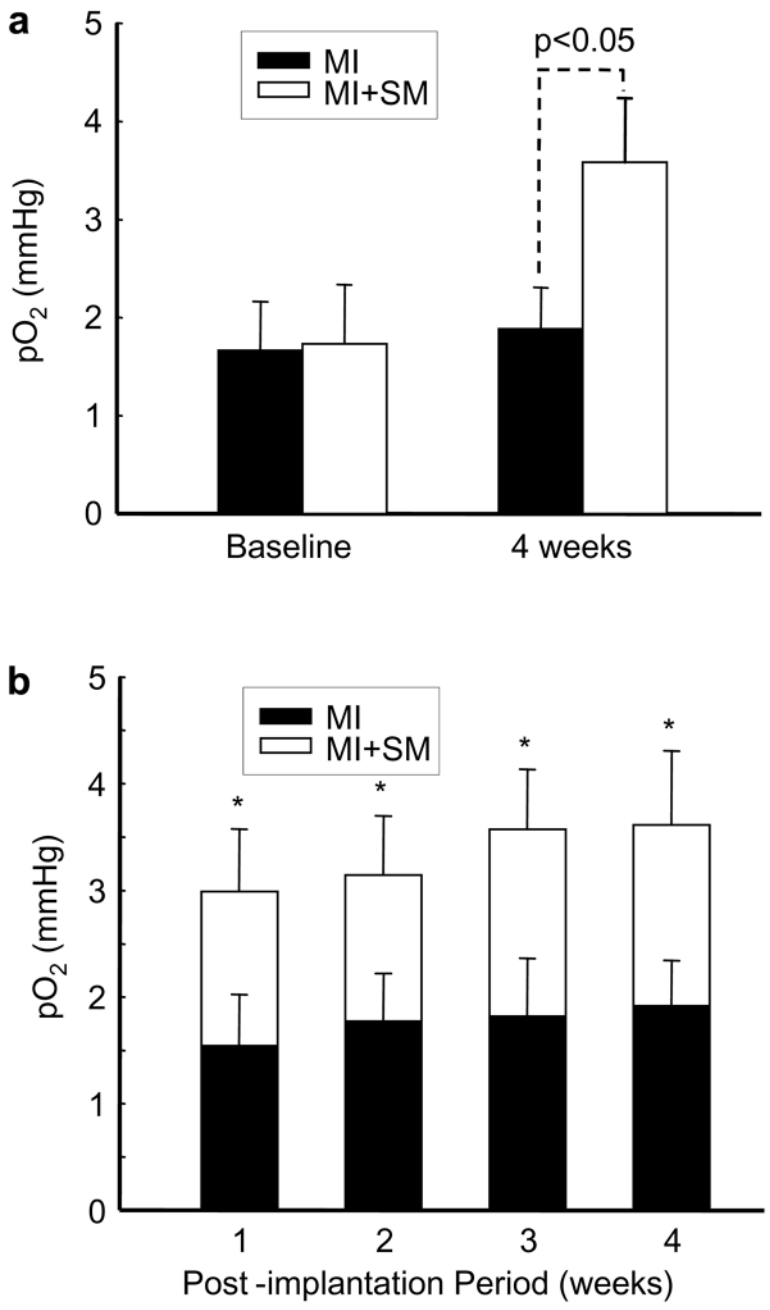

Figure 24.

Myocardial pO_2 in the infarcted heart at site of cell transplantation. Myocardial pO_2 values were measured repeatedly for 4 weeks using *in vivo* EPR oximetry in mice hearts transplanted with LiNc-BuO-labeled skeletal myoblasts (SM) cells. **a:** Tissue pO_2 at 4 weeks after treatment with SM cells (MI+SM) was significantly higher as compared to untreated (MI) hearts. **b**: The time-course values of myocardial pO_2 measured from infarcted hearts (MI), and infarcted hearts treated with SM cells (MI+SM) are shown. Values are expressed as mean±SD (n=7 per group). *p<0.05 vs MI group. Reprinted with permission from ref [227]. Copyright 2007 American Physiological Society.

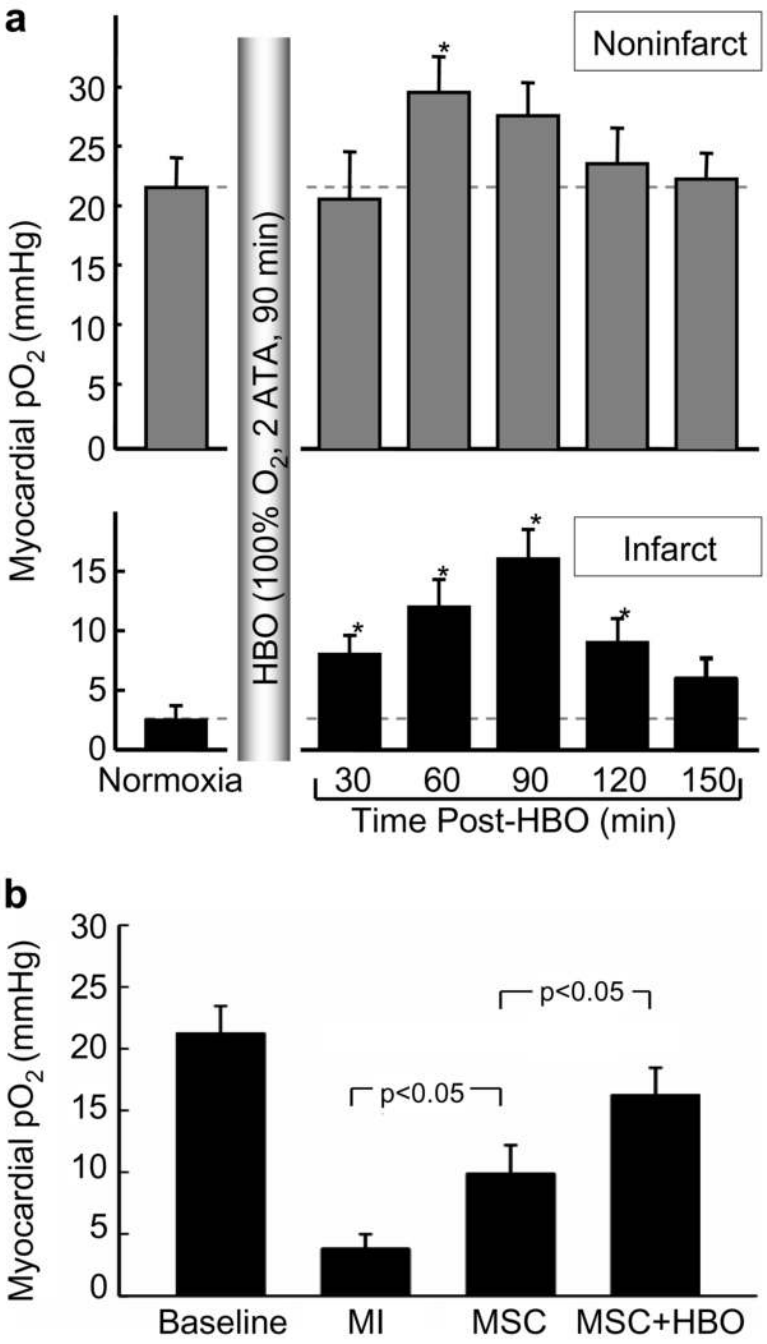

Figure 25.

Hyperbaric oxygenation and myocardial pO_2, *in vivo*. **a**: Myocardial pO_2 in (noninfarcted and infarct) rat hearts measured before (normoxia) and after HBO. Data represent mean±SD obtained from 4 rats. The results show an increase in oxygenation levels reaching significance at 60 min followed by returning to baseline in about 2.5 hours in the noninfarcted hearts. In the infarcted hearts the oxygenation levels are significantly higher up to 2 hours post-treatment. It is interesting to note that a 5.8-fold increase in oxygenation is achieved in the infarct hearts after 90 min of HBO. **b**: Myocardial pO_2 in rat hearts transplanted with stem cells at 2 weeks. The results (mean±SD; N=4 rats) show an increase in myocardial oxygenation in hearts treated

with MSC and further enhancement in pO_2 was observed in hearts treated with HBO. Reprinted with permission from ref [229]. Copyright 2009 Elsevier.

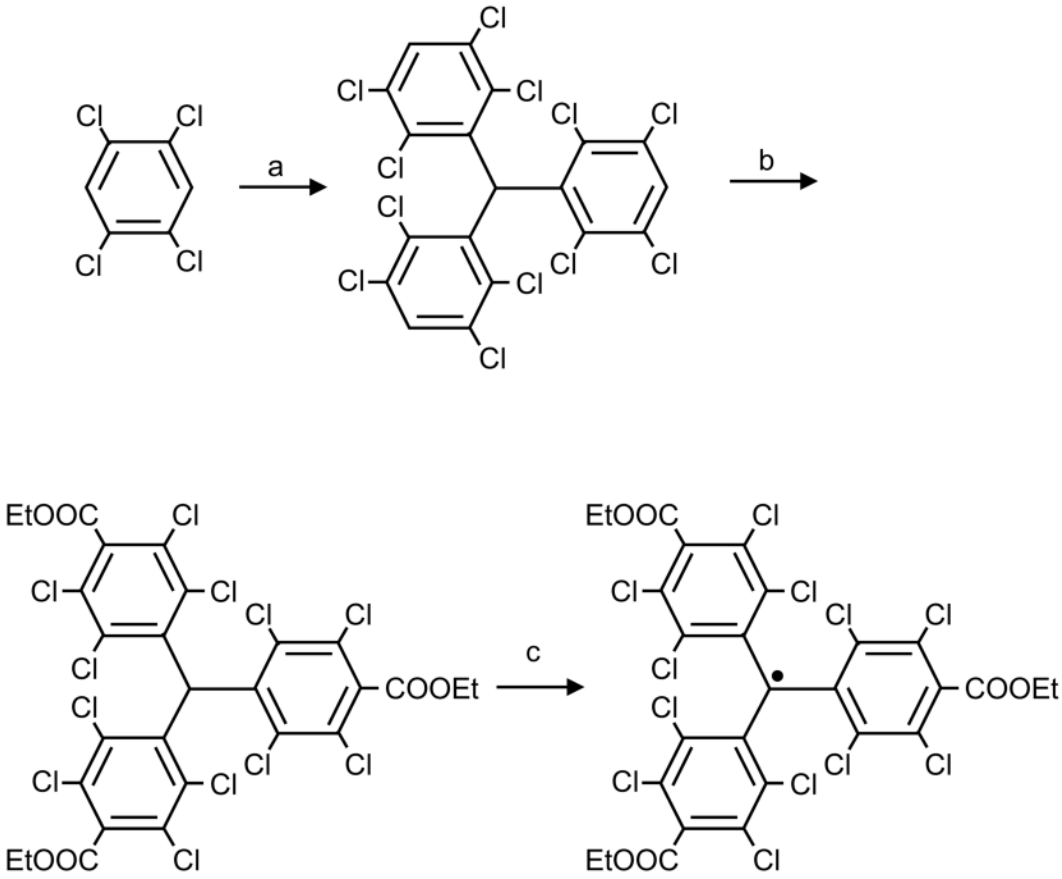

Scheme 1.

Synthesis of PTM-TE radical. Reagents and conditions: (a) $CHCl_3$, $AlCl_3$; (b) *n*-BuLi, TMEDA, ethyl chloroformate, 77%; (c) (1) NaOH, DMSO/Et_2O, (2) I_2, Et_2O, 93%.

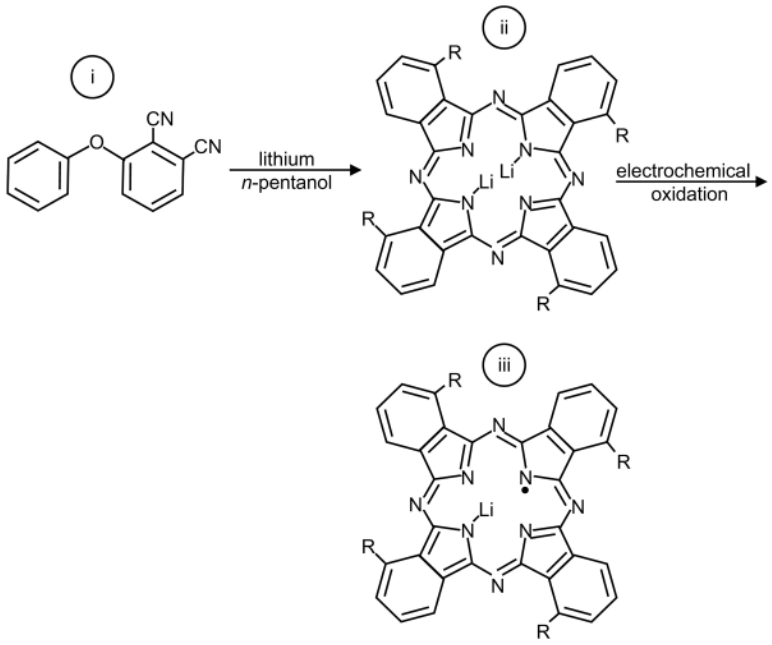

Scheme 2.

LiPc-α-OPh was synthesized by cyclotetramerization of 3-phenoxyphthalonitrile (i) in the presence of lithium pentoxide to obtain Li_2Pc-α-OPh (ii) followed by electrochemical oxidation to form microcrystals of LiPc-α-OPh (iii).

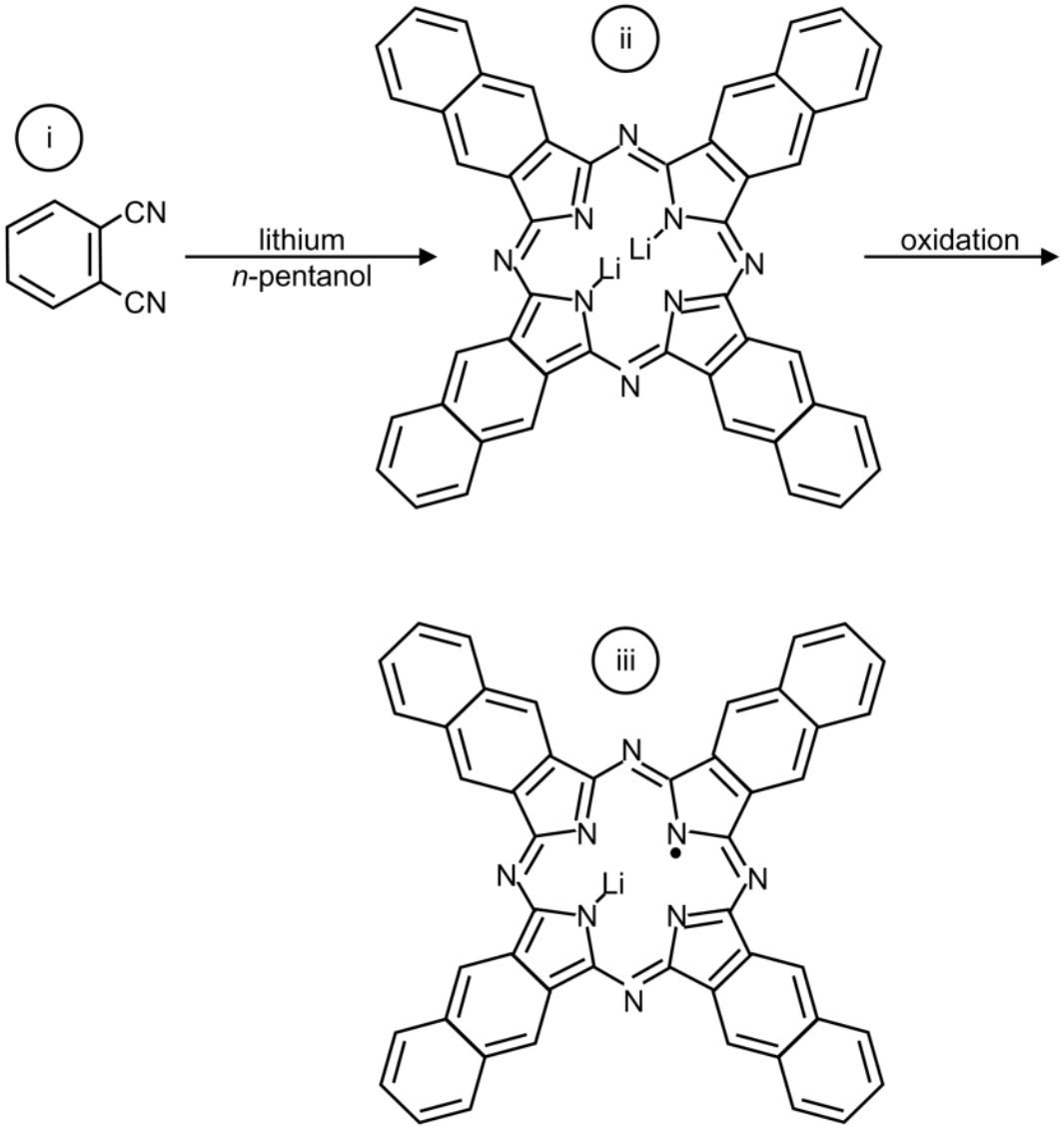

Scheme 3.

LiNc was synthesized by cyclotetramerization of 2,3-dicyano naphthalene (i), in the presence of lithium/pentanol to give Li_2Nc (ii), followed by oxidation to form microcrystals of LiNc (iii).

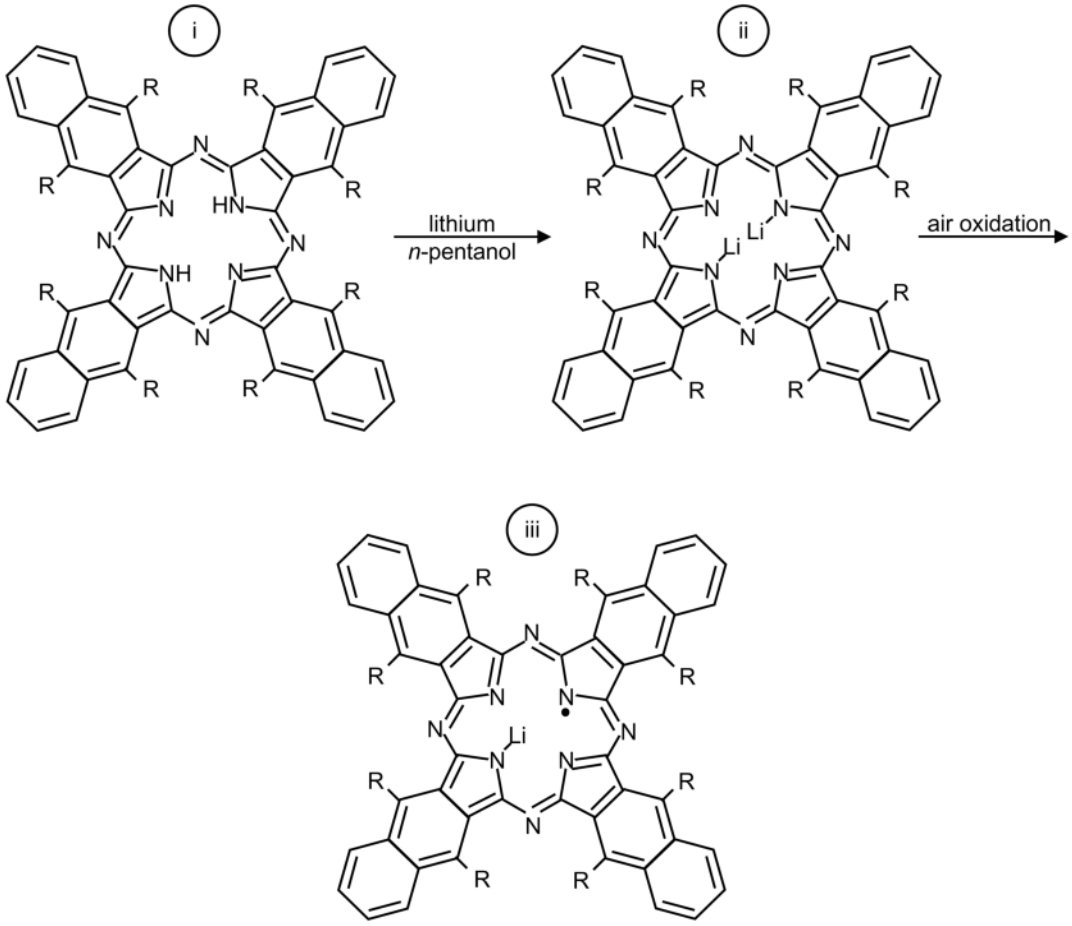

Scheme 4.

LiNc-BuO was synthesized from lithium metal and octa-*n*-butoxy-substituted naphthalocyanine (Nc-BuO) (i) in *n*-pentanol. Nc-BuO macrocyclic ligand reacted with lithium pentoxide (lithium metal in pentanol) to give dilithium octa-*n*-butoxy-naphthalocyanine (Li_2Nc-BuO) (ii), followed by oxidation to give LiNc-BuO radical (iii) which formed as needle-shaped dark-green microcrystals.

Table 1

Anoxic linewidth and oxygen sensitivity values for some commonly used EPR oximetry spin probes. Values for LiPc from Liu *et al.*[156] and Ilangovan *et al.*[157]; values for LiPc-α-OPh from Pandian *et al.*[158]; values for LiNc from Manivannan *et al.*[159]; values for LiNc-BuO from Pandian *et al.*[160]; values for Fusinite from Vahidi *et al.*[161] and Smirnova *et al.*[162]; values for Gloxy from James *et al.*[163]; values for India Ink from Goda *et al.*[164]; values for Tempone from Shen *et al.*[165]; values for TAM from Dhimitruka *et al.*[166].

Spin Probe	Spin Density (spins/g) $\times 10^{19}$	Anoxic Peak-to-Peak Linewidth (mG)	Oxygen Sensitivity (mG/mm Hg)
LiPc	10	10–14	6.1–9.5
LiPc-α-OPh	--	530	13.7
LiNc	68	510	30
LiNc-BuO	72	210	8.5
Fusinite	1–2	800	25
Gloxy	4.6	550	27
India Ink	2.5	650	420
Tempone	--	330	0.64
TAM	--	90	0.84